Advances in OTFS Waveform for Integrated Sensing and Communications

Correas Serrano, A.

DOI
10.4233/uuid:97bdc0b8-af5b-42ff-8513-c2520f12b098

Publication date
2025

Document Version
Final published version

Citation (APA)
Correas Serrano, A. (2025). *Advances in OTFS Waveform for Integrated Sensing and Communications*. [Dissertation (TU Delft), Delft University of Technology]. https://doi.org/10.4233/uuid:97bdc0b8-af5b-42ff-8513-c2520f12b098

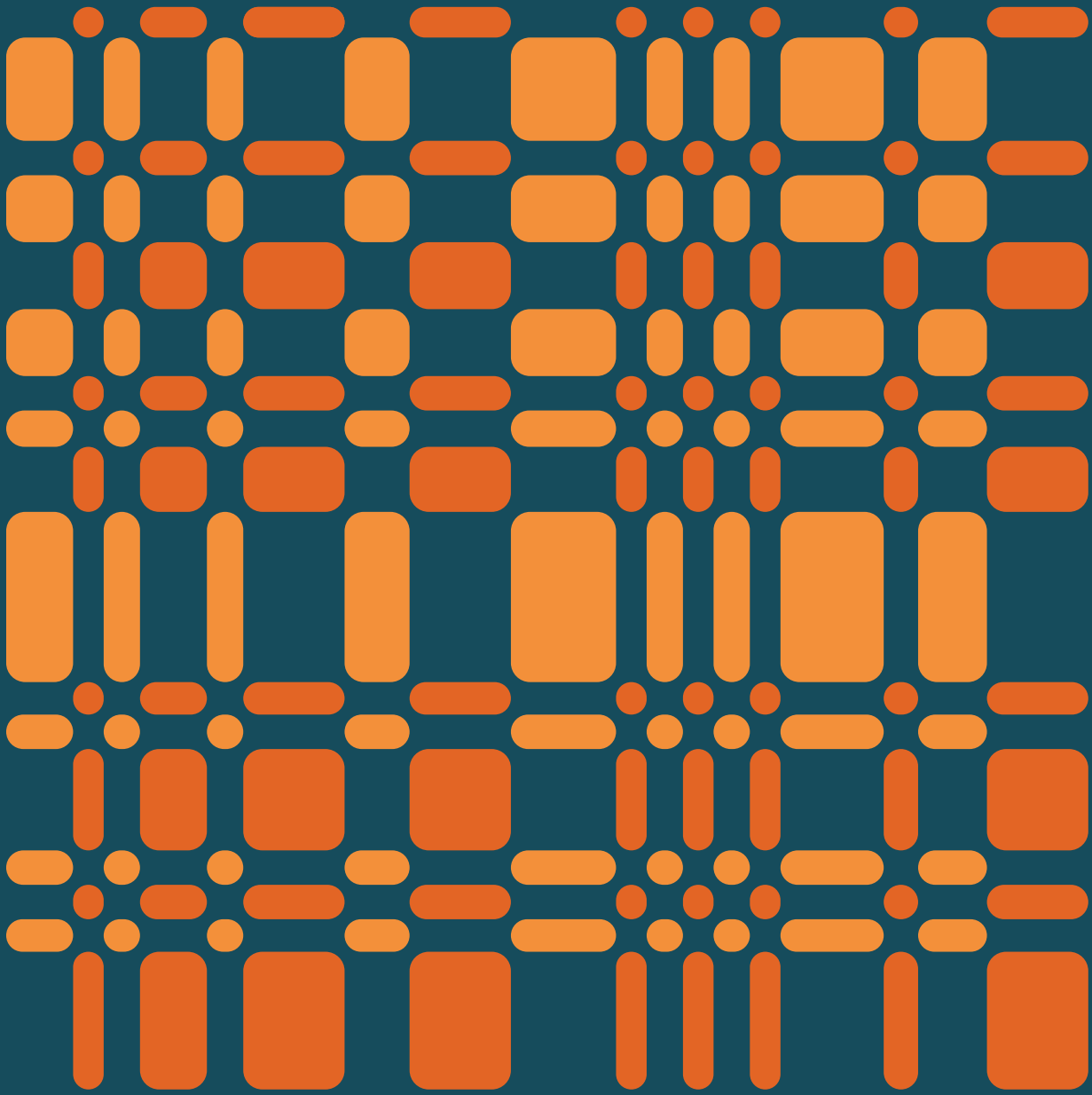

Advances in OTFS Waveform for Integrated Sensing and Communications

Aitor Correas Serrano

Advances in OTFS Waveform for Integrated Sensing and Communications

Advances in OTFS Waveform for Integrated Sensing and Communications

Dissertation

for the purpose of obtaining the degree of doctor
at Delft University of Technology
by the authority of the Rector Magnificus, prof. dr. ir. T.H.J.J. van der Hagen,
chair of the Board for Doctorates
to be defended publicly on
Monday 3 November 2025 at 17:30

by

Aitor Correas Serrano

Master of Science in Telecommunication Engineering,
Technical University of Cartagena, Spain
born in Tarragona, Spain

This dissertation has been approved by the promotors.

Composition of the doctoral committee:

Rector Magnificus	chairperson
Prof. dr. A. Yarovoy	Delft University of Technology, *promotor*
Dr. N. Petrov	Delft University of Technology, *copromotor*
Independent members:	
Prof. dr. ir . L.C.N. de Vreede	Delft University of Technology
Prof. dr. ir. G.J.T. Leus	Delft University of Technology
Prof. dr. ir. P.G.M. Baltus	Eindhoven University of Technology
Dr. M. Bauduin	Interuniversity Microelectronics Centre, Belgium
Dr. M. Spirito	Delft University of Technology, *reserve member*
Dr. rer. nat. M.A. Gonzalez Huici	Fraunhofer FHR, Germany, *non-independent member*

The work described in this thesis was financially supported by the Fraunhofer Institute for High-frequency Physics and Radar (FHR).

Keywords: MIMO Radar, Integrated Sensing and Communications, Multicarrier Waveforms, Orthogonal Time Frequency Space.

Printed by: Proefschiftspecialist, 1506RZ Zaandam, The Netherlands.

Front & Back: Concept by A. Correas Serrano, design by C. Piancatelli Ruiz.

ISBN number

An electronic copy of this dissertation is available at
`https://repository.tudelft.nl/`.

Author e-mail: aitorcorreas@gmail.com

To the family that I was given and the family I found along the way. To everyone I have shared this journey with. I love you all.

Aitor Correas Serrano

CONTENTS

SUMMARY

This dissertation pushes orthogonal time-frequency space (OTFS) from a communications-centric innovation to a radar-ready waveform family suitable for future 6G integrated sensing and communications (ISAC). It is driven by the need to retain OTFS's Doppler resilience while overcoming three main drawbacks: a lack of a fair comparison study with orthogonal frequency-division multiplexing (OFDM) for radar tasks, (ii) its rigid, fully populated time-frequency (TF) structure that hinders multiple-access flexibility, and (iii) its high peak-to-average-power ratio (PAPR), which obstructs high-power operation, crucial for many sensing applications.

The dissertation begins by giving a layman's introduction to the problem of joint sensing and communication that is abstracted from the specific wireless electromagnetic applications that we study within the rest of the dissertation. We use this chapter to motivate our research, from the relevance of ISAC to the specific approach of choosing a pre-existing promising communication waveform and adapting it to perform radar tasks. This chapter also identifies the key knowledge gaps and research questions to be tackled within this dissertation. With this as background, Chapter 2 lays the theoretical bedrock. It introduces multicarrier waveforms and some key radar concepts, showcasing the similarities and differences between OTFS and OFDM. It also establishes a consistent notation that will be used in the rest of the dissertation.

Chapter 3 answers the first question by developing a family of monostatic radar receivers for OTFS and OFDM whose assumptions about intercarrier and inter-symbol interference are rigorously aligned. The study goes beyond the general impression that OTFS possesses innate Doppler immunity: once both waveforms are processed with an identical joint delay Doppler estimator, their range-Doppler performance converges. The perceived OTFS advantage is thus traced to receiver structure rather than fundamental waveform physics, re-focusing research attention on algorithm design.

Chapter 4 introduces non-uniform OTFS (NU-OTFS), a novel waveform that can be understood as a generalisation of OTFS that maps delay Doppler symbols onto quasi-arbitrary TF patterns via a non-uniform inverse symplectic finite Fourier transform. This flexibility enhances the multiple-access capabilities of OTFS for multiple input multiple output (MIMO) radar and multi-user (MU) communications. Realistic high-mobility communication simulations and the first over-the-air OTFS radar measurements confirm that NU-OTFS preserves the baseline bit-error-rate (BER) and sensing accuracy while allowing non-overlapping resource allocation and increased unambiguous radar parameter estimation.

Chapters 5 and 6 deepen the NU-OTFS investigation. Chapter 5 proposes a low-rank optimisation framework that leverages the joint ambiguity function to design NU-OTFS TF patterns with minimal sidelobes, exploring the scalability of NU-OTFS to multi-user and massive MIMO configurations in the presence of interference. Chapter 6 delivers the

first simultaneous MIMO NU-OTFS radar experiment in the literature by using a polarimetric radar. These experiments demonstrate very low cross-transmitter interference and full signal separability in real hardware, thereby validating NU-OTFS for dense ISAC deployments with multiple communication users and radar transmitters.

In Chapter 7, we move on from NU-OTFS to tackle the PAPR barrier by proposing constant-modulus OTFS (CM-OTFS), the first constant-envelope sister-waveform of OTFS. By fusing complementary sequences with the Zak transform formulation of OTFS, CM-OTFS neutralises amplifier clipping, clearly outperforming distorted OTFS when it comes to dynamic range in the range–Doppler radar estimation, and performing similarly to pristine OTFS. Although CM-OTFS suffers from a data-rate reduction when compared to pristine OTFS, it also outperforms distorted OTFS in communication tasks when it comes to symbol recovery.

In sum, the dissertation delivers a coherent toolkit that (i) clarifies the true origin of OTFS sensing gains, (ii) provides the waveform with OFDM-like scheduling freedom via the novel and well-researched NU-OTFS, and (iii) offers an alternative to remove the PAPR bottleneck through CM-OTFS. Collectively, these contributions support OTFS in becoming a practically deployable candidate for next-generation ISAC networks that demand dense MIMO operation, fragmented spectral access, and high-power front-ends.

SAMENVATTING

Dit proefschrift verheft orthogonal time-frequency space (OTFS) van een puur communicatiegerichte innovatie tot een golfvormfamilie die zowel voor radar geschikt is als voor toekomstige 6G-toepassingen voor geïntegreerde detectie en communicatie (Integrated Sensing and Communication, ISAC). Het onderzoek wordt gedreven door de noodzaak om de Doppler-robuustheid van OTFS te behouden en tegelijk drie kernnadelen te ondervangen: (i) het ontbreken van een eerlijke vergelijkende studie met orthogonal frequency-division multiplexing (OFDM) voor radartaken; (ii) de rigide, volledig gevulde tijd-frequentiestructuur die flexibiliteit in meervoudige toegang belemmert; (iii) de hoge piek-gemiddelde vermogensverhouding (PAPR), die hoog-vermogen-bedrijf – cruciaal voor veel detectietoepassingen – beperkt.

Het proefschrift begint met een lekeninleiding in het probleem van gezamenlijke detectie en communicatie, los van de specifieke draadloze elektromagnetische toepassingen die in de rest van het werk worden onderzocht. Dit hoofdstuk motiveert het onderzoek – van de relevantie van ISAC tot de keuze om een bestaande, veelbelovende communicatiegolfvorm te selecteren en aan te passen voor radartaken – en identificeert de belangrijkste kennislacunes en onderzoeksvragen. Tegen deze achtergrond legt hoofdstuk 2 het theoretisch fundament. Het introduceert multicarriergolfvormen en essentiële radarbegrippen, toont de overeenkomsten en verschillen tussen OTFS en OFDM en legt de consistente notatie vast die in het verdere proefschrift wordt aangehouden.

Hoofdstuk 3 beantwoordt de eerste onderzoeksvraag door een familie monostatische radarontvangers voor OTFS en OFDM te ontwikkelen, waarvan de aannames omtrent inter-carrier- en inter-symboolinterferentie strikt op elkaar zijn afgestemd. De studie kijkt verder dan de gangbare opvatting dat OTFS inherent Doppler-immuniteit bezit: zodra beide golfvormen met een identieke gezamenlijke vertraging-Doppler-schatter worden verwerkt, convergeert hun bereik-Doppler-prestatie. Het vermeende OTFS-voordeel blijkt dus te wortelen in de ontvangerarchitectuur en niet in de fundamentele golfvormfysica, waardoor de nadruk verschuift naar algoritmeontwerp.

Hoofdstuk 4 introduceert niet-uniform OTFS (NU-OTFS), een nieuwe golfvorm die kan worden gezien als een generalisatie van OTFS waarbij vertraging-Doppler-symbolen via een niet-uniform inverse symplectische discrete Fouriertransformatie in quasi-willekeurige TF-patronen worden geplaatst. Deze flexibiliteit verbetert de meervoudige-toegangsmogelijkheden van OTFS voor multiple-input-multiple-output-(MIMO)-radar en multi-user-(MU)-communicatie. Realistische hoog-mobiele communicatiesimulaties en de eerste OTFS-radarmetingen in de ether bevestigen dat NU-OTFS zowel de basis-bitfoutverhouding (BER) als de detectienauwkeurigheid behoudt, terwijl het niet-overlappende brontoewijzing en ondubbelzinniger radarparameterschattingen mogelijk maakt.

Hoofdstukken 5 en 6 verdiepen het onderzoek naar NU-OTFS. Hoofdstuk 5 stelt een

low-rank-optimalisatieraamwerk voor dat de gezamenlijke ambiguïteitsfunctie benut om NU-OTFS-TF-patronen met minimale nevenlobben te ontwerpen en onderzoekt de schaalbaarheid van NU-OTFS naar multi-user- en massieve-MIMO-configuraties in de aanwezigheid van interferentie. Hoofdstuk 6 presenteert het eerste gelijktijdige MIMO-NU-OTFS-radarexperiment in de literatuur met behulp van een polarimetrische radar. De experimenten tonen zeer lage wederzijdse zenderinterferentie en volledige signaalscheidbaarheid op echte hardware, waarmee NU-OTFS wordt gevalideerd voor dichte ISAC-opstellingen met meerdere communicatiegebruikers en radarzenders.

Hoofdstuk 7 bouwt verder op NU-OTFS om de PAPR-barrière te slechten door constant-modulus OTFS (CM-OTFS) te introduceren, de eerste constant-enveloppe-zustergolfvorm van OTFS. Door complementaire reeksen te combineren met de Zak-transformatieformulering van OTFS elimineert CM-OTFS versterkerclipping en levert het aanzienlijk betere prestaties dan vervormde OTFS bij het dynamisch-bereiksprobleem in bereik-Doppler-schatting, terwijl het vergelijkbaar presteert met zuiver OTFS. Hoewel CM-OTFS een lagere datasnelheid heeft dan zuiver OTFS, overtreft het vervormde OTFS tevens op communicatietaken wat betreft symboolherstel.

Samenvattend levert dit proefschrift een coherente toolkit die (i) de ware oorsprong van het OTFS-waarnemingsvoordeel verduidelijkt, (ii) via het grondig bestudeerde NU-OTFS OFDM-achtige planningsvrijheid biedt, en (iii) een alternatief aanreikt om het PAPR-knelpunt te verwijderen via CM-OTFS. Gezamenlijk ondersteunen deze bijdragen OTFS als een praktisch inzetbare kandidaat voor volgende-generatie-ISAC-netwerken die dichte MIMO-operatie, gefragmenteerde spectrumbenutting en hoogvermogen-front-ends vereisen.

1

INTRODUCTION

"If I'm sincere today, what does it matter if I regret it tomorrow?"
— José Saramago

1

1.1. COMMUNICATION AND PERCEPTION

Most, if not all, life is able to perceive its environment in some way. Some life does it through complex sensors such as vision through the eyes and hearing through the ears. Some have simpler forms of perception, such as those enabled by chemical receptors in single-celled organisms, able to detect and follow chemical gradients in their surroundings. Perception is crucial for any system operating in a physical environment, including living organisms. For humans, it is our interface with reality; it shapes and limits how we *see* the world and how we *imagine* it (if we understand imagination as the ability to simulate sensory input). Perception involves the flow of information from the environment to the individual, be it an artificial system or a living organism. It can be considered a form of one-way communication. However, proper communication stems from the ability to somehow affect the environment in a way that other entities can perceive. Communication requires perception, but it is also something more. Communication is present in many organisms, and its complexity is usually tied to their perception capabilities. From chemical communication through pheromones in ants to visual and auditory communications in birds trying to attract mates, tactile communication in primates' grooming behavior, and ending with the seemingly infinitely complex forms of communication in which we as humans participate. Our direct physical capabilities enable some forms of communication, and technology significantly enhances others. So, from perception arises communication, and they can hardly be separated.

The development of electromagnetic theory and radiofrequency technology mimics the process described above in many ways. As humanity, we devised tools that made us aware of and allowed us to perceive electromagnetic waves outside the visible spectrum, such as the induction experiments of Faraday. Soon, we could generate and perceive electromagnetic waves, and the first electromagnetic-based wireless communication systems were invented. Active sensing through electromagnetic waves and radar arrived soon after, when ships were detected through the transmission and reception of electromagnetic waves. Communication technologies have continued evolving ever since, to the point where they have become one of the defining characteristics of our current era. Radar technology has been crucial in military applications since its inception and has also found its way to many civilian applications, such as aviation, manufacturing, and autonomous mobility. However, the systems that we create usually specialize in either one task or the other. Having both communications and (active) sensing within the same system is rare. Why is that, and should it continue being this way?

1.2. INTEGRATED SENSING AND COMMUNICATIONS

There are many names for the field of research that aims to integrate wireless sensing and communication into multifunctional systems. This dissertation primarily uses integrated sensing and communications (ISAC) to refer to these systems. However, similar terms such as Joint Radar and Communication (JRC) and RadCom are also used in the literature.

Traditional systems segregate the two: radar and communications are engineered

independently, assigned separate bands, and interact only incidentally. Instead, ISAC refers to the deliberate co-design of radar and wireless communications functions so that they not only coexist in a shared frequency band but also, when desired, employ multifunctional systems that perform both tasks at once.

There are good reasons why the radar sensors and the communication systems have been generally distinct [1]. First, they found usage in different fields of society. While wireless communication infrastructure is omnipresent in populated areas (base stations and user equipment such as mobile phones), radar systems are usually mounted in systems and vehicles that have a very specialized purpose (meteorology, detection of airplanes or ships, tracking of targets for interception...) in a very specific setting. Another reason was simply technological: there are challenges in creating a system that simultaneously fulfills the requirements of a good radar and a sound communication system, particularly in terms of hardware. Traditionally, many radar applications related to surveillance require high power, whereas communications require careful and precise phase control.

Technological advances in electronics and manufacturing allow the above reasons to lose some weight [2, 3]. High-frequency radars function more and more like a robust camera or Lidar [4]. They can perceive a complex environment and support other sensors, and are finding their way to robotics [5] and mobility [6] applications that are widespread in society. Advances in radiofrequency hardware allow modern radars to apply complex phase modulations to the signals they transmit [7]. Another driving force for the fusion of radar and communications is the finitude of the available spectrum. As communication and radar applications grow, the possibility of assigning non-overlapping spectra to both applications disappears, and joint solutions must be found [8].

It is not only about the capacity of fusing radar and communications, but also about the benefits of integrating them within multipurpose systems. Apart from the gains in spectrum availability, it seems clear that wireless communication systems can benefit from a better perception of their surroundings to become more efficient [2, 9, 10]. Communication capabilities can also greatly enhance autonomous mobility in complex multi-agent environments where an only-sensing approach, such as autonomous driving [11], drone swarms [12], truck platooning, and autonomous robotics [5], may not be enough.

Even with the technical capability and motivation, many challenges remain in the field of integrated sensing and communications (ISAC). One thought experiment that represents where many of these challenges stem from is the following. Let us imagine a room full of objects we want to see - colorful paintings and sculptures, birds flying around, it does not matter. Imagine that we are there, and we have the task to observe all of this and to communicate it in some way to an observer too far away to be able to discern anything about the room; we are in complete darkness, and all we can do is to turn the flashlight that we carry on and off and choose the color of its light. Clearly, if we prioritize our perception of the environment, we would turn on the flashlight with white light and enjoy the view of the room. However, our far-away observer would not receive any information about the room. We could devise an alphabet based on colors in order to transmit this

information, assuming the observer knows this alphabet. The choice of colors affects the communication of information. More colors mean we can make more words faster and communicate more information. However, it also means a limitation and bias in how we perceive the colors in the room. This trade-off exemplifies the opposing requirements in sensing and communication with radiofrequency and shows some of the design challenges of such systems. However, we chose to tackle this problem, so the question remains of how to proceed.

One could think that there is clearly a specific set of colors that optimizes the integrated perceived and transmitted information, which is likely true. However, the optimal choice would depend on the specific room (or class of rooms) being observed, which is unknown in advance. Moreover, we would have to communicate the optimal alphabet to our observer, which can also be problematic. We choose to tackle the problem differently. Instead of finding the optimal waveform (set of colors) for each case (room), we acknowledge the reality that communication systems are omnipresent, and predefined communication protocols and waveforms exist. Therefore, our aim is to adapt to them to fulfill the sensing requirements. That way, we have no need to redefine the language all of our systems understand, but rather make minor adaptations. This dissertation explores the radar capabilities of modern and future multicarrier communication waveforms. I aim to find ways to use and appropriately change them to optimize their radar (sensing) performance. The goal is to develop realistic solutions that enhance perception while preserving compatibility with legacy communication systems, expanding their capabilities.

This dissertation presents advancements in radar technology, focusing on integrating radar and communication systems by exploring the radar capabilities of modern and future communication waveforms. Specifically, I aim to explore the radar capabilities of multicarrier waveforms with a clear focus on the Orthogonal Time Frequency Space (OTFS) waveform. This dissertation will employ a multi-faceted approach that combines theoretical analysis, simulation, and experimental validation to achieve this.

1.3. WHY ORTHOGONAL TIME FREQUENCY SPACE?

Orthogonal Time Frequency Space (OTFS) [13] is an innovative waveform that has gained attention for its potential to enhance communication and sensing capabilities [14]. OTFS was proposed as an alternative to traditional orthogonal frequency division multiplexing (OFDM), omnipresent in modern communications, from Wi-Fi to Bluetooth and 4G/5G cellular communication [15–17]. OFDM arranges the information in orthogonal subcarriers that coexist closely in frequency but, under ideal conditions, do not interfere with each other [18]. Multicarrier waveforms based on OFDM have seen a lot of attention in ISAC implementations due to their ubiquity in communication standards and good radar performance without significant changes in communication frame structures and system design [19–21]. However, OFDM presents a key drawback in ISAC applications: a low tolerance

to high Doppler shifts [22, 23]. Both in communications and radar applications, performance decreases as the Doppler shift in the signal increases to levels above a fraction of the subcarrier separation [14]. This Doppler sensitivity narrows the range of viable waveform parameterizations; other configurations, while potentially advantageous, can aggravate Doppler-related issues [22]. This drawback is even more problematic in high-mobility scenarios, such as automotive or drone platforms, which are key ISAC applications.

One of the primary motivations for selecting OTFS in this research is its ability to effectively handle high mobility scenarios [24]. In autonomous driving or drone operations applications, the relative motion between the transmitter and receiver can significantly impact communication quality. The inherent robustness of OTFS against these variations means that it could provide reliable performance even as conditions change rapidly. When compared with OFDM, OTFS also has a shorter cyclic prefix (CP) [25] and lower peak-to-average power ratio (PAPR) in typical usage scenarios [26], making this waveform a candidate for potential improvement over OFDM modulations in high-mobility scenarios. While studies of the communication performance of OTFS confirm an improved communication rate and Doppler shift insensitivity at the cost of a more complex channel estimation scheme [14], the interest in the potential of OTFS for radar and ISAC applications is more recent. Unlike OFDM, OTFS utilizes a two-dimensional modulation scheme simultaneously occupying both time and frequency domains [13]. This unique characteristic allows for greater resilience to Doppler shifts and multipath fading, making it particularly advantageous in dynamic environments [27].

1.4. OTFS RADAR: STATE OF THE ART AND CONTRIBUTIONS

While studies of the communication performance of OTFS confirm an improved communication rate and Doppler shift insensitivity at the cost of a more complex channel estimation scheme [14], the interest in the potential of OTFS for radar and ISAC applications is quite recent. Several studies prior to this dissertation have developed joint range-Doppler receivers for OTFS [28, 29] in an analog manner to how pilot-based channel estimation for communications would be implemented. These receivers are able to deal with high-Doppler shifts without the degradation present in OFDM, albeit at a higher computational cost. The increased Doppler robustness is attributed to the structure and properties of OTFS. However, prior to the work in this dissertation, it remains unclear whether these advantages in radar sensing are due to waveform physics or rather due to the higher complexity of the radar receiver. Moreover, it is not explored whether a similar type of receiver could be adapted to work with OFDM radar. In fact, a recent study [30] shows that the claims of Doppler robustness in OTFS communications are tied to the design of the receiver and its increased complexity, and not only to waveform properties. This gap in the literature gives rise to the first research question that I aim to answer within this dissertation:

Q1: *How do the differences in structure between OFDM and OTFS translate to radar*

sensing, and does the Doppler resilience of OTFS in communications transfer to monostatic radar sensing?

While range and Doppler estimation are crucial parts of radar sensing, estimating the angular position of targets through array processing is central to many radar applications. The achievable angular resolution of a radar system is limited by the aperture of the sensing array, which is, in turn, limited by the number of channels for a given array sparsity factor. MIMO radar relies on the separability of the signals emitted by transmitters in different positions to increase angular resolution. Signal separability is a requirement partially shared with the communication function to enable simultaneous access for multiple users sharing the same band. In OFDM ISAC applications, this is achieved primarily through subcarrier interleaving [31, 32]. This limits the unambiguous range of the radar. Alternatives such as random or optimized assignment of the subcarriers have been proposed [33, 34] to reduce ambiguities at the cost of reduced dynamic range.

The possibilities for user/transmitter multiplexing in OTFS are limited, as the signal spreads over the time-frequency domain, leading to symbol overlap and difficulties in signal separability. Only a few proposed solutions to this challenge are available in recent literature. The approach in [35] multiplexes the signals in the delay-Doppler domain. Although this system design retains many of the advantageous properties of OTFS over OFDM, it incurs higher computational complexity due to the joint estimation of the range and Doppler parameters. This approach to signal multiplexing gives up separability in the time-frequency domain, resulting in reduced spectrum flexibility and overlapping time-frequency signal representations for different transmitters/users, reducing its compatibility with applications that require multi-user communications or dynamic interference avoidance. Specific delay-Doppler signal representations allow for separability in the time-frequency (TF) domain and enable multiple access in OTFS communications [36]. The resulting signals are specific, uniform patterns of time-frequency resource allocation. Such representations are helpful for user separation, but reduce the non-ambiguous radar parameter estimation or resolution, and are less able to adapt to dynamic interference. This situation gives rise to the second research question that I aim to address in this dissertation

Q2: *What are practical ways of enabling flexible time-frequency multiple access for MIMO radar and MIMO/multi-user communications for OTFS?*

Finally, I aim to address a somewhat separated but central problem of OTFS radar. Similarly to OFDM, OTFS is not a constant modulus waveform [26]. That means that the instantaneous power of the transmitted signal at any given time is not constant, but instead varies depending on the transmitted symbols, and it is best modelled as a random variable. This can be a deal-breaker for some ISAC applications, due to hardware compatibility. Many radar applications use constant-power waveforms so they can be amplified with non-linear power amplifiers, thus maximizing output power and reducing system cost. However, such a system would distort non-constant power waveforms such as OTFS and OFDM.

While OTFS offers situationally advantageous PAPR characteristics [26], it is far from being enough to avoid signal distortion. Several solutions impair radar and communication performance. Although some solutions with diverse trade-offs are available in the literature for OFDM [37, 38], to the best of the authors' knowledge, none have been developed for OTFS. This motivates the first and final question I aim to address in this dissertation:

Q3: *How can a constant-envelope (or ultra-low-PAPR) OTFS waveform be designed, such that it preserves its delay–Doppler sensing fidelity and key communication characteristics?*

1.5. OUTLINE OF THE DISSERTATION

To present the results, this thesis is organized as follows. First, I investigate the structure of multicarrier waveforms and OTFS, examining their implications for radar applications. A mathematical model is then introduced to establish the framework within which specific findings and innovations are derived. The principal sections of the thesis and their contributions to the state of the art are arranged in the following chapters:

1.5.1. MULTICARRIER RADAR FOR INTEGRATED SENSING AND COMMUNICATIONS

In this chapter, the structure of OTFS is examined in depth to assess its impact on both communication and radar performance. The fundamental concepts employed throughout the thesis are defined here, providing the groundwork for the chapters that follow. The relationship between orthogonal OFDM and OTFS is then analysed. By highlighting their similarities and differences, I identify the root causes of the open problems in OTFS radar sensing and outline potential solutions that underpin the contributions made to the field of OTFS-based integrated sensing and communication. This chapter includes content from:

A. Correas-Serrano, N. Petrov, M. Gonzalez-Huici and A. Yarovoy, "Emerging Trends in Radar: OTFS-Based Radar for Integrated Sensing and Communications Systems," in IEEE Aerospace and Electronic Systems Magazine, vol. 40, no. 6, pp. 102-107, June 2025.

1.5.2. RADAR RECEIVERS FOR OFDM AND OTFS WAVEFORMS

This chapter examines the structure of radar receivers designed for multicarrier waveforms in general and for OTFS and OFDM in particular. The aim is to determine whether the features that give OTFS an advantage in high-mobility communications also benefit monostatic radar sensing. The similarities and differences between the

two waveforms in this radar context are analysed, and a set of radar receivers with distinct characteristics is proposed for each waveform. This chapter is an extension the the following conference publication:

A. Correas-Serrano, N. Petrov, M. Gonzalez-Huici and A. Yarovoy, "Comparison of Radar Receivers for OFDM and OTFS waveforms," 2022 19th European Radar Conference (EuRAD), Milan, Italy, 2022, pp. 1-4.

1.5.3. NU-OTFS: MIMO OTFS WITH ARBITRARY TIME-FREQUENCY ALLOCATION

In this chapter, the MIMO radar and multi-user communication capabilities of OTFS are investigated. The discussion centres on the multiple-access problem in the time-frequency domain. Because OTFS symbols are defined in the delay–Doppler domain and subsequently spread across the time–frequency plane, the waveform's spectral flexibility is restricted, hindering its ability to multiplex transmitters in MIMO radar and to support multi-user communications. To address this limitation, I introduce a generalised OTFS frame-generation procedure that enables arbitrary allocations of time–frequency resources for a given OTFS message, thereby enhancing spectral agility. The resulting waveform, designated Non-Uniform OTFS (NU-OTFS), is validated through theoretical analysis, numerical simulations, and single-transmitter NU-OTFS measurements: This chapter is largely based on the following publication:

A. Correas-Serrano, N. Petrov, M. Gonzalez-Huici and A. Yarovoy, "MIMO OTFS With Arbitrary Time-Frequency Allocation for Joint Radar and Communications," in IEEE Transactions on Radar Systems, vol. 1, pp. 707-718, 2023.

1.5.4. DESIGN OF TIME-FREQUENCY ALLOCATION PATTERNS FOR MIMO NU-OTFS

This chapter examines the range–Doppler estimation performance of NU-OTFS MIMO radar frames as the number of transmitters increases and spectral availability varies. I develop a non-convex optimisation framework based on the simulated-annealing algorithm to identify advantageous time–frequency patterns for radar operation. The resulting analysis clarifies the degrees of sparsity and interference that NU-OTFS MIMO radar can tolerate and offers guidelines for future ISAC system design and implementation, leading to the following publication:

A. Correas-Serrano, N. Petrov, M. Gonzalez-Huici and A. Yarovoy, "Optimized Time-Frequency Allocation in MIMO NU-OTFS Radar for Enhanced Performance Under Spectral Constraints," 2024 IEEE Radar Conference (RadarConf24), Denver, CO, USA, 2024, pp. 1-6.

1.5.5. EXPERIMENTAL VALIDATION OF NU-OTFS RADAR WITH POLARIMETRIC MEASUREMENTS

This chapter extends the previous analysis by validating NU-OTFS radar with MIMO radar measurements. The ability of NU-OTFS to multiplex transmitters or users had not yet been fully tested experimentally in the previous chapters; to address this gap, I use a fully polarimetric MIMO radar to demonstrate, through measurements, its capability for time–frequency multiplexing of OTFS signals with arbitrary time-frequency patterns and minimal cross-channel interference. The content of this chapter was presented in the following publication:

A. Correas-Serrano, N. Petrov, M. Gonzalez-Huici and A. Yarovoy, "Experimental Validation of NU-OTFS MIMO Radar through Polarimetric Measurements," 2024 21st European Radar Conference (EuRAD), Paris, France, 2024, pp. 63-66.

1.5.6. CONSTANT MODULUS OTFS

This chapter addresses one of the remaining open problems in OTFS—the waveform's non-uniform amplitude. Drawing on approaches developed for OFDM, I propose an information-encoding scheme that yields constant-modulus OTFS frames, making the waveform suitable for high-power applications without the risk of amplifier-induced amplitude or phase distortion. The properties of this new waveform, referred to as Constant-Modulus OTFS (CM-OTFS), are analysed, and techniques are introduced to mitigate the associated trade-offs in communication capacity. The work in this chapter lead to the publication of the following journal article:

A. Correas-Serrano, N. Petrov, M. A. Gonzalez-Huici and A. Yarovoy, "Constant Modulus OTFS Based on Zak Transform of Complementary Sequences for Joint Radar and Communications," in IEEE Transactions on Radar Systems, vol. 3, pp. 1131-1144, 2025.

1.6. NOTATION

Throughout this dissertation, $\mathbf{A}^{\mathrm{H}}$ and $\mathbf{A}^{-1}$ denote, respectively, the conjugate transpose and the inverse of a matrix $\mathbf{A}$. The operator vec($\mathbf{A}$) stacks an $N \times M$ matrix $\mathbf{A}$ into the column vector $\mathbf{a} \in \mathbb{C}^{NM\times 1}$, while $\mathrm{vec}^{-1}_{N\times M}(\mathbf{a})$ performs the inverse reshaping. For a vector $\mathbf{b} \in \mathbb{C}^{N\times 1}$, diag($\mathbf{b}$) forms the $N \times N$ diagonal matrix whose main diagonal equals $\mathbf{b}$. The symbol $\odot$ designates the element-wise (Hadamard) product. Vector dependencies are indicated by $\mathbf{a}(n)$, individual components by $a[m]$, and subscripts distinguish related vectors, e.g., the complementary sequence pair $\mathbf{c}_1$ and $\mathbf{c}_2$.

2

MULTICARRIER RADAR FOR INTEGRATED SENSING AND COMMUNICATIONS

"The purpose of a storyteller is not to tell you how to think, but to give you questions to think upon."
— Brandon Sanderson

This chapter introduces the theoretical foundation for using multicarrier waveforms in integrated sensing and communications (ISAC), with a focus on OFDM and OTFS. Emphasis is placed on their radar-specific properties, including range, Doppler, and angle estimation, as well as the challenges they pose for waveform design. Particular attention is given to the issues of transmitter separability in MIMO radar and the high peak-to-average power ratio (PAPR) inherent to multicarrier signals. These challenges motivate the core research directions of this thesis: improving OTFS radar receiver performance, enabling efficient MIMO and multiuser operation, and formulating OTFS waveforms suitable for high-power radar systems.

2.1. A RADAR SCIENTIST'S TAKE ON ISAC

Radar technology has evolved significantly over the past few decades, driven by the need for more accurate and efficient systems in various applications, including automotive [6, 39–41], aviation, and manufacturing sectors. As radar technology continues to evolve, researchers and engineers face a critical challenge: the congested electromagnetic spectrum. With an increasing number of devices competing for limited frequency resources, it becomes essential to develop systems capable of operating efficiently within these constraints.

Sensing systems share spectrum with wireless communication systems, resulting in a crowded spectrum in which both functions avoid overlapping [8]. A high percentage of frequency bands remains reserved exclusively for various radar applications, becoming inaccessible to communication providers, although it is not constantly exploited by radar systems. This situation, further motivated by the advent of software-defined transmitters/receivers and cognitive radio [42, 43], has prompted a renewed interest in radar concepts that are compatible in some sense with communications in the same bandwidth. This compatibility can take the form of either coexisting or multifunctional ISAC concepts [1]. Within this thesis, we focus on a waveform-centric approach to ISAC, but other approaches also fall under the same umbrella term.

The more practical efforts in waveform-centric ISAC consist of adapting known communications or radar waveforms so that both functions can be achieved. The necessity of ISAC has led to two primary approaches: adapting existing radar waveforms, such as frequency modulated continuous wave (FMCW), or leveraging multicarrier communications waveforms, such as orthogonal frequency division multiplexing (OFDM) and orthogonal time-frequency space (OTFS).

FMCW-based ISAC systems, while extensively studied, face intrinsic limitations in communication capabilities due to their narrowband nature and rigid frequency modulation structure. Nonetheless, FMCW is one of the most popular radar waveforms, and multiple attempts to design ISAC systems based on it have been investigated. Some of them are in the form of protocols for medium access control (Radchat [44], radarMAC [45]), while others try to encode information in phase changes during each chirp [46]. The resulting data rates of the proposed solutions are low, and communication remains secondary to radar operation.

In contrast, multicarrier waveforms offer greater flexibility but introduce challenges such as high-speed ADC requirements and peak-to-average power ratio (PAPR) issues. Multicarrier radar based on the orthogonal subcarrier principle was first investigated two decades ago in [47] under the label of multicarrier phase-coded (MCPC) waveform [47]. In this work, multicarrier pulses with intra-pulse phase coding were proposed strictly as a radar waveform. This idea was further developed years later in [20, 21, 48] to accommodate existing multicarrier communications waveforms, namely cyclic prefix-OFDM (CP-OFDM) and repeated-symbol OFDM (RS-OFDM). By using an existing modulation for communications and designing a radar receiver around its frame structure, a truly multifunctional waveform is possible. Following its introduction, numerous radar aspects of this waveform have been investigated, with some strategies to tackle some of its shortcomings such

as the required high speed ADCs [49], variable envelope and high peak-to-average power ratio (PAPR) [50], intercarrier de-orthogonalization due to Doppler shift [23, 51] and non-trivial approaches to MIMO-OFDM [32, 34, 52]. Simultaneously, a general model for multicarrier radar was proposed in [53] and used as a base for optimizing multicarrier radar waveforms under interference constraints in [54].

While OFDM has been the dominant waveform for ISAC, its performance degrades in high-Doppler scenarios due to inter-carrier interference (ICI). OTFS offers improved Doppler resilience at the cost of increased receiver complexity [14]. Similar to OFDM, OTFS makes use of a compact time-frequency signal representation to transmit information. Its higher tolerance to Doppler [28, 55] and a shorter cyclic prefix [25] make this waveform a potential improvement over OFDM modulations for radar and ISAC. Unlike OFDM, in which the symbols are defined over the frequency grid, OTFS defines the communication symbols over the "delay-Doppler" plane and spreads them over the time-frequency plane utilizing the discrete symplectic Fourier transform (DSFT). The implications of OTFS to communications and radar are still being investigated, with some works already investigating radar receiver design [28, 55]

The remainder of this chapter is structured as follows: Section 2 provides a short introduction to radar, with a focus on the concepts of matched filter (MF) and ambiguity function (AF). Section 3 introduces the principles of multicarrier waveforms, focusing on OFDM and OTFS. Section 4 explains MIMO and array processing techniques for direction-of-arrival estimation. Finally, Section 5 reviews the state-of-the-art in MIMO-OFDM and OTFS radar, highlighting current challenges and research directions.

2.2. FUNDAMENTALS OF RADAR: MATCHED FILTER AND AMBIGUITY FUNCTION

This thesis assumes some level of knowledge about radar systems. Nonetheless, in this section, we introduce some key concepts of radar signal processing. For a more in-depth description of radar principles, hardware, and types of radar systems, we redirect the reader to textbooks such as [56, 57]

The functioning principle of radar relies on the emission and reception of electromagnetic radiation to estimate parameters of the illuminated environment, based on its effect on the transmitted signals. Typically, this involves the transmission of a modulated electromagnetic wave (e.g., a pulse), the reception of its echoes in the environment, and the comparison between the transmitted and received signals. The primary function of a radar is the detection of objects and estimation of their parameters, such as distance, radial velocity, and direction. Based on the radar returns, other high-level parameters can be estimated in function-specific radars, such as precipitation on a weather radar, or orbit in a space observation radar.

In this section, we focus on two key concepts related to radar that are mentioned throughout this thesis. These concepts are the matched filter and the ambiguity function of a waveform. The matched filter is a fundamental receiver operation in radar systems, designed to maximize the signal-to-noise ratio (SNR) for a known

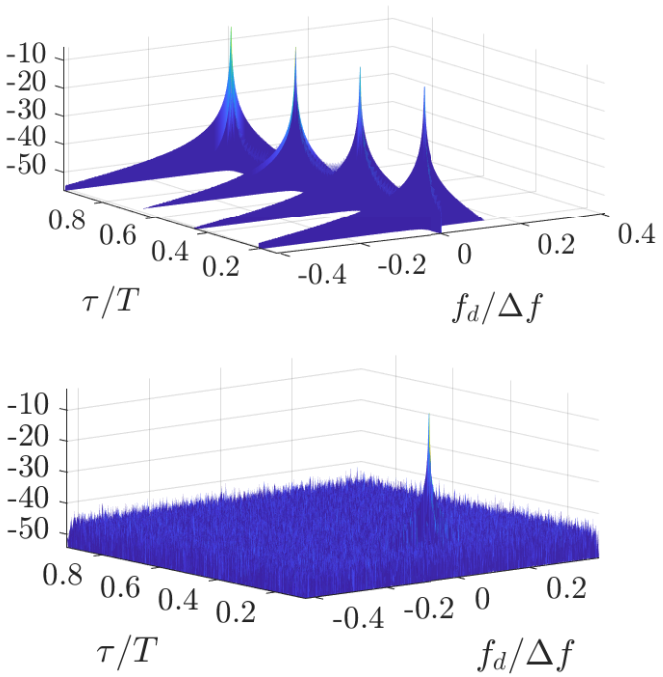

Figure 2.1: Ambiguity functions with different sidelobe structures. The top example shows ambiguities (grating lobes), whereas the bottom example shows an increased sidelobe level without ambiguities.

transmitted waveform in the presence of additive noise. It operates by correlating the received signal with a time-reversed and conjugated version of the transmitted waveform, effectively aligning their structures in time to enhance detectability. A matched filter can be implemented directly in analog hardware, as is the case in many high-power applications, or through digital signal processing.

For a single-input single-output (SISO) radar system, the output of the matched filter as a function of time delay τ and Doppler frequency f_D is captured by the ambiguity function (AF). The delay and Doppler AF of a waveform can be written in a generic way as the correlation of itself with time and frequency-shifted versions of itself

$$\chi(\tau, f_D) = \int_{-\infty}^{\infty} s(t)\, s^*(t-\tau)\, e^{i2\pi f_D t}\, dt \tag{2.1}$$

where $s(t)$ is the transmitted signal, and $s^*(t-\tau)$ is its complex conjugate delayed by τ. The exponential term accounts for the Doppler shift. This function provides a measure of the matched filter's response to targets at different delays and Doppler frequencies, and can be evaulated in all relevant range-Doppler hypothesis pairs.

The range-Doppler ambiguity (AF) function essentially gives two main pieces of

information about the associated waveform. The first is the parameter estimation resolution achievable with the waveform. In the case of radar, this indicates how well we can separate targets that have very close range and radial speed parameters. This can be estimated from the characteristics of the mainlobe of an AF. The second piece of information we can get directly from the AF is how the presence of a target with parameters $\{\tau_0, \nu_0\}$ interferes with the ability to identify another target with a different set of parameters $\{\tau, \nu\}$. The sidelobe level of the AF defines this metric, and it is crucial to consider as it leads to target masking, in which bright targets "mask" darker targets in the estimation process. Effectively, it is linked to the dynamic range associated with a specific waveform, although other factors during signal processing can come into play when defining the dynamic range of a radar system. The two exemplary ambiguity functions shown in Fig. 2.1 can be used to illustrate these concepts: In the top AF, the overall sidelobe level is low (indicating a high dynamic range), but the mainlobe "repeats" in the time dimension. These mainlobe replicas indicate ambiguities that limit the parameter estimation range, and are often referred to as grating lobes. The AF at the bottom of Fig. 2.1 shows a higher constant sidelobe level, but no rating lobes. From the AF alone it is possible to understand that both waveforms will have similar resolution, and that the waveform above will have a higher dynamic range but smaller unambiguous parameter estimation range than the waveform below.

It is worth noting, however, that the AF is not always the most informative metric for all waveform classes. For multicarrier waveforms such as OFDM, the range profile is obtained in the frequency domain through spectral division and inverse Fourier transforms, rather than directly from the waveform autocorrelation. Thus, while the AF in Eq. 2.1 still provides insight into Doppler coupling and sidelobe behavior, it does not fully characterize the effective range resolution. For this reason, in later chapters we sometimes compare the output of specific radar receivers instead of relying solely on the AF. Furthermore, the concept of ambiguity functions can be defined for other estimation problems, such as the angular estimation capabilities associated with a digital antenna array (also common in radar), and are commonly used as a metric for sparse antenna array designs [58, 59]. Moreover, one can derive AFs that take into account transmitter coupling when multiple-input-multiple-output (MIMO) radar is used [60]. This is important when designing a waveform for MIMO radar operation, and will be revisited in Chapter 4.

2.3. MULTICARRIER WAVEFORMS FOR ISAC: OFDM AND OTFS

Multicarrier waveforms are present in almost all forms of wireless and cellular communication systems, and understanding their radar capabilities is of great interest for ISAC. In this section, we present the structure of OTFS and OFDM, as well as a generalized multicarrier radar model that offers a compact notation for both OTFS and OFDM radar. OTFS and OFDM share a lot of characteristics, and presenting them separately may feel cumbersome to the reader. However, we believe that having a clear, separate understanding of the inner structure of both waveforms

is key to understanding the contributions to OTFS ISAC systems made in this thesis.

2.3.1. PRINCIPLES OF OFDM

OFDM operates under the principle of orthogonal multicarriers, in which information is encoded in closely spaced frequencies (subcarriers) that do not interfere with one another (i.e., they are orthogonal). To achieve this, the length of each pulse (or OFDM symbol) T has to fulfill

$$T = 1/\Delta f, \tag{2.2}$$

where Δf is the subcarrier separation. OFDM is the waveform at the physical layer of 4G and 5G communications, ensuring high data rates in combination with MIMO techniques and adaptive beamforming. Consider an OFDM system with N subcarriers; the multicarrier time-domain signal is comprised of the sum of these carriers. In the discrete domain, and fulfilling the orthogonality condition in (2.2), the signal sampled in $t = n_s T/N, n_s \in [0, N)$ can be written as

$$s_0[n_s] = \frac{1}{\sqrt{N}} \sum_{n=0}^{N-1} x[n] e^{j2\pi \frac{nm}{N}} \tag{2.3}$$

where $x(n)$ is the complex amplitude representing the communication symbol that modulates the n-th subcarrier. The signal model in (2.3) mimics the inverse discrete Fourier transform (IDFT) structure, and is usually implemented in the digital domain with it. In fact, the orthogonal multicarrier principle relies on the alignment of the *sinc* functions resulting from the DFT of time-limited rectangular pulses, and it is where the sampling requirement in (2.2) stems from. The OFDM signal is then transformed to the analog domain with a digital-to-analog converter (DAC) and modulated with a transmission pulse g_{tx}, such that

$$s_0(t) = \frac{1}{\sqrt{N}} \sum_{n=0}^{N-1} g_{tx}(t) x[n] e^{j2\pi f_n t} \tag{2.4}$$

where $f_n = n\Delta f$ denotes the frequency of the n-th subcarrier, and the transmit pulse $g_{tx}(t)$ is assumed to be an ideal rectangular function.

$$\text{rect}\left(\frac{t}{T + T_{\text{CP}}}\right) = \begin{cases} 1, & 0 \le t \le T + T_{\text{CP}} \\ 0, & \text{otherwise} \end{cases} \tag{2.5}$$

Although the rectangular pulse assumption is common in the literature about multicarrier waveforms, the synthesis of such pulses is impossible, and work on pulse design for multicarrier waveforms can be found in [25, 61]. It is usual for OFDM systems that a sequence of OFDM pulses is transmitted, and it is particularly useful to consider it that way for radar applications, where multiple symbols constitute a radar frame. The transmission of multiple OFDM symbols separated by a cyclic prefix (CP) can be written as

$$s(t) = \sum_{n=0}^{N-1} \sum_{m=0}^{M-1} \mathbf{X}_{\text{TF}}^{\text{OFDM}}[n, m] g_{tx}(t - m(T + T_{\text{CP}})) e^{j2\pi n \Delta \text{f}(t - m(T + T_{\text{CP}}))} \tag{2.6}$$

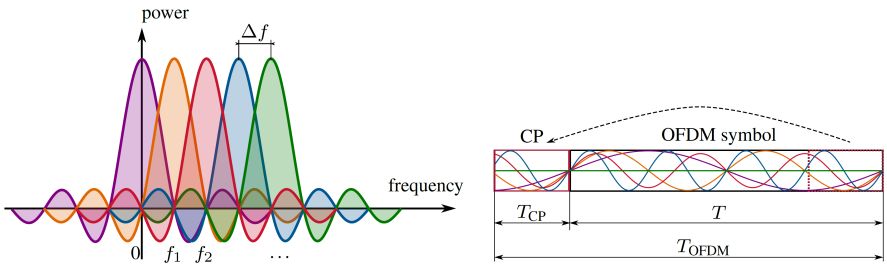

Figure 2.2: On the left, depiction of an OFDM symbol in the frequency domain. The maximum of the frequency representation of each subcarrier aligns with the nulls of the rest (i.e., they are orthogonal). On the right, time representation of an OFDM symbol. The symbol is the superposition of all the subcarriers and is preceded by a cyclic prefix. Figure reproduced from [19].

where $\mathbf{X}_{\text{TF}}^{\text{OFDM}} \in \mathbb{C}^{N \times M}$ is a matrix formed by the concatenation of M OFDM symbols $x(n)$, each with N subcarriers. In between symbols, a cyclic prefix (CP) of duration T_{CP} (a fraction of the symbol duration) is appended before transmission. The cyclic prefix is a repetition of the last samples of the time-domain signal that is appended at the beginning of the signal. It prevents inter-symbol interference (ISI) in both radar and communications by simplifying multipath scenarios into a multitude of circular shifts in the signal. This assumption is valid as long as the cyclic prefix is longer than the maximum delay spread of the channel (communications) and the delay associated with the farthest relevant target (radar). The frequency and time-domain structure of an OFDM symbol is shown in Fig. 2.2, and the structure of a sequence of symbols forming a radar frame is depicted in the left half of Fig. 2.3. Finally, the signal (frame) is modulated to the desired carrier frequency

$$s_{\text{RF}}(t) = s(t) e^{j2\pi f_c t} \tag{2.7}$$

where f_c is the carrier frequency. So far, the signal model for communications and radar sensing is the same. However, the signal models diverge when it comes to the monostatic radar received signal. The received signal after propagation in a smooth medium and reflection in P targets is

$$y_{\text{RF}}(t) = \sum_{p=0}^{P-1} a_p \; s_{\text{RF}}\big(t - \tau_p\big) e^{j2\pi f_{D,p}(t-\tau_p)} \tag{2.8}$$

where we assume that the delay associated with a single path is not changing during the frame time (no range migration assumption), and the Doppler shift is also constant during the frame time (no acceleration assumption). Methods to deal with range migration if OFDM have been researched in [62].

While OFDM provides a convenient single-dimension (frequency-only) packing of symbols and is therefore well matched to existing 4G/5G transceivers, its radar

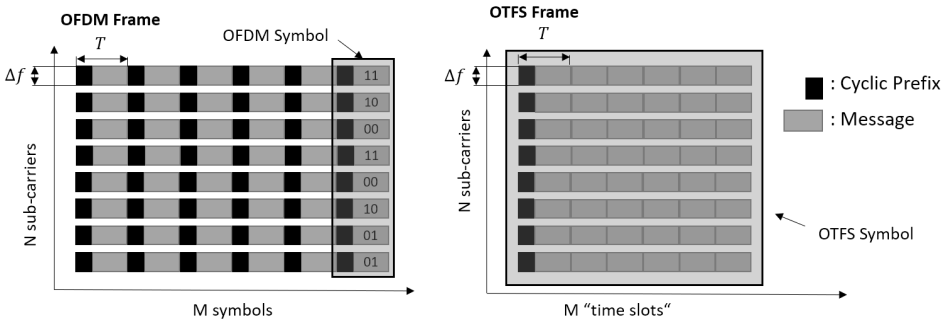

Figure 2.3: Structure of an OFDM and an OTFS radar frame side by side, where the differences in cyclic prefix and frame structure can be observed. In OFDM, multiple symbols with a cyclic prefix are concatenated to have a two-dimensional signal (fast-time and slow-time) to estimate the range and Doppler parameters, respectively. In OTFS, a single symbol is spread over time and frequency, and can be used effectively as a frame for range-Doppler estimation.

and high-mobility performance is ultimately constrained by two structural features: the reliance on a cyclic prefix, which sacrifices useful energy or bandwidth, and the sensitivity of its per-subcarrier processing to Doppler shifts that approach a non-negligible fraction of Δf. A natural way to overcome both issues is to abandon the one-dimensional sub-carrier view and embed the information symbols directly on the two-dimensional delay–Doppler. The resulting multicarrier scheme, Orthogonal Time–Frequency Space (OTFS), retains all of OFDM's implementation assets (FFT-based modulation, compatibility with legacy hardware) yet redistributes each information symbol over the entire time–frequency plane, achieving improved Doppler resilience. The next subsection introduces the OTFS signal model and shows how its delay–Doppler formulation generalises the OFDM framework developed above.

2.3.2. PRINCIPLES OF OTFS

OTFS can be seen as an extension or generalization of OFDM. As introduced in the previous section, OFDM arranges the communication symbols in a 1D arrangement that can be seen as orthogonal subcarriers. These subcarriers are modulated into a time-domain signal through a DFT transform. OTFS instead arranges the symbols in a 2D format that represents the so-called delay-Doppler domain, and is then mapped to the time-frequency domain by means of the Inverse Symplectic Finite Fourier Transform (ISFFT). Consider a single transmitter OTFS system transmitting a message $\mathbf{X}_{\mathrm{DD}} \in \mathbb{C}^{N\times M}$ defined in a $N \times M$ delay-Doppler grid, with N delay bins and M Doppler bins. The number of subcarriers and subsymbols in TF representation is N and M, respectively. The communication symbols are mapped

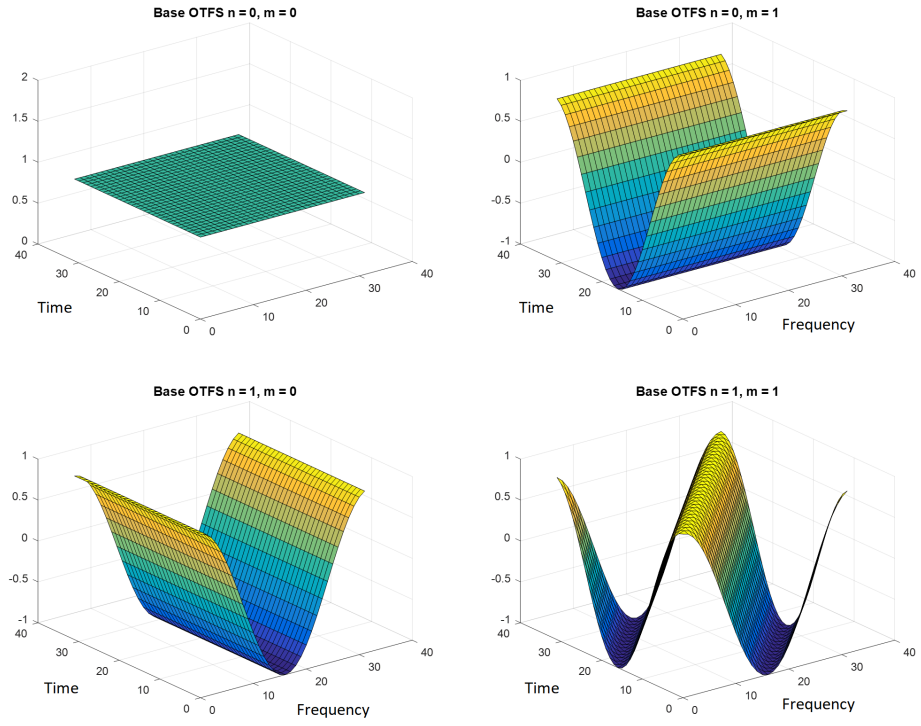

Figure 2.4: Example of the real part of the time-requency representation of OTFS symbols in the delay-doppler indices [0,0], [0,1]. [1,0], and [1,1]. An OTFS symbol representation in the time-frequency domain is the superposition of these $N \times M$ such bases with phase and/or amplitude shifts depending on the communication symbol modulation.

to the time-frequency domain through the ISFFT such that

$$\mathbf{X}_{\mathrm{TF}}^{\mathrm{OTFS}}[n,m] = \frac{1}{\sqrt{NM}} \sum_{k=0}^{N-1} \sum_{l=0}^{M-1} \mathbf{X}_{\mathrm{DD}}[k,l] e^{j2\pi\left(\frac{ml}{M} - \frac{nk}{N}\right)} \tag{2.9}$$

where $[k,l]$ are index pairs in the delay-Doppler grid, and $[n,m]$ are index pairs in the time-frequency grid. $\mathbf{X}_{\mathrm{TF}}[n,m]$ is the time-frequency representation of the OTFS symbols, now spread in the time-frequency domain. This intermediate representation is useful for understanding the differences between OFDM and OTFS. The OFDM communication symbols in this domain are localized in each subcarrier, whereas the OTFS symbols are spread over the time-frequency plane. Fig. 2.4 shows an example of the first four canonical bases for OTFS in the TF domain. It shows that localized delay-Doppler bits of information, in this case situated in the delay-Doppler indices $[0,0], [0,1], [1,0]$, and $[1,1]$ become spread 2D oscillating surfaces. A complete OTFS

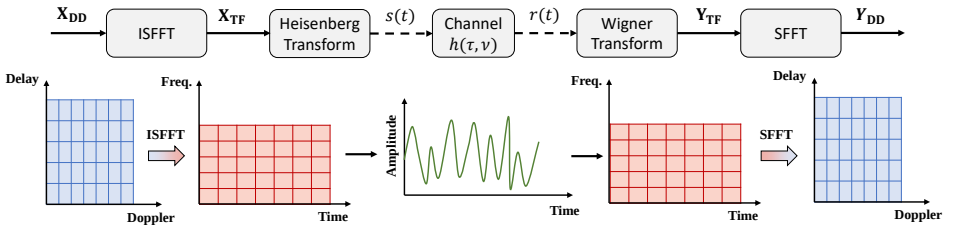

Figure 2.5: Block diagram of the transformations in OTFS signal generation, highlighting the similarities between OTFS and OFDM. OTFS goes from the Delay-Doppler domain to the time domain, passing an optional intermediate time-frequency representation, where OFDM signals are generated. With this system architecture, OTFS can be highly compatible with OFDM legacy systems.

symbol in the TF domain is composed of the integration of all the bases multiplied by an initial phase and/or amplitude, depending on the communication symbol dictionary (e.g., QPSK or QAM).

The TF signal is converted into the time domain for transmission using the Heisenberg transform, as in OFDM. The time domain signal $s(t)$ is given by

$$s(t) = \sum_{n=0}^{N-1} \sum_{m=0}^{M-1} \mathbf{X}_{\mathrm{TF}}^{\mathrm{OTFS}}[n,m] g_{tx}(t-mT) e^{j2\pi n\Delta \mathrm{f}(t-mT)} \tag{2.10}$$

where g_{tx} is the transmit pulse. The sequence of transforms to synthethise, transmit and receive an OTFS signal is depicted in Fig. 2.5. Assuming a rectangular transmit pulse and a critically sampled signal (Nyquist sampling), equations (2.9) and (2.10) can be written in compact matrix notation as

$$\mathbf{X}_{\mathrm{TF}}^{\mathrm{OTFS}} = \mathbf{F}_{\mathrm{N}} \mathbf{X}_{\mathrm{DD}} \mathbf{F}_{\mathrm{M}}^{\mathrm{H}} \tag{2.11}$$

and

$$\mathbf{s} = \mathrm{vec}(\mathbf{F}_{\mathrm{N}}^{\mathrm{H}} \mathbf{X}_{\mathrm{TF}}^{\mathrm{OTFS}}) = \mathrm{vec}(\mathbf{X}_{\mathrm{DD}} \mathbf{F}_{\mathrm{M}}^{\mathrm{H}}) \tag{2.12}$$

where $\mathbf{F}_{\mathrm{N}} \in \mathbb{C}^{N\times N}$ and $\mathbf{F}_{\mathrm{M}} \in \mathbb{C}^{M\times M}$ are normalized Fourier transform matrices. Analogously as with OFDM, the discrete time-domain signal $\mathbf{s} \in \mathbb{C}^{NM\times 1}$ is transformed to the analog domain with a digital-to-analog converter (DAC) before undergoing I/Q modulation to the desired carrier frequency f_c, transmitted and received in a monostatic manner, as in equations (2.7) and (2.8). For this dissertation, narrowband radar operation is assumed in all steps, and therefore $f_c \gg B$, where $B = N\Delta f$ is the bandwidth of the OTFS signal. It is worth noting that from (2.12), the time-frequency representation is a middle step that is not required to synthesize the OTFS time-domain signal. Instead, the Zak transform and its inverse, shown in the right-hand side of (2.12), can be used to go from the delay-Doppler signal representation to the time-domain representation, as depicted in Fig. 2.6. However,

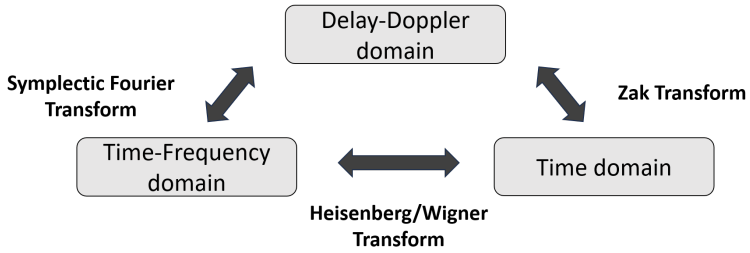

Figure 2.6: Schematic showing the transforms connecting the delay-Doppler, time-frequency, and time domain.

it is important not to overlook the possibility of an intermediate time-frequency representation, as it is relevant for the compatibility of OTFS with legacy OFDM systems. Furthermore, in future chapters, we exploit this intermediate time-frequency representation to increase the flexibility of OTFS for multiuser communications and MIMO radar.

2.4. MIMO MULTICARRIER RADAR

The estimation of the angular direction of the received signal (echo in the case of radar) is not inherent to the waveform used, but is enabled by the radar front-end. Traditionally, a directive antenna was used to scan the area of interest, and the position in space of the estimated target would be given by the direction at which the antenna is pointed. Many modern radar implementations deploy multiple transmitters and receiving elements, an arrangement commonly called MIMO (multiple-input, multiple-output) radar. Instead of relying on a single directive antenna or mechanical scanning, MIMO radar leverages waveforms transmitted from different antenna positions. Each transmitter can emit a known (ideally orthogonal) waveform, and the array of receiving elements collects echoes that preserve the identity of each transmitted signal. The system can infer the angular directions from which reflections originate by comparing how these signals arrive across the array.

One simple way to see this is through the steering vector formulation. Conceptually, for a given angle, each antenna element in the array samples the signal with a predictable phase shift relative to the others, and dependent on the angle of arrival ϕ

$$\mathbf{a}(\phi)_{\text{SIMO}} := \exp\left(j\frac{2\pi}{\lambda}\mathbf{d}^{\text{Rx}}\sin\phi\right) \tag{2.13}$$

where $\mathbf{a}(\phi)_{\text{SIMO}} \in \mathbb{C}^{N_{Rx}}$, $\mathbf{d}^{\text{Rx}} := [d_1^{\text{Rx}},\ldots,d_{M_{\text{Rx}}}^{\text{Rx}}]$ are the positions in the array of the receive channels, and λ is the wavelength of the carrier signal. When a MIMO configuration with multiple transmitters in addition to multiple receivers is used, all the transmitter-receiver pairs are taken into account within the steering vector. This added spatial diversity allows for an increase in angular resolution, with the resulting

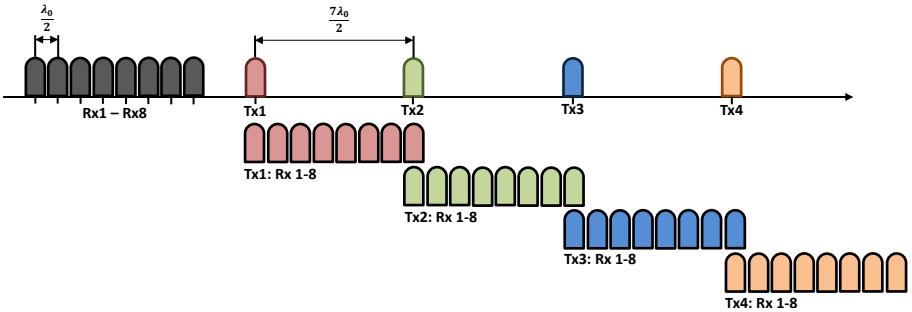

Figure 2.7: Schematic of the virtual array of a 4x8 MIMO radar system.

steering vector $\mathbf{a}(\phi)_{\text{MIMO}} \in \mathbb{C}^{N_{Rx} \times N_{Tx}}$

$$\mathbf{a}(\phi)_{\text{MIMO}} := \exp\left(j\frac{2\pi}{\lambda}(\mathbf{d}^{\text{Tx}} \oplus \mathbf{d}^{\text{Rx}})\sin\phi\right) \tag{2.14}$$

now dependent on both the positions of the transmit and receive elements. The MIMO formulation is often written as a so-called SIMO virtual array in which the receiver element positions $\mathbf{d}^{\text{Virt}} \in \mathbb{C}^{N_{Rx} \times N_{Tx}}$ are defined by

$$\mathbf{d}^{\text{Virt}} = \mathbf{d}^{\text{Tx}} \oplus \mathbf{d}^{\text{Rx}} := [d_1^{\text{Tx}} + d_1^{\text{Rx}}, d_1^{\text{Tx}} + d_2^{\text{Rx}}, \ldots, d_{M_{\text{Tx}}}^{\text{Tx}} + d_{M_{\text{Rx}}}^{\text{Rx}}]. \tag{2.15}$$

The previous equations show that with the same number of physical channels, one can achieve more effective measurements using a MIMO array with both transmitters and receivers. To give a quick numerical example, if we restrict a radar system to have 12 digital array elements, we could achieve a receive array of 11 receive channels with the SIMO configuration, or 36 virtual receive channels with a MIMO configuration of 6 transmitters and 6 receivers. In the case of a uniform linear array, using a MIMO array would improve the resolution by a factor of 3.3. Moreover, the use of multiple transmit channels often implies an increase in the transmitted power, which is also beneficial in radar systems.

While the benefits of using MIMO arrays in terms of are clear, it does not come without added challenges. Introducing multiple transmitters places demands on the radar waveform design. Specifically, each transmitter must radiate a known signal so the receiver can distinguish the different transmit–receive paths, yet all signals must coexist without excessive mutual interference. Balancing these two goals requires selecting (or designing) waveforms that are sufficiently orthogonal so the receive channels can isolate each transmitter's contribution.

MIMO radar relies on the separability of the signals emitted by each transmitter to increase angular resolution and avoid self-interference [63]. In communications, signal separability from different transmitters is also required to enable simultaneous access for multiple users sharing the same bandwidth [64]. Therefore, the ability to multiplex different radar transmitters or communication users such that they are

separable in a receiver is desirable for both radar and communication applications. In OFDM, this can be accomplished by multiplexing the different transmitters directly in the time-frequency (TF) domain, allocating non-overlapping TF bins to different transmitters [64]. Under realistic channel conditions, the signal associated with different transmitters/users can be recovered by filtering the appropriate TF resource blocks in the receiver [65].

OTFS symbols are defined in the delay-Doppler (DD) domain and are later spread in the TF domain through the Inverse Symplectic Finite Fourier Transform (ISFFT). This can be seen in Fig. 2.4, where each subfigure corresponds to the time-frequency representation of a single delay-Doppler cell worth of information. When an entire frame of delay-doppler symbols is sent, they overlap in the TF domain, and different transmitters can not be separated anymore by looking at specific time-frequency bins. To address this challenge, several strategies are possible. Specific DD resource allocations that allow for separability in the time-frequency domain have been studied in [36, 66] for multiple user access for OTFS communications. The resulting TF representation amounts to interleaving or block allocation of transmitters/users in the TF resource plane, as shown in Fig. 2.8, left. Such allocation is problematic for radar applications, as it reduces the non-ambiguous interval or resolution in either range or Doppler domain [33]. The signals could be separated for radar operation using the different messages each transmitter encodes, as shown in Fig. 2.8, middle. However, this approach is not valid for communications, where the receiver has no prior knowledge of the message. Alternative TF allocation schemes, particularly non-uniform optimized [34] or random patterns [33], have shown great promise in OFDM radar applications when paired with sparse reconstruction algorithms. Sparse reconstruction algorithms have shown potential in various aspects of radar signal processing [67] and interference mitigation [68] due to the inherent sparsity of radar data in the delay-Doppler-angle domain. This approach will be explored within this disertation in Chapters 4, 5 and 6, and is depicted in Fig. 2.8, right.

2.5. PAPR IN MULTICARRIER RADAR WAVEFORMS

Due to its military roots, many radar applications are focused on the long-distance detection of targets that do not want to be detected. In order to detect a target hundreds of kilometers away, high power transmission is crucial. Radar systems usually drive their high-power amplifiers to saturation to enable such high-power implementations. For a waveform to go through a saturated amplifier without being substantially distorted, it must always have the same amplitude. The peak-to-average power ratio (PAPR) is a useful metric to measure how closely a waveform resembles a constant-modulus waveform, and is defined as

$$\mathrm{PAPR}\big(x(t)\big) = \frac{\max_t \big|x(t)\big|^2}{\mathbb{E}\Big\{\big|x(t)\big|^2\Big\}}. \tag{2.16}$$

where $x(t)$ is the transmitted signal. Notice that the PAPR of a constant modulus signal is one, and increasing values above one indicate increasing variability in the

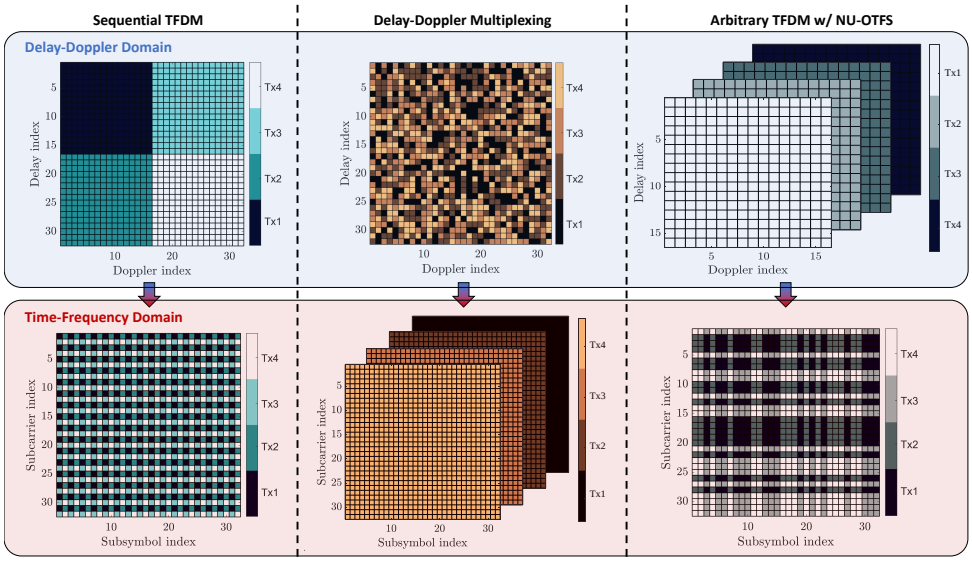

Figure 2.8: Depiction of multiplexing OTFS MIMO radar transmitter multiplexing strategies. On the left, sequential TFDM allows for non-overlapping time-frequency representations of the OTFS signal only in the shown pattern [36]. In the center, arbitrary non-overlapping delay-Doppler multiplexing is transformed into multiple superimposed time-frequency signals [69]. On the right, the NU-OTFS [70] formulation permits multiple OTFS messages (assigned, e.g., to different comms users or radar transmitters) to be multiplexed in arbitrary non-overlapping time-frequency resources.

peak power of the signal with respect to the average. Common waveforms for radar sensing, such as FMCW and pulsed radar, have constant modulus. However, multicarrier waveforms are known to have a high PAPR due to the superposition of the orthogonal subcarriers in the time domain(in the case of OFDM) with different phase and amplitude modulations. In the case of OFDM, when the number of subcarriers N is large, the transmitted samples can be approximated to have a complex Gaussian distribution, and the instant envelope is Rayleigh distributed as a result [26]. OTFS follows the same distribution, although its dependency is on the number of subsymbols, or M. This difference in dependency can be understood intuitively from (2.6) and (2.12). In them, we can see that the transform from the symbol domain to the time-domain signal involves a Fourier transform across subcarriers for OFDM and subsymbols for OTFS. These transforms cause the non-unitary PAPR in the time-domain transmitted signal. In Fig. 2.9 we can see the sample cumulative distribution function (CCDF) of OTFS and OFDM for different numbers of subcarriers and subsymbols, where the dependency just discussed is clearly shown.

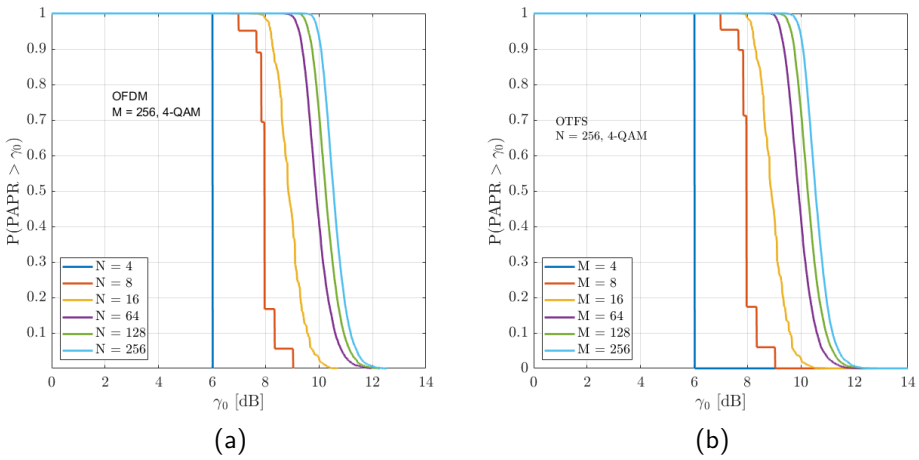

Figure 2.9: CCDF of PAPR of OFDM (a) and OTFS (b) for different values of subcarriers N and subsymbols M.

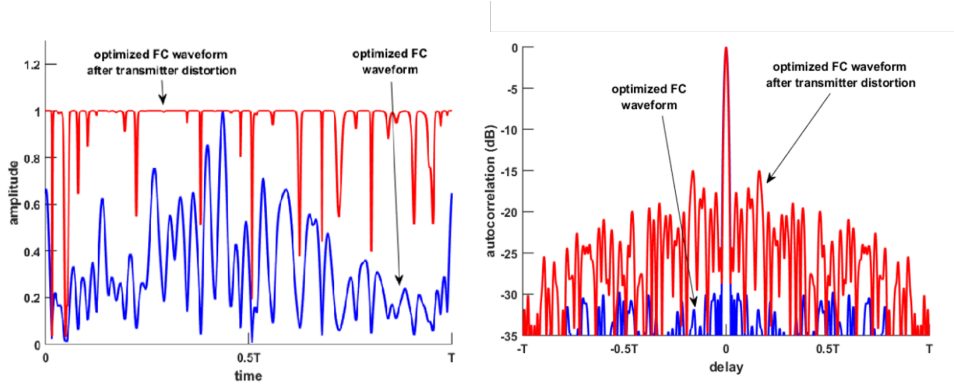

Figure 2.10: Distortion due to non-linear amplification of a non-constant frequency-coded (FC) waveform. On the left, the effect of amplitude clipping in the time-domain signal is shown. On the right, we see the effect of such distortion in the matched filter response of the signal. Images reproduced from [71]

Due to the non-unitary PAPR, multicarrier waveforms are distorted when sent with a system relying on a saturated high-power amplifier. This is usually not an issue in wireless communication, as lower power transmission and amplifiers operating in the linear region are used. However, it is a real problem when considering multicarrier waveforms for multifunctional systems, where radar modes may require high-power transmissions. In Fig. 2.10 we show an example of a saturated amplifier's

effect in a multicarrier signal, both in the time domain and after radar processing. In order to enable multifunctional multicarrier systems, it is important to devise ways to reduce the PAPR of multicarrier waveforms so that they can be used with saturated amplifiers.

2.6. CONCLUSIONS

This chapter has provided the foundational background necessary to contextualize the contributions of this thesis within the broader landscape of ISAC research. Starting from a radar-centric perspective, we introduced the increasing relevance of multicarrier communication waveforms, particularly OFDM and OTFS, in modern multifunctional ISAC systems. By discussing their underlying time-frequency structures, we highlighted how these waveforms can be repurposed for sensing tasks, yet also introduced new challenges in doing so. OFDM's widespread adoption and OTFS's promise in high-mobility scenarios make them compelling candidates, but several technical barriers remain unresolved. Specifically, this thesis addresses three main research challenges: the design of radar receivers for OTFS and their comparison with OFDM; the integration of OTFS with MIMO radar and multiuser communication systems where transmitter separability is critical; and the formulation of low-PAPR OTFS waveforms suitable for high-power operation in practical multifunctional systems. These directions are explored in depth in the following chapters, where we propose and validate new techniques to improve receiver design, waveform separability, and power efficiency. The overarching aim is to advance OTFS as a viable waveform for next-generation ISAC systems, balancing performance and hardware constraints in both radar and communication domains. It is important to note that the above challenges primarily arise in multifunctional ISAC systems, where radar sensing and data transmission must coexist. In contrast, dedicated radar implementations of OFDM or OTFS can circumvent issues such as high PAPR by using constant-modulus codes or repeated symbols, at the cost of transmitting no information. The research directions in this thesis, therefore, focus on the ISAC case, where achieving a balance between radar performance and communication functionality remains an open challenge.

3

RADAR RECEIVERS FOR OFDM AND OTFS WAVEFORMS

"I realised that the search for the Knowledge has encouraged us to think of the House as if it were a sort of riddle to be unravelled, a text to be interpreted, and that if ever we discover the Knowledge, then it will be as if the Value has been wrested from the House and all that remains will be mere scenery."
— Susanna Clarke

In this chapter, a generic description of common multicarrier radar receivers is presented. Two multicarrier waveforms - orthogonal frequency division multiplexing (OFDM) and orthogonal time-frequency spacing (OTFS) - are considered. OFDM and OTFS are strong candidate waveforms for integrated sensing and communication (ISAC) applications. Sensing performances of different waveform-receiver pairs are compared theoretically and through simulations. It is shown that while qualitatively, both waveforms perform similarly under the same receiver, performance differences exist between them.

Parts of this chapter have been published in [72].

3.1. INTRODUCTION

Multicarrier waveforms based on orthogonal frequency division multiplexing (OFDM) are promising in achieving good radar and communications performance without significant changes in existing communication system design. OFDM suffers from inter-carrier interference (ICI) when subject to Doppler shifts above a tenth of the subcarrier separation due to the de-orthogonalization of the subcarriers, affecting both communications and radar performance [22]. Considering that the deployment of radar is often tied to high-mobility scenarios, ICI limits the implementation scenarios of OFDM joint radar and communication systems. For communications, OTFS has been shown to be a good alternative to OFDM in high-mobility scenarios, due to the inherent sparsity and stability of the channel in the delay-Doppler domain regardless of the magnitude of the present Doppler shifts.

The performance of OTFS and OFDM radar has been compared recently in both [55] and [28]. The authors of [55] derive a maximum likelihood receiver for the OTFS waveform considering inter-symbol interference (ISI) and ICI and compare it with the symbol-canceling maximum likelihood receiver for an OFDM signal, which implicitly assumes no ISI/ICI. In [28], a more straightforward matched filter OTFS receiver is developed and compared with an unspecified OFDM radar receiver under moderate ICI conditions, showing a systematic Doppler estimation error in the latter. This effect is inconsistent with the previously reported effect of ICI in OFDM radar behavior (e.g., [23, 73]), which appears as an increase in the noise floor in the estimation.

This chapter first develops a generic description of state-of-the-art OFDM and OTFS monostatic radar receivers from both time–frequency and delay–Doppler perspectives. Building on this common framework, we propose adaptations in the receivers that render the receivers compatible with both waveforms, enabling a fair, unified comparison of the two waveforms. Section 3.2 presents a concise multicarrier radar model; Section 3.3 details the receiver structures; Section 3.4 evaluates each waveform–receiver pair through simulation; and Section 3.5 offers concluding remarks.

3.2. MULTICARRIER RADAR

OFDM and OTFS waveforms fall under the umbrella of multicarrier waveforms and can be described by the same model for multicarrier radar waveforms. Such generalization, without including OTFS, is presented in [53]. In Chapter 2, it was argued that both OFDM and OTFS can be represented in the same domains. For a given time-frequency representation of an OFDM or OTFS signal, the baseband equation describing it may be written in the time domain as

$$s(t) = \sum_{n=0}^{N-1} \sum_{m=0}^{M-1} \mathbf{X}_{\mathrm{TF}}[n,m]\, g_{tx}(t - mT)\, e^{j2\pi n \Delta \mathrm{f}(t-mT)} \tag{3.1}$$

where $\mathbf{X}_{\mathrm{TF}} \in \mathrm{C}^{N\times M}$ is the TF representation of the multicarrier signals with N subcarriers and M subpulses. The duration of each subpulse is T, and $\Delta f = 1/T$ is

the intercarrier spacing. The critically sampled discrete equivalent of equation (3.1) can be written in matrix form as

$$\mathbf{s}_{\mathrm{TX}} = \mathrm{vec}(\mathbf{F}_N^H \mathbf{X}_{\mathrm{TF}}) \tag{3.2}$$

where $\mathbf{F}_N^H$ is the IDFT matrix performing the IDFT transform along columns (i.e., the Heisenberg transform) to create the time-signal from the time-frequency grid. Generally, the received signal in the monostatic radar case will be an integration of time and frequency-shifted replicas of the transmitted waveform. For P monostatic propagation paths, it can be written generically as

$$s_{\mathrm{RX}}(t) = \sum_{p=0}^{P-1} a_p \; s\big(k-\tau_p\big) e^{j2\pi f_{D,p}(t-\tau_p)} \tag{3.3}$$

where a_p, τ_p, and $f_{D,p}$ are the complex amplitude, time delay, and frequency shift associated with each path p. While this is correct, in order to understand the effect of the channel on the signal at the symbol level, it is helpful to look at how the time and frequency shifts manifest in the time-frequency discrete representation of the transmitted signal. This can be accomplished by using a slightly altered version of the generalized multicarrier radar signal model presented first in [53]. We define the following notation: for a delay τ_p and a Doppler shift $f_{D,p}$,

$$\psi_p = \exp\big(-j2\pi f_c \tau_p\big), \tag{3.4}$$

represents the phase shift due to the propagation delay of the carrier signal. The Doppler shift is captured through

$$\gamma_p = \exp\left(-j2\pi \frac{T}{N} f_{D,p}\right). \tag{3.5}$$

by constructing the following matrices

$$\mathbf{\Gamma}_1(f_{D,p}) = \mathrm{diag}\{\gamma_p^0, \gamma_p^1, \ldots, \gamma_p^{(N-1)}\} \tag{3.6}$$

$$\mathbf{\Gamma}_2(f_{D,p}) = \mathrm{diag}\{\gamma_p^0, \gamma_p^N, \ldots, \gamma_p^{(M-1)N}\}, \tag{3.7}$$

where $\mathbf{\Gamma}_1 \in \mathbb{C}^{N\times N}$ represents the Doppler-related phase shift along the fast time (the ICI) and $\mathbf{\Gamma}_2 \in \mathbb{C}^{M\times M}$ is the Doppler phase shift across subpulses. Analogously, a matrix form of the target range-related subcarrier phase shift can be constructed through

$$a_p = \exp\big(-j2\pi\Delta f \tau_p\big), \tag{3.8}$$

with the matrix

$$\mathbf{A}(\tau_p) = \mathrm{diag}\{a_p^0, a_p^1, \ldots, a_p^{N-1}\}. \tag{3.9}$$

Lastly, the multicarrier structure of the signal is captured by the IDFT matrix, now scaled by the Doppler shift. If we define

$$\beta_{\mathrm{RX},p} = \exp\left(j2\pi\Delta f \tfrac{T}{N}\left(1-\tfrac{2v_p}{c}\right)\right), \tag{3.10}$$

then, the scaled IDFT matrix is

$$\mathbf{B}_{\mathrm{RX},p} = \begin{bmatrix} 1 & 1 & \cdots & 1 \\ 1 & \beta_{\mathrm{RX},p} & \cdots & \beta_{\mathrm{RX},p}^{(N-1)} \\ \vdots & \vdots & \ddots & \vdots \\ 1 & \beta_{\mathrm{RX},p}^{(N-1)} & \cdots & \beta_{\mathrm{RX},p}^{(N-1)(N-1)} \end{bmatrix} \tag{3.11}$$

and the baseband received multicarrier signal can be written compactly as

$$\mathbf{s}_{\mathrm{RX}} = \sum_p \mathrm{vec}\left(\mu_p \psi_p \mathbf{\Gamma}_1(f_{D,p}) \mathbf{B}_{\mathrm{RX},p} \mathbf{A}(\tau_p) \mathbf{X}_{\mathrm{TF}} \mathbf{\Gamma}_2(f_{D,p})\right), \tag{3.12}$$

where μ_p is the complex amplitude associated to the path p, and $\mathbf{s}_{\mathrm{RX}} \in \mathbb{C}^{MN\times 1}$. The terms $\mathbf{\Gamma}_1(f_{D,p})$, $\mathbf{\Gamma}_2(f_{D,p})$, $\mathbf{B}_{\mathrm{RX},p}$, $\mathbf{A}(\tau_p)$, ψ_p, and μ_p contain the target-dependent information. This model can be used as a common representation for different time-frequency signals, including OFDM and OTFS signals. In OFDM, the communication symbols in the time-frequency plane are the entries $x_{n,m}$ of $\mathbf{X}_{\mathrm{TF}}$, whereas in OTFS, the symbols are defined in the delay-Doppler domain through the matrix $\mathbf{X}_{\mathrm{DD}}$ and transformed to the time-frequency domain via the inverse symplectic finite Fourier transform (ISFFT) (i.e. a DFT over the columns and a IDFT over the rows of X_{DD}),

$$\mathbf{X}_{\mathrm{TF}}^{\mathrm{OTFS}} = \mathbf{F}_N \mathbf{X}_{\mathrm{DD}}^{\mathrm{OTFS}} \mathbf{F}_M^H \tag{3.13}$$

where, by letting $\mathbf{X} = \mathbf{X}_{\mathrm{OTFS}}$ in (3.2) and (3.12), the model can be applied for OTFS modulation. For simplicity, we assume that the cyclic prefix is long enough that no significant ISI is present in the signal.

3.3. MULTICARRIER RADAR RECEIVERS

In this section, we will introduce three different multicarrier radar receivers available in different forms in the literature.

3.3.1. TIME-DOMAIN CORRELATION

A straightforward receiver for multicarrier radar, presented in [47] and used, e.g., in [53, 74], consists of the correlation of the known time-domain signal (3.1) with the expected received signal (3.12) for all the relevant delay-Doppler pairs. Such a receiver is valid for any waveform, and it is the strict definition of the matched filter operation in radar. It can be written as

$$\chi(\tau, f) = \int_{-\infty}^{\infty} s(t)\, s^*(t-\tau)\, e^{i2\pi f_D t}\, dt \tag{3.14}$$

where $s(t)$ is the transmitted signal, $s(t-\tau)$ is its complex conjugate delayed by τ, and the exponential term accounts for the Doppler shift. The matched filter is designed to maximize the SNR for a known transmitted waveform. However, in the context of multicarrier communication waveforms, a matched filter in the

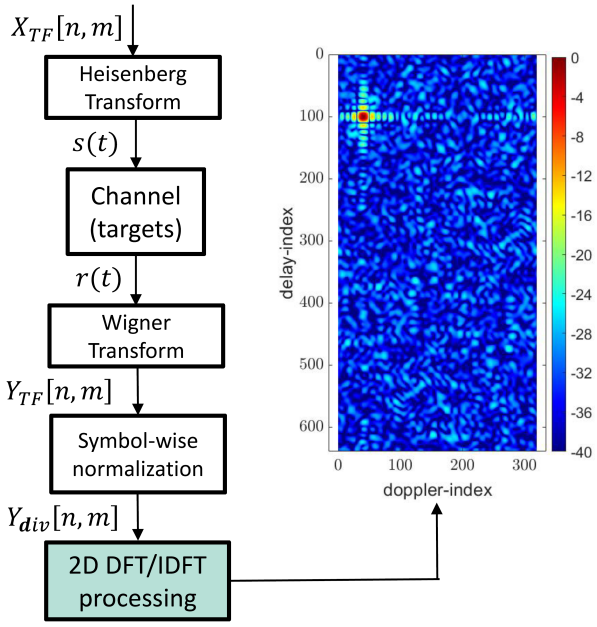

Figure 3.1: Block diagram of the spectral-division based receiver for OFDM, where the signal processing steps for range-Doppler estimation in OFDM radar, and the resulting spectrogram (normalized amplitude, dB), are shown.

time-domain signal can lead to artifacts due to repeating frame structure elements such as the cyclic prefixes. In our implementation, a removal of the cyclic prefixes is performed before the matched filter is applied, effectively overcoming this issue. Another crucial shortcoming is the high computational complexity due to the high number of correlations to compute, which makes this type of receiver impractical in many low-cost civil applications.

3.3.2. SYMBOL-CANCELING RECEIVER

An alternative to such a general receiver is to design a receiver for each specific multicarrier communications waveform using its specific frame structure. We start with the radar receiver generally associated with OFDM radar. The "symbol-canceling" radar receiver for cyclic-prefix OFDM (CP-OFDM), presented first in [75] and widely used in radar literature thereafter (e.g. [19, 76]), accomplishes that by reducing the complexity of the receiver to a 2D DFT, although only under the assumption of no ICI or ISI. This assumption is valid for $f_d \leq 0.1\Delta f$ and

τ lower than the CP duration. The receiver is implemented by performing an element-wise division of the received signal in the time-frequency domain $\mathbf{Y}^{\text{RX}}$ by the time-frequency communication symbols $\mathbf{X}$, that is

$$\mathbf{Y}^{\text{div}}_{n,m} = \frac{\mathbf{Y}^{\text{RX}}_{n,m}}{\mathbf{X}_{n,m}}, \tag{3.15}$$

and then performing an IDFT over the columns and a DFT over the rows,

$$\mathbf{P} = \mathbf{F}_N^H \mathbf{Y}^{\text{div}} \mathbf{F}_M, \tag{3.16}$$

resulting in the spectrum $\mathbf{P}$. A schematic and example of the peridogram output for this receiver is shown in Fig. 3.1. Interestingly, the double DFT in (3.16) is exactly the symplectic finite Fourier transform (SFFT), i.e., the inverse transformation used to generate the OTFS time-frequency signal in (3.13). Therefore, this receiver normalizes the received signal in the time-frequency domain and transforms the result to the delay-Doppler domain, showing a connection between OFDM and OTFS. For example, if the time-frequency shifts $[\tau, f_d] = [0,0]$, $\mathbf{Y}_{\text{div}}$ is an all-ones matrix, and its delay-Doppler representation $\mathbf{Y}^{\text{DD}}_{\text{div}}$ appears as a peak in $[0,0]$. For any other pair of $[\tau_p, \upsilon_p]$, the peak in $\mathbf{Y}^{\text{DD}}_{\text{div}}$ is displaced to the corresponding index in the delay-Doppler plane. Therefore, what this receiver is accomplishing is to normalise the OFDM time-frequency representation into bases in the delay-Doppler domain that represent each delay-Doppler path in the signal (associated with each target, if there is no multipath). Although this receiver is generally associated with CP-OFDM radar, it is possible to adapt it to OTFS with some changes. First, we use a cyclic prefix between the subsymbols in OTFS. This is usually referred to as repeat-cyclic-prefix OTFS (RCP-OTFS) [77]. This addition is required to avoid ISI. Second, we substitute the element-wise division in (3.19) with a phase-normalization given by

$$\mathbf{Y}^{\text{norm,OTFS}}_{n,m} = \mathbf{Y}^{\text{RX,OTFS}}_{n,m} \exp\left(-j\Psi[n,m]\right) \tag{3.17}$$

where

$$\Psi[n,m] = \angle(\mathbf{X}_{\text{OTFS}}[n,m]). \tag{3.18}$$

The purpose of this change is to avoid distorting the amplitude of the received OTFS time-frequency signal, as the reference transmitter OTFS time-frequency signal is not a constant amplitude across subcarriers/subsymbols. Note that this formulation is equivalent to the element-wise division used in the OFDM signal for symbol cancellation. With this slightly altered formulation, we have adapted the low-cost symbol-cancelling receiver to function for OTFS, and we will compare the performance of these receiver-waveform pairs in the following sections.

3.3.3. DELAY-DOPPLER DOMAIN RECEIVER

We move on to a radar receiver commonly associated with OTFS, as it is based on the delay-Doppler representation of the signal. This receiver was proposed first for OTFS in [28], and also rediscovered with slight variations in [29, 51]. In [28], this formulation is compared with the symbol-cancelling receiver paired with an

OFDM waveform. The results are used to argue that OTFS outperforms OFDM in terms of non-ambiguous range and Doppler parameter estimation, as well as ICI/ISI tolerance. However, the formulation is valid for any multicarrier signal and can be readily adapted to OFDM. The approach mirrors the one used to adapt the symbol-cancelling receiver to OTFS in the previous section. We use the delay-Doppler representation of the received and transmitted OFDM signals to formulate a joint delay-Doppler receiver that shares the same qualities for both OTFS and OFDM.

The delay-Doppler domain receiver is built upon the fact that phase shifts in the time-frequency domain correspond to a signal translation in the delay-Doppler domain. With $\mathbf{x}_{\text{DD}} = \text{vec}(\mathbf{X}_{\text{DD}})$, and $\mathbf{y}_{\text{DD}} = \text{vec}(\mathbf{Y}_{\text{DD}})$, then

$$\mathbf{y}_{\text{DD}} = \mathbf{H}\mathbf{x}_{\text{DD}} + \mathbf{w} \tag{3.19}$$

where $\mathbf{w} \in \mathbb{C}^{NM\times 1}$ is additive complex white gaussian noise, and $\mathbf{H} \in \mathbb{C}^{NM\times(NM)^2}$. We define a matrix $\mathbf{H}$ having the first column as equal to $\mathbf{x}_{\text{DD}}$, and the remaining columns are progressively bigger circulant shifts of $\mathbf{x}_{\text{DD}}$ modulated by the ICI phase-terms $\mathbf{\Gamma}_1(f_D)$ associated to each Doppler shift, such that each column of $\mathbf{H}$ corresponds to a n' and m' delay-Doppler shift hypothesis, which can be written compactly as

$$\mathbf{H} = [\mathbf{h}(0,0), \mathbf{h}(1,0), \ldots, \mathbf{h}(0,1), \ldots, \mathbf{h}(N-1, M-1), \ldots, \mathbf{h}\left(N^2-1, M^2-1\right)] \tag{3.20}$$

where the columns $\mathbf{h}_{n',m'}$ are

$$\mathbf{h}(n', m') = \text{vec}\left(\mathbf{\Gamma}_1^{-1}\left(f_D = m'/MT\right)\mathbf{P}_N(n')\mathbf{X}_{\text{DD}}\mathbf{P}_M(m')\right) \tag{3.21}$$

where the matrices $\mathbf{P}_N$ and $\mathbf{P}_M$ are standard circular permutation matrices for the rows (delay) and columns (Doppler) dimensions. Finally, the output of the receiver is given by

$$\hat{\mathbf{h}}_{\text{DD}} = \mathbf{H}^H\mathbf{y}_{\text{DD}} \tag{3.22}$$

where $\hat{\mathbf{h}}_{\text{DD}} \in \mathbb{C}^{(NM)^2\times 1}$ can be reshaped into $\hat{\mathbf{x}}_{\text{DD}} \in \mathbb{C}^{NM\times NM}$, with each element being the receiver output for each delay-Doppler shift pair.

The core idea with this receiver is to solve the matched filter output jointly for the delay and Doppler. Intuitively, the inter-symbol Doppler dependent phase shift $\mathbf{\Gamma}_2$ causes the circular shift of the received signal in the Doppler dimension, and the delay-dependent phase shift across subcarriers modelled by $\mathbf{A}$ causes the circulant shift in the transmitted signal in the delay dimension, following the properties of the Fourier Transform. However, the Doppler-dependent phase shift along subcarriers (the ICI) occurs on top of and is compensated for by the term $\mathbf{\Gamma}_1^{-1}$. This is only possible because of the joint estimation of the delay and Doppler, which increases the computational complexity and memory requirements of such a receiver. An analogous compensation of the ISI, a delay-dependent phase shift that modulates each subsymbol, is also possible and introduced in the later simulations within this chapter. An OTFS radar parameter estimation technique based on the generalized likelihood ratio test (GLRT) with similar properties has been reported in [29].

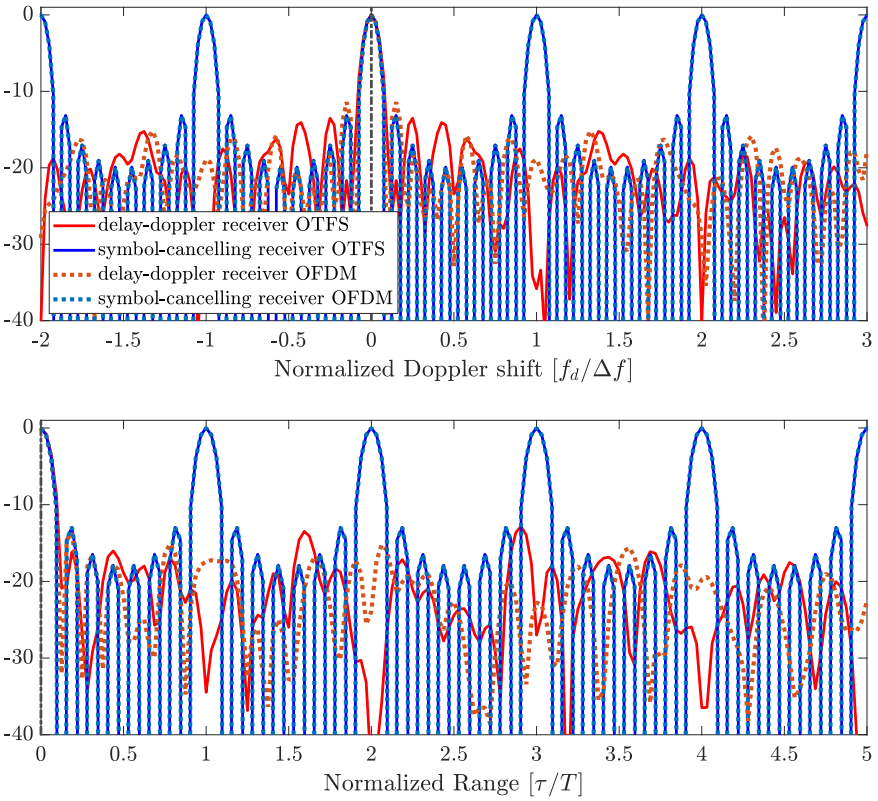

Figure 3.2: Receiver output of all the presented waveform-receiver pairs for zero delay and doppler shifts, showing the receiver output without any signal distortion. The symbol-cancelling receiver output overlaps for OTFS and OFDM, whereas de delay-doppler receiver output does not. $N = 8$ and $M = 10$.

3.4. SIMULATIONS RESULTS

In this section, we show the simulations of the presented radar receivers for both OFDM and OTFS signals to investigate the relationship between receiver and waveform performance. For this purpose, we simulate i) a scenario with no doppler or delay shifts, to compare the characteristics of the receivers without any ICI/ISI effect from the channel; ii) a scenario with $f_d \leq 0.1\Delta f$, in which the effect of ICI is tolerable for all receivers; and iii) a scenario with $f_d > \Delta f$, where the effect of ICI is substantial, and compensation or joint range-Doppler estimation is necessary. Lastly, we evaluate the integrated side lobe ratio (ISLR) [78]to understand the differences between waveforms and receivers further. The ISLR describes the ratio of power between the sidelobes and the mainlobe. A higher value indicates more power in the sidelobes with respect to the mainlobe. It can be written for a general correlation,

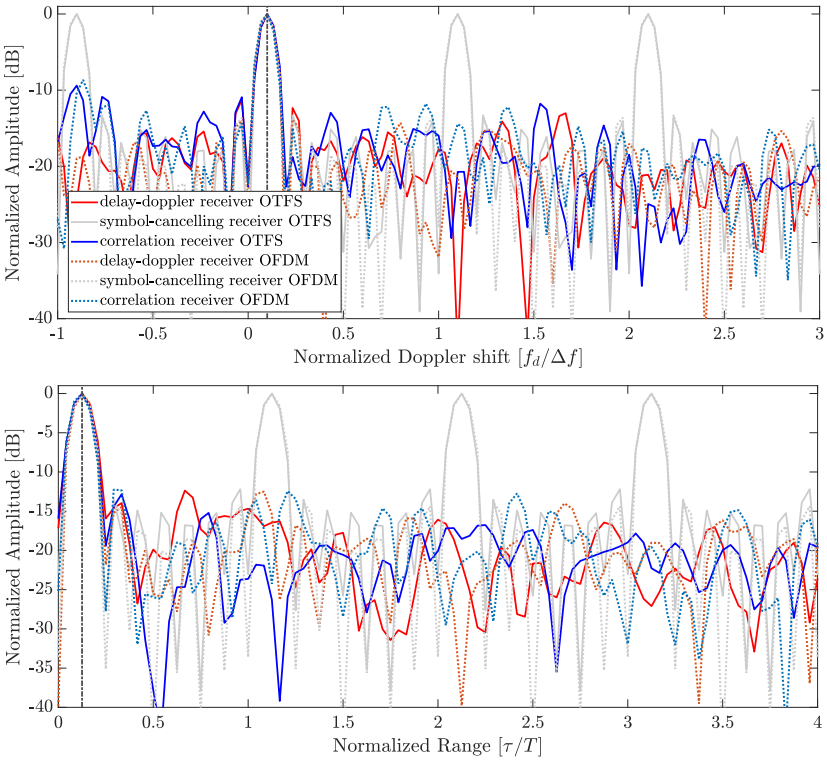

Figure 3.3: Receiver output of all the presented waveform-receiver pairs for low time and Doppler shifts. The delay-Doppler receiver and the simple time-domain matched-filter show an increased unambiguous estimation range in both delay and Doppler, whereas the symbol-cancelling receiver has a smaller unambiguous region as it ignores the effect of ICI and ISI. When compared to Fig. 3.2, moderate ICI adds a noise-like distortion to the sidelobes in the symbol-canceling receiver. $N = 8$ and $M = 10$.

e.g., in time as

$$\text{ISLR} = 10\log_{10}\left(\frac{\int_{|\tau|>T_0} |\chi(\tau)|^2\, d\tau}{\int_{|\tau|\leq T_0} |\chi(\tau)|^2\, d\tau}\right) \tag{3.23}$$

where T_0 indicates the limits of the mainlobe in the correlation or estimation, and $\chi(\tau)$ represents a generic autocorrelation of a signal for different values of τ.

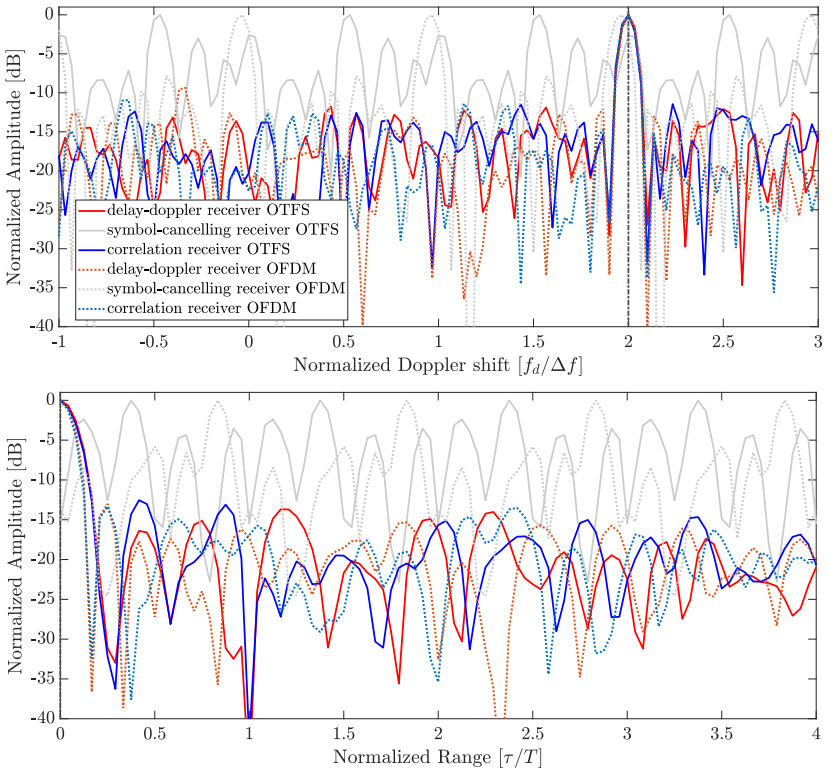

Figure 3.4: Receiver output of all the presented waveform-receiver pairs for a big Doppler shift, causing strong ICI. ICI visibly degrades symbol-canceling receiver performance. $N = 8$ and $M = 10$.

3.4.1. QUALITATIVE WAVEFORM-RECEIVER COMPARISON

First, we explore the scenario in which no delay and Doppler shift is present on the received signal. This is clearly not a realistic scenario for radar, but it aids in understanding the characteristics of each waveform-receiver pair. The range and Doppler estimation outputs are plotted in Fig. 3.2, showing that the symbol cancelling receiver in the TF domain performs exactly the same in OFDM and OTFS, assuming the RCP-OTFS variant with cyclic prefixes before each subsymbol, and indicating that the TF representation does not affect the estimation when no ICI-ISI is present. On the other hand, we can see slight differences in the sidelobes when comparing OFDM and OTFS paired with the joint delay-Doppler receiver, indicating that the different representation of the information signal affects the performance of this receiver. Moreover, it is also shown that the delay-Dopplr receiver shows no grating lobes in the multiples of T and Δf, indicating a higher non-unambiguous parameter estimation region, which theoretically can extend until $N\Delta f$ and MT for

Doppler and delay respectively.

Next, we consider scenarios in which the Doppler shift is small enough that ICI is not a substantial issue (i.e., $f_d = 0.1\Delta f$). Fig. 3.3 shows the delay and Doppler receiver outputs in such a scenario. Under these conditions, it can be seen that all receivers peak at the correct range and Doppler hypotheses for both OFDM and OTFS waveforms. Reduction of the unambiguous range and Doppler in the symbol-canceling receiver can also be noticed, with the grating lobes appearing on delays $\tau' = (nT + \tau)$ and Doppler shifts $f'_d = (m\Delta f + f_d)$. Again, the Delay-Doppler and time-domain correlation receivers are capable of unambiguous estimation up to $N\Delta f$ and MT for Doppler shifts and delay, respectively. Moreover, the mainlobe does not significantly differ between receivers or waveforms. At low Doppler, the symbol canceling receiver output resembles a *sinc* function, enabling sidelobe reduction through windowing at the cost of increasing the mainlobe width. The benefits of windowing will decrease as the Doppler increases.

Finally, we consider a high ICI scenario in which $f_d = 2\Delta f$, and compute the output of the presented receivers for both OTFS and OFDM signals. The output (see Fig. 3.4) shows little difference between the OTFS and OFDM in each receiver type.

The symbol-canceling receiver cannot resolve the target unambiguously in either the delay or the Doppler domain. This is expected, as not only is the target beyond the unambiguous hypotheses in terms of Doppler, but also the implicit assumption of no ICI in the receiver is strongly violated. Both the time-domain correlation and delay-Doppler domain receivers' output reflect the correct target parameters, showing that they are not affected by ICI and that their unambiguous range and Doppler extend to the bandwidth and duration of the signal.

3.4.2. INTEGRATED SIDE-LOBE RATIO EVALUATION

Lastly, we evaluate the side-lobe characteristics of the presented receiver-waveform combinations for the delay and Doppler estimation. As the main-lobe characteristics are identical for all receivers (in low ICI cases for the symbol-canceling receiver), we choose the ISLR as a metric to compare each waveform-receiver combination. We evaluate the metric within the $\tau' = [0, T]$ and $f'_d = [0, \Delta f]$ as the symbol-canceling receiver output is unusable beyond that Doppler shift. The side-lobe characteristics of the delay-Doppler and time-domain correlation receivers remain constant for higher values of τ and f_d. Simulations are conducted under noiseless conditions in order to evaluate solely the sidelobe power.

The results (see Fig. 3.5 and Fig. 3.6) show differences in the ISLR both between receivers and waveforms. Most notably, the degradation of the ISLR for the symbol-canceling receiver increases as the Doppler shifts approach Δf, and the unaccounted effect of the ICI degrades the output of the receiver. Notably, this degradation occurs both in the delay and Doppler estimation. The small ripples in the delay-Doppler receiver are caused by the off-grid error in the estimation process being unaccounted for. Overall, the delay-Doppler and correlation receivers show similar performance (with a notable exception for OTFS in the range estimation), and OFDM shows a lower ISLR level in Doppler estimation. In contrast, OTFS shows a lower ISLR in range estimation with the time-correlation receiver.

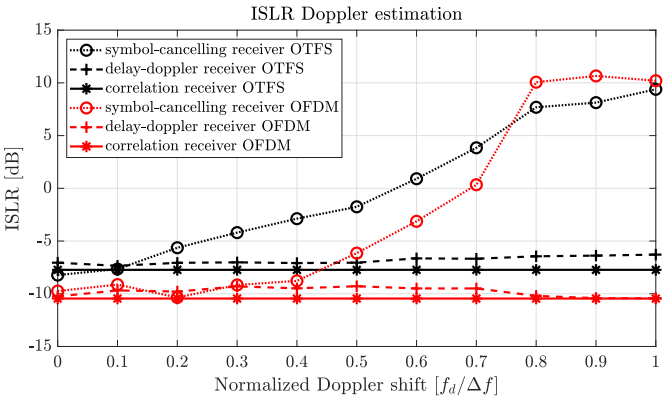

Figure 3.5: Integrated side-lobe ratio in the Doppler estimation for $f_d \leq \Delta f$. $N = 8$ and $M = 10$.

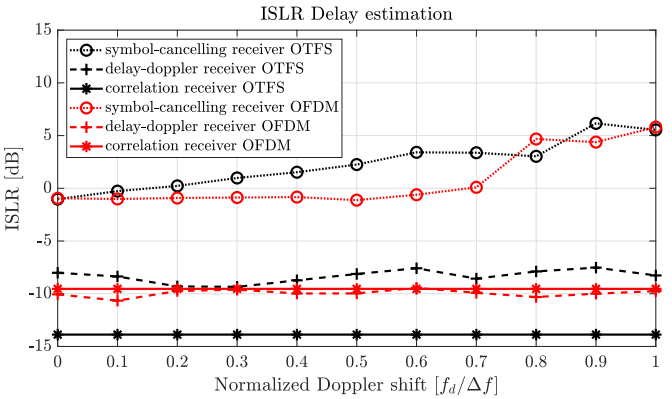

Figure 3.6: Integrated side-lobe ratio in the delay estimation for $f_d \leq \Delta f$. $N = 8$ and $M = 10$.

3.5. CONCLUSIONS

This chapter delivers the first waveform-agnostic framework for evaluating OTFS and OFDM radar receivers, enabling a genuinely fair comparison between the two multicarrier families. The results reveal that, for radar operation, OTFS is not more Doppler tolerant than OFDM when paired with the same symbol-canceling receiver. A joint delay-Doppler receiver, usually associated with OTFS, can achieve Doppler tolerance at the cost of higher computational complexity for both OTFS and OFDM. Therefore, we conclude that receiver design can be generalized for any multicarrier waveform and that radar sensing properties usually attributed to OTFS and OFDM are, in fact, primarily due to the difference in the receivers traditionally associated with each waveform. Nonetheless, we demonstrated differences between OFDM and OTFS waveforms regarding the side-lobe characteristics for different receiver outputs.

Although the radar properties of OTFS and OFDM under the presented receivers are similar, OTFS offers the possibility of designing a signal in the delay-Doppler domain, opening exciting opportunities in signal orthogonality for MIMO and new interference interactions investigated in subsequent chapters.

4

NU-OTFS: MIMO OTFS WITH ARBITRARY TIME-FREQUENCY ALLOCATION

"To remain in the past means to be dead."
— José Ortega y Gasset

This chapter proposes a novel waveform, namely non-uniform OTFS (NU-OTFS), for joint radar and communication applications (Radcom) in multi-user/MIMO scenarios. Based on orthogonal time frequency space (OTFS) modulation, the proposed waveform is realized by using a non-uniform symplectic finite Fourier transform (NU-SFFT) to generate non-overlapping quasi-arbitrary time-frequency representations of OTFS messages. Non-uniform sampling and sparse reconstruction algorithms within the compressed sensing framework are employed to avoid (self-)interference and enhance radar target parameter estimation. The performance of NU-OTFS and its corresponding receivers is evaluated through numerical simulations and measurements, and compared with state-of-the-art MU/MIMO Radcom OTFS system concepts. NU-OTFS allows for increased flexibility in time-frequency resource allocation and larger unambiguous radar parameter estimation while showing comparable performance to state-of-the-art OTFS multi-user communication implementations in realistic high-mobility channel conditions.

Parts of this chapter have been published in [70].

4.1. INTRODUCTION

Besides range and velocity estimation explored in the previous chapter, estimating the angular position of reflecting targets through array processing is crucial in many radar applications, such as automotive radar [6]. MIMO radar effectively increases the angular resolution with fewer array elements by exploiting path diversity between different transmit-receive pairs [79]. MIMO radar relies on the separability of the signals emitted by each transmitter to increase angular resolution [63]. In communications, signal separability from different transmitters is also required to enable simultaneous access for multiple users sharing the same bandwidth [64]. Therefore the ability to multiplex different radar transmitters or communication users such that they are separable in a receiver is desirable for both radar and communication applications. In OFDM, this can be accomplished by multiplexing the different transmitters directly in the time-frequency (TF) domain, allocating non-overlapping TF bins to different transmitters [64]. Under realistic channel conditions, the signal associated with different transmitters/users can be recovered by filtering the appropriate TF resource blocks in the receiver [65].

For OTFS, multiplexing directly on the DD domain is also not trivial, as time-frequency shifts in the channel result in a quasi-periodic 2D rotation of the symbols in this domain [80], and separating the transmitters without prior knowledge of the channel can be difficult. It is possible to exploit channel characteristics, such as diversity in user mobility, to minimize inter-user interference [81], achieving improved performance for user multiplexing but not allowing for transmitter multiplexing in MIMO radar without channel knowledge. Specific DD resource allocations that allow for separability in the time-frequency domain have been studied in [36, 66] for multiple user access for OTFS communications. The resulting TF representation amounts to interleaving or block allocation of transmitters/users in the TF resource plane. Such allocation is problematic for radar applications, as it reduces the non-ambiguous interval or resolution in either range or Doppler domain [33]. Alternative TF allocation schemes, particularly non-uniform optimized [34] or random patterns [33], have shown great promise in OFDM radar applications when paired with sparse reconstruction algorithms. Sparse reconstruction algorithms have shown potential in various aspects of radar signal processing [67] and interference mitigation [68] due to the inherent sparsity of radar data in the delay-Doppler-angle domain.

In this chapter, a novel waveform that maps an OTFS frame into quasi-arbitrary TF patterns is proposed, increasing the multiplexing flexibility of OTFS in both MIMO radar and MU communications. The proposed waveform is referred to as non-uniform OTFS (NU-OTFS). Specifically, the main contributions of this chapter are the following.

1. A generalized formulation for time-frequency multiplexing of OTFS signals, resulting in the NU-OTFS waveform. A non-uniform ISFFT (NU-ISFFT) is defined using non-uniform discrete Fourier operators for its implementation. The NU-ISFFT is used to generate non-overlapping TF representations of the OTFS messages and recover the OTFS message from a partially sampled TF plane. This non-overlapping representation enables transmitter/user separation

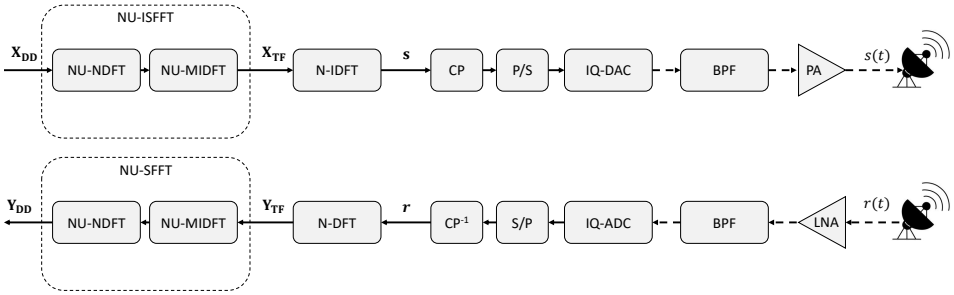

Figure 4.1: Block diagram of a single channel NU-OTFS for MU/MIMO showing the non-uniform (NU) ISFFT operators. In transmission, the NU-ISFFT is implemented using a non-uniform DFT along the N dimension (NU-NDFT) and an inverse NU-DFT along the M dimension (NU-MIDFT). An IDFT along the N dimension (N-IDFT) is used to transform the time-frequency signal into a time-domain signal. Transmission occurs after cyclic-prefix appending (CP), digital-to-analog conversion (DAC), band-pass filtering (BPF), and amplification (PA). The inverse operations are carried out in the receiver chain, before the radar/communication receiver is implemented.

at the receiver by filtering out the unwanted time-frequency samples in the digital domain. The inverse transform (NU-SFFT) is then used to move back to the original DD representation from the sparsely sampled TF signal. This formulation is general and can be used to include fixed patterns presented in previous work, such as interleaved TF allocation [66], as well as other quasi-arbitrary non-uniform patterns. Non-uniform time-frequency multiplexing is novel in OTFS waveforms. NU-OTFS could also simplify the implementation of high-bandwidth multistatic radar networks with reduced interference due to the increased flexibility in TF resource allocation. A schematic depiction of the proposed scheme for transmission and reception is shown in Fig. 4.1.

2. A simulation and measurement-based evaluation of the performance of the proposed NU-OTFS waveform for monostatic MIMO radar applications. This is the first measurement-based OTFS radar validation reported in the literature, to the best of the author's knowledge. A signal processing chain based on compressed sensing (CS) is proposed, compared to traditional OTFS implementations, and validated through measurements.

3. A simulation-based study of the communications performance of NU-OTFS compared to other OTFS approaches, using standard 3GPP vehicular channel models [82] for simulation. A numerical comparison of error rates for different SNR and channel mobility values is drawn.

The remainder of the chapter is structured as follows. Section 4.2 presents a

mathematical description of OTFS signal generation and channel effects and presents a novel system concept based on the NU-SFFT to generate the proposed NU-OTFS waveform. Section 4.3 includes descriptions of NU-OTFS radar and communication receivers. Section 4.4 presents numerical radar and communications performance simulations for the proposed NU-OTFS system concept, as well as experimental validation for NU-OTFS radar. Finally, a chapter summary is given in section 4.5.

4.2. OTFS SIGNAL MODEL

Consider a single transmitter OTFS system transmitting a message $\mathbf{X}_{\mathrm{DD}} \in \mathbb{C}^{N\times M}$ defined in a $N \times M$ delay-Doppler grid, with N delay bins and M Doppler bins. The number of subcarriers and subsymbols in TF representation is N and M, respectively. The communication symbols are mapped to the time-frequency domain through the inverse symplectic Fourier transform (ISFFT) such that

$$\mathbf{X}_{\mathrm{TF}}[n,m] = \frac{1}{\sqrt{NM}} \sum_{k=0}^{N-1} \sum_{l=0}^{M-1} \mathbf{X}_{\mathrm{DD}}[k,l] e^{j2\pi\left(\frac{ml}{M} - \frac{nk}{N}\right)} \tag{4.1}$$

where $[k,l]$ are index pairs in the delay-Doppler grid, and $[n,m]$ are index pairs in the time-frequency grid. $\mathbf{X}_{\mathrm{TF}}[n,m]$ is the time-frequency representation of the OTFS symbols, now spread in the time-frequency domain. The TF signal is converted into the time domain for transmission using the Heisenberg transform. The time domain signal $s(t)$ is given by

$$s(t) = \sum_{n=0}^{N-1} \sum_{m=0}^{M-1} \mathbf{X}_{\mathrm{TF}}[n,m] g_{tx}(t-nT) e^{j2\pi n\Delta \mathrm{f}(t-mT)} \tag{4.2}$$

where g_{tx} is the transmit pulse. Assuming a rectangular transmit pulse and a critically sampled signal, equations (4.1) and (4.2) can be written in compact matrix notation as

$$\mathbf{X}_{\mathrm{TF}} = \mathbf{F}_{\mathrm{N}} \mathbf{X}_{\mathrm{DD}} \mathbf{F}_{\mathrm{M}}^{\mathrm{H}} \tag{4.3}$$

and

$$\mathbf{s} = \mathrm{vec}\left(\mathbf{F}_{\mathrm{N}}^{\mathrm{H}} \mathbf{X}_{\mathrm{TF}}\right) = \mathrm{vec}\left(\mathbf{X}_{\mathrm{DD}} \mathbf{F}_{\mathrm{M}}^{\mathrm{H}}\right) \tag{4.4}$$

where $\mathbf{F}_{\mathrm{N}} \in \mathbb{C}^{N\times N}$ and $\mathbf{F}_{\mathrm{M}} \in \mathbb{C}^{M\times M}$ are normalized Fourier transform matrices. The discrete time-domain signal $\mathbf{s} \in \mathbb{C}^{NM\times 1}$ is transformed to the analog domain with a digital-to-analog converter (DAC) before undergoing I/Q modulation to the desired carrier frequency f_c. For this chapter, narrowband radar operation is assumed in all steps, and therefore, $f_c \gg B$, where $B = N\Delta \mathrm{f}$ is the bandwidth of the OTFS signal. In both communication and radar applications, the received signal is a linear combination of multiple time and frequency-shifted replicas of the transmitted signal embedded in noise. For the full parametrization of the monostatic radar channel effects in the multicarrier signal structure, we refer the reader to Chapter 3.

Equations (4.1), and (4.4) describe the generation of the transmitted time-domain signal in a single-transmitter OTFS system, where the entirety of the available time-frequency resources are used by a single radar transmitter or communications user. In this chapter, RCP-OTFS is implemented in order to simplify radar processing.

4.2.1. NU-OTFS TRANSMITTER MULTIPLEXING

For an extension to MU/MIMO case, the signals originating from different users/transmitters must be separable at the receiver. Let us consider the critically sampled received signal as presented in the previous chapters. The time-frequency representation of the received signal is given by

$$\mathbf{Y}_{\mathrm{TF}} = \mathbf{F}_{\mathrm{N}} \mathrm{vec}^{-1}_{N\times M}(\mathbf{r}) \tag{4.5}$$

and the delay-Doppler received signal is given by

$$\mathbf{Y}_{\mathrm{DD}} = \mathbf{F}_{\mathrm{N}}^{\mathrm{H}} \mathbf{Y}_{\mathrm{TF}} \mathbf{F}_{\mathrm{M}} \tag{4.6}$$

which can also be written in the discrete delay-Doppler domain as [80]

$$y_{\mathrm{DD}}[k',l'] = \sum_{k'=0}^{N-1}\sum_{l'=0}^{M-1} h[k',l'] \exp\left(j\frac{2\pi}{NM}[l-l']_M[k']_N\right) \alpha[k,l]x[[k-k']_N,[l-l']_M] \tag{4.7}$$

where

$$\alpha[k,l] = \begin{cases} 1 & \text{if } l' \le l < M \\ \exp\left(-j2\pi\frac{k}{N}\right) & \text{if } 0 \le l < l' \end{cases} \tag{4.8}$$

where $[\cdot]_N$ and $[\cdot]_M$ denote modulo N and M operations respectively. This notation highlights the effect of targets with amplitude $h[k',l']$, delay k', and Doppler shift l' on the received signal, which appear as circular shifts of the transmitted symbols in the delay-Doppler domain. Due to this shift in the delay-Doppler representation, different communication users or radar transmitters can not be separated easily in the delay-Doppler domain without prior channel knowledge. Alternatively, the signal associated with different transmitters can be identified if non-overlapping sets of time-frequency bins are assigned to each of them, as shown, e.g., in Fig. 4.2b. This approach is common in MU/MIMO OFDM applications [64].

In OTFS, the DD symbols are spread in the TF domain after the ISFFT in (4.1) and (4.3); therefore, non-overlapping DD signals can overlap in the TF domain. Some specific arrangements of DD symbols studied in the literature, such as block division or interleaving in the DD domain, result in an interleaving or block division, respectively, in the time-frequency domain [66]. These arrangements are specific forms of the common time-division (symbol) or frequency-division (subcarrier) multiplexing in MU/MIMO OFDM. Fig. 4.2a shows a delay-Doppler multiplexing of two transmitters that, when represented in the time-frequency domain through the standard ISFFT, correspond to subcarrier interleaving (see Fig. 4.2b). This can be extended to 2D interleaved multiplexing, as seen in Figs. 4.2d and 4.2e. However, interleaved frequency and time multiplexing reduce the non-ambiguous range and Doppler, respectively, as depicted in Fig. 4.3. To maintain the total range-Doppler unambiguous interval and transmitter separability in the TF domain, random TF multiplexing is a common approach for OFDM radar. To accomplish quasi-arbitrary

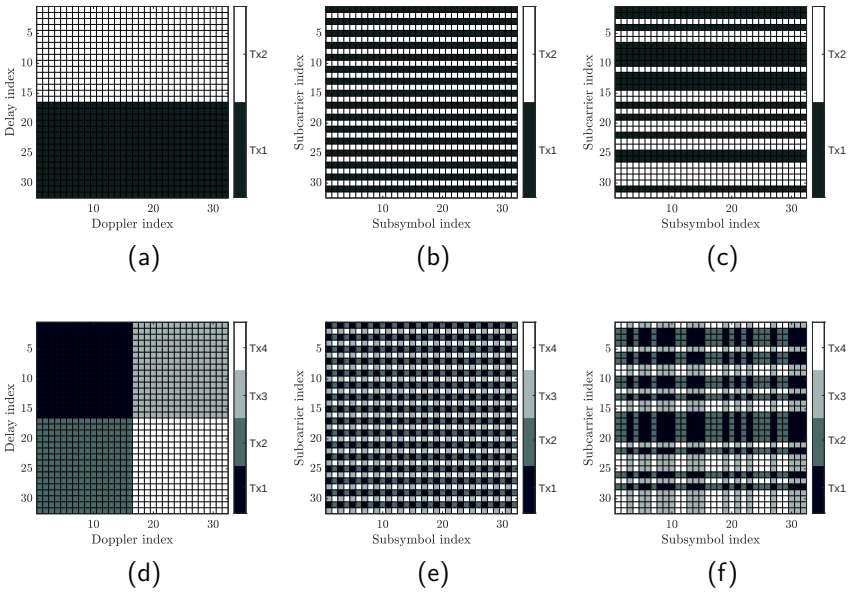

Figure 4.2: Depiction of multiplexing strategy in delay-Doppler representation, standard interleaved multiplexing in time-frequency, and quasi-arbitrary multiplexing in time-frequency with NU-OTFS. (a) delay-Doppler representation of two multiplexed waveforms; (b) interleaved multiplexing in the TF domain; (c) arbitrary multiplexing across subcarriers in the TF domain with NU-OTFS. For 2D quasi-arbitrary multiplexing: (d) four transmitters multiplexed in the delay-Doppler domain; (e) interleaved 2D multiplexing in the time-frequency domain; (f) quasi-arbitrary 2D multiplexing in the TF domain with NU-OTFS.

time-frequency multiplexing for OTFS signals, a non-uniform ISFFT (NU-ISFFT) can be defined by using non-uniform discrete Fourier transform (DFT) operators.

First, let $\mathbf{X}_{\mathrm{DD}}^{\mathrm{MIMO}}$ be defined as

$$\mathbf{X}_{\mathrm{DD}}^{\mathrm{MIMO}} = \begin{bmatrix} \mathbf{X}_{\mathrm{DD}}^{(1,1)} & \cdots & \mathbf{X}_{\mathrm{DD}}^{(1,\sqrt{N_{\mathrm{Tx}}})} \\ \vdots & \ddots & \vdots \\ \mathbf{X}_{\mathrm{DD}}^{(\sqrt{N_{\mathrm{Tx}}},1)} & \cdots & \mathbf{X}_{\mathrm{DD}}^{(\sqrt{N_{\mathrm{Tx}}},\sqrt{N_{\mathrm{Tx}}})} \end{bmatrix} \tag{4.9}$$

where $\mathbf{X}_{\mathrm{DD}}^{(p,q)} \in \mathbb{C}^{(N/\sqrt{N_{\mathrm{Tx}}})\times(M/\sqrt{N_{\mathrm{Tx}}})}$ are the delay-Doppler messages associated to different transmitters, and $\mathbf{X}_{\mathrm{DD}}^{\mathrm{MIMO}} \in \mathbb{C}^{N\times M}$ is the OTFS MIMO frame for a monostatic OTFS radar with N_{Tx} transmitters. For simplicity of notation, it is assumed that N_{Tx} is a square number to assume equal distribution of the messages in the delay and Doppler domain. This is not a necessary condition, as any non-prime number of transmitters can be distributed in tiles across the delay-Doppler domain, or some

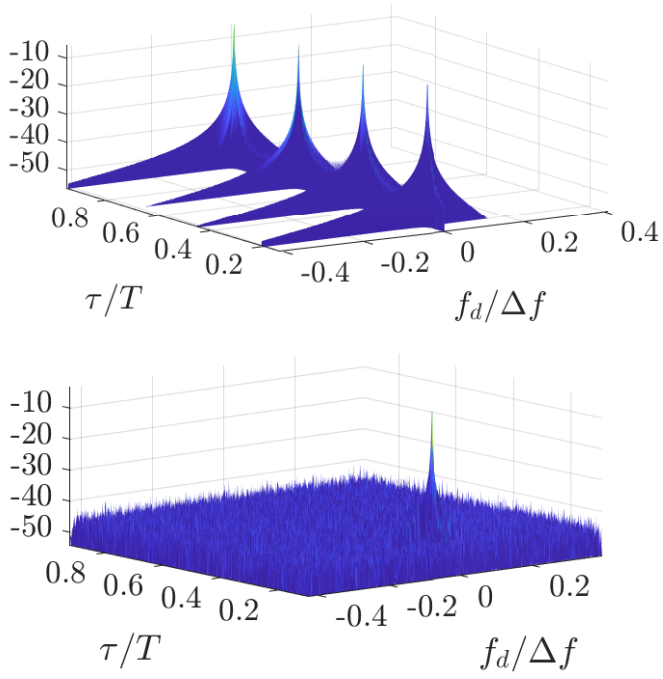

Figure 4.3: Comparison of noiseless range-Doppler estimation with different MIMO approaches with four transmitters. On the top, subcarrier interleaving causes a reduction in the maximum unambiguous range. On the bottom, random multiplexing reduces the dynamic range of the estimation.

time-frequency resources can be left unoccupied. Equation (4.3) can be altered to design a mapping between $\mathbf{X}_{\mathrm{DD}}$ and a TF representation with a quasi-arbitrary TF occupancy pattern. This mapping is denoted here as the NU-ISFFT. For transmitter n_{Tx}, let $\boldsymbol{\xi}_{N,n_{\mathrm{Tx}}} \in \{0,1\}^{N\times 1}$ be a vector indexing the active subcarriers, $\boldsymbol{\xi}_{M,n_{\mathrm{Tx}}} \in \{0,1\}^{M\times 1}$ a vector indexing the active time subsymbols, $\Xi_N^{(n_{\mathrm{Tx}})} = \mathrm{diag}\{\boldsymbol{\xi}_{N,n_{\mathrm{Tx}}}\}$, and $\Xi_M^{(n_{\mathrm{Tx}})} = \mathrm{diag}\{\boldsymbol{\xi}_{M,n_{\mathrm{Tx}}}\}$, then

$$\mathbf{X}_{\mathrm{TF}}^{(n_{\mathrm{Tx}})} = \Xi_N^{(n_{\mathrm{Tx}})} \mathbf{F}_N \mathbf{X}_{\mathrm{DD}}^{(n_{\mathrm{Tx}})} \mathbf{F}_M^{\mathrm{H}} \Xi_M^{(n_{\mathrm{Tx}})} \tag{4.10}$$

$$\mathbf{X}_{\mathrm{TF}}^{\mathrm{MIMO}} = \sum_{n_{tx}=1}^{N_{\mathrm{Tx}}} \mathbf{X}_{\mathrm{TF}}^{(n_{\mathrm{Tx}})} \tag{4.11}$$

where $\mathbf{X}_{\mathrm{TF}}^{(n_{\mathrm{Tx}})} \in \mathbb{C}^{N\times M}$ is the sparse time-frequency representation of the signal associated to the n_{Tx}-th transmitter, and $\mathbf{X}_{\mathrm{TF}}^{\mathrm{MIMO}} \in \mathbb{C}^{N\times M}$ is the time-frequency representation of all the transmitters. In order to achieve arbitrary non-overlapping

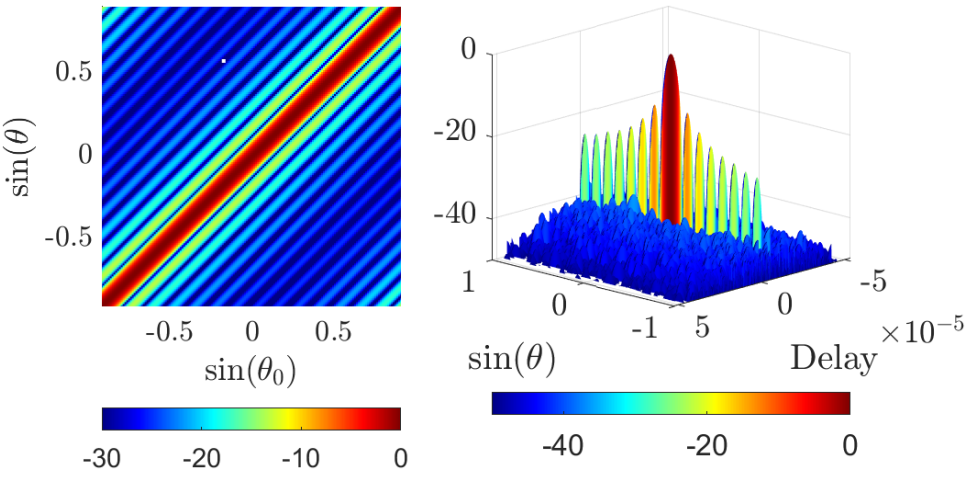

Figure 4.4: MIMO radar ambiguity function (AF) for NU-OTFS, with 16 transmitters and $N = 1024$, $M = 512$. On the left, the angular AF shows that the angular spectrum (distretized in angular hypotheses θ is constant regardless of the target's angular position θ_0. On the right, the range-angle AF shows no artifacts or ambiguities in the delay estimation for the entire signal length.

time representations, it is necessary that

$$\left(\boldsymbol{\xi}_{N,n_{\mathrm{Tx}}}\boldsymbol{\xi}^{T}_{M,n_{\mathrm{Tx}}}\right)\odot\left(\boldsymbol{\xi}_{N,n'_{\mathrm{Tx}}}\boldsymbol{\xi}^{T}_{M,n'_{\mathrm{Tx}}}\right)=\mathbf{0}\quad\forall\quad n_{\mathrm{Tx}}\neq n'_{\mathrm{Tx}} \tag{4.12}$$

where $\mathbf{0}$ is the $N\times M$ all zero matrix. Equation (4.12) forces that no pair of subcarrier-subsymbol is occupied by more than one transmitter. Uniform sampling is performed in the subsymbol dimension if $\Xi_M = \mathbf{I}$, and in the subcarrier if $\Xi_N = \mathbf{I}$. The TF patterns arising from the NU-ISFFT are not truly arbitrary, but rather the intersections of two one-dimensional arbitrary assignations of time and subcarrier resources defined by $\boldsymbol{\xi}_{M,n_{\mathrm{Tx}}}$ and $\boldsymbol{\xi}_{N,n_{\mathrm{Tx}}}$ respectively. The proposed multiplexing is depicted in Fig. 4.2c for multiplexing across the delay/frequency domain and Fig. 4.2f for multiplexing across both the delay/frequency and Doppler/time domain.

Finally, the transmitted time-domain signal is obtained by applying the standard Heisenberg transform to the new TF signal representation, substituting (4.11) in (4.4),

$$\mathbf{s}^{\mathrm{MIMO}}=\mathrm{vec}\left(\mathbf{F}_{\mathrm{N}}^{\mathrm{H}}\mathbf{X}_{\mathrm{TF}}^{\mathrm{MIMO}}\right) \tag{4.13}$$

The MIMO transmit ambiguity function (AF) (as defined in e.g., [60]) of the signal in (4.13) is shown in Fig. 4.4. The MIMO AF shows constant amplitude regardless of target position and no ambiguities or abnormal sidelobes in the range-angular cut, showing no angle-dependent interference between transmitters.

4.3. NU-OTFS RECEIVER

4.3.1. NU-OTFS MIMO RADAR RECEIVER

Consider a critically sampled received echo from a point target at relative azimuth angle ϕ, in an NU-OTFS MIMO system with N_{Tx} transmitters and N_{Rx} receivers arranged in a one-dimensional array, with their positions given by $\mathbf{d}_{\text{Tx}} \in \mathbb{R}^{N_{\text{Tx}}\times 1}$ and $\mathbf{d}_{\text{Rx}} \in \mathbb{R}^{N_{\text{Rx}}\times 1}$ respectively. The steering vector

$$\mathbf{a}(\phi) := \exp\left(j\frac{2\pi}{\lambda}\mathbf{d}_{\text{Tx}}\sin(\phi)\right) \tag{4.14}$$

with $\mathbf{a}(\phi) \in \mathbb{C}^{N_{\text{Tx}}\times 1}$ captures the direction-of-arrival dependent phase shift associated to the position of the transmitters. Analogously, the angle-dependent phase shift at each receiver is given by

$$\mathbf{b}(\phi) := \exp\left(j\frac{2\pi}{\lambda}\mathbf{d}_{Rx}\sin(\phi)\right). \tag{4.15}$$

with $\mathbf{b}(\phi) \in \mathbb{C}^{N_{\text{Rx}}\times 1}$. Then the received signal at receiver n_{Rx} can be written as

$$\mathbf{r}^{\text{MIMO}}_{n_{\text{Rx}}} = \mu\psi b_{n_{\text{Rx}}}(\phi)\sum_{n_{\text{Tx}}=1}^{N_{\text{Tx}}} a_{n_{\text{Tx}}}(\phi)\text{vec}\left(\mathbf{\Gamma_1}\mathbf{F}_{\text{N}}^{\mathbf{H}}\mathbf{A}\mathbf{X}^{\text{MIMO}}_{\text{TF}}\mathbf{\Gamma_2}\right) \tag{4.16}$$

where n_{Tx} and n_{Rx} denote the transmitter and receiver index respectively, and $a_{n_{\text{Tx}}}$ and $b_{n_{\text{Rx}}}$ denote the steering vector entry associated with this index. Co-located MIMO and far-field targets are assumed, and therefore the delay and Doppler shifts associated to each transmit-receive pair are considered the same.

Similarly to (4.5), the TF representation of the signal at receiver n_{Rx} is given by

$$\mathbf{Y}^{\text{MIMO}}_{\text{TF},n_{\text{Rx}}} = \mathbf{F}_{\text{N}}\text{vec}^{-1}_{N\times M}(\mathbf{r}^{\text{MIMO}}_{n_{\text{Rx}}}) \tag{4.17}$$

Henceforth, a single receiver is assumed and the n_{Rx} suffix is omitted to simplify notation. This can be done without loss of generality, as the process of receiving and separating the different transmit signals is invariant to the number of receivers. Each transmitted signal can now be separated in the receiver by

$$\mathbf{Y}^{(n_{\text{Tx}})}_{\text{TF}} = \mathbf{\Xi}^{(n_{\text{Tx}})}_{N}\mathbf{Y}^{\text{MIMO}}_{\text{TF}}\mathbf{\Xi}^{(n_{\text{Tx}})}_{M} \tag{4.18}$$

thus retrieving the signal associated to the n_{Tx} transmitter, and completing the MIMO implementation of NU-OTFS. Further steps involve the range-Doppler estimation in each transmit-receive pair.

Regarding OTFS radar receivers, multiple options have been proposed in the literature. A matched filter in the delay-Doppler domain is described in [28, 29], which accomplishes high Doppler tolerance. However, it involves joint estimation of range and Doppler, making its computational complexity prohibitive for typical radar applications. Therefore, a radar receiver based on a spectral division in the time-frequency domain [72] is chosen as an alternative. Although the chosen receiver degrades for high Doppler shifts, its computation involves only DFT processing to

effectively transform the spectral-normalized TF representation of the received signal into the estimation domain. The implementation involves only the SFFT processing and a symbol-wise division, and the range and Doppler estimations are assumed to be decoupled. This estimation approach can be used together with non-uniform subcarrier multiplexing to maintain the full unambiguous range estimation. Doppler compensating approaches such as all-cell Doppler correction (ACDC) [23] can be adapted to OTFS and used to exploit the increased maximum unambiguous Doppler resulting from non-uniform multiplexing in the time (subsymbol) domain. Further comparison between OTFS radar receivers can be found in [72] and Chapter 3 in this dissertation.

In order to implement the spectral-division-based receiver previously presented in Section 3.3.2, the TF representation of the received signal is normalized with respect to the phase of the transmitted TF representation

$$\mathbf{Y}^{\text{norm}}[n,m] = \mathbf{Y}^{\text{RX}}[n,m]\exp\left(-j\Psi[n,m]\right) \tag{4.19}$$

where

$$\Psi[n,m] = \angle(\mathbf{X}_{\text{TF}}[n,m]). \tag{4.20}$$

for every $[n,m]$ that fulfills $\mathbf{X}_{\text{TF}}^{n_{\text{tx}}}[n,m] \neq 0$. After spectral division, an IDFT is performed over the columns and a DFT over the rows. This is the symplectic finite Fourier transform (SFFT), i.e., the transform shown in (4.6). This receiver normalizes the received signal in the time-frequency domain and transforms the result into the delay-Doppler domain. If $[\tau, f_d] = [0,0]$, $\mathbf{Y}_{\text{div}}$ is an all-ones matrix, and its delay-Doppler representation $\mathbf{Y}_{\text{div}}^{\text{DD}}$ appears as a peak in $[0,0]$. For any other pair of $[\tau_p, \upsilon_p]$, the peak in $\mathbf{Y}_{\text{div}}^{\text{DD}}$ is displaced to the corresponding index in the delay-Doppler plane.

4.3.2. ORTHOGONAL MATCHING PURSUIT (OMP)

Sparse reconstruction algorithms from Compressed Sensing (CS) are commonly used to mitigate the loss in dynamic range when non-uniform sampling is used [83]. A wide variety of algorithms with different performance and computational complexity have been proposed in the literature. For the radar simulations in this chapter, the Orthogonal Matching Pursuit (OMP) [84] algorithm is chosen, as it has shown good performance in automotive radar scenarios [32, 58, 85, 86], while being one of the least computationally expensive algorithms described in the CS literature. For more information on the experimental comparison of OMP with other sparse reconstruction algorithms in terms of computational complexity and performance, we refer the reader to [85]. OMP is a greedy iterative algorithm that does not require accurate knowledge of the number of targets in the scene. For N range or M Doppler hypotheses, OMP estimates the matched filter response in each channel as $\text{MF} := \mathbf{A}^{\text{H}}\mathbf{r}_{i-1}$, where i is the iteration index, and $\mathbf{r}_0 = \mathbf{y}$. The sensing matrix for range and Doppler estimation are defined as $\mathbf{A}_\tau = [\mathbf{a}^{\text{T}}(\tau_1), \ldots, \mathbf{a}^{\text{T}}(\tau_N)]$ and $\mathbf{A}_\nu = [\mathbf{a}^{\text{T}}(\nu_1), \ldots, \mathbf{a}^{\text{T}}(\nu_M)]$ respectively, with

$$\mathbf{a}(\tau) := \exp\left(j\ 2\pi\Delta\text{f}\boldsymbol{\alpha}\frac{2r}{c_0}\right) \tag{4.21}$$

$$\mathbf{a}(v) := \exp\left(j\ 2\pi T \boldsymbol{\beta} \frac{\mathrm{v} f_c}{c_0} \right) \tag{4.22}$$

where for a given transmitter, $\boldsymbol{\alpha}$ and $\boldsymbol{\beta}$ are vectors indexing the active subcarriers and subsymbols, respectively, and τ and v represent the delay and Doppler shift hypotheses. For either range or Doppler estimation, the hypothesis n with the highest model match is selected

$$k_{\mathrm{it}} := \arg \max_{n} \mathbf{A}^{\mathrm{H}} \mathbf{r}_{\mathrm{it}-1}. \tag{4.23}$$

A partial sensing matrix is built in each iteration with the hypotheses ψ_{it} of $\mathbf{A}$ selected in the current and previous iterations, such that $\Psi = [a_{\psi_1}, \ldots, a_{\psi_{\mathrm{it}}}]$. The current estimate is calculated as

$$\hat{\mathbf{x}} = \Psi^{-1} \mathbf{y}. \tag{4.24}$$

the residual for the next iteration is $\mathbf{r}_{\mathrm{it}+1} = \mathbf{y} - \hat{\mathbf{y}}$, where $\hat{\mathbf{y}} = \Psi \hat{\mathbf{x}}$. If stopping criteria are not met, the algorithm iterates back to (4.23). A stopping condition is usually defined as the residual power variation or a fixed number of iterations. The complexity of the algorithm grows linearly with the number of iterations and the dimensions of the sensing matrix. Therefore, for $\mathbf{A} \in \mathbb{C}^{P \times Q}$ and k iterations the complexity is $O(kPQ)$.

For radar data, it is possible to apply OMP for only range or Doppler estimation, or sequentially for both. The following approaches to range-Doppler estimation are defined for the sake of clarity.

- **2D-DFT:** The range-Doppler map is calculated through standard IDFT processing along subcarriers, and DFT along the subsymbols. Zero-filling is used for the subcarrier-subsymbol pairs not occupied by the selected transmitter.
- **Hybrid-OMP:** First, the Doppler estimation is performed through standard DFT processing, followed by range estimation with OMP using $\mathbf{A}_\tau$ as sensing matrix. This approach is aimed at minimizing sidelobes in the range dimension, where bright targets near the radar could mask far away targets.
- **2D-OMP:** Range and Doppler estimations are performed sequentially with OMP. The range estimation uses $\mathbf{A}_\tau$ as the sensing matrix, whereas the Doppler estimation uses $\mathbf{A}_v$. The approach offers the benefits of OMP in both range and Doppler dimensions.

4.3.3. NU-OTFS MULTIUSER COMMUNICATIONS RECEIVER

One of the key advantages of the proposed NU-OTFS is increased flexibility in time-frequency allocation when multiplexing multiple communication users or when operating in a crowded spectrum. When it comes to OTFS communication receivers, multiple approaches have been proposed, such as the single-tap equalized, the LMMSE receiver [87] and a message passing algorithm receiver [27]. In this chapter, a standard LMMSE [88] receiver is used to validate the communications performance of the proposed NU-OTFS. The LMMSE receiver is more Doppler tolerant than the single-tap equalized receiver, and its adaptation to NU-OTFS

frames is relatively straightforward. Although the computational complexity is $O(N^3M^3)$, implementations exploiting channel sparsity in the delay-Doppler domain with $O(\frac{MN}{2}\log_2 N)$ complexity have been proposed in [87]. Perfect knowledge of the channel $\mathbf{H}$ is assumed, as channel estimation approaches are not considered in the scope of this research. Assuming a noise variance σ_w^2, the LMMSE estimate of $\mathbf{X}_{\mathrm{DD}}$ is given as

$$\hat{\mathbf{X}}_{\mathrm{DD}}^{(n_{tx})} = (\mathbf{H}^{\mathrm{H}}\mathbf{H} + \sigma_w^2\mathbf{I}_{\mathrm{MN}})^{-1}\mathbf{H}^{\mathrm{H}}\mathbf{Y}_{\mathrm{DD}}^{(n_{tx})} \tag{4.25}$$

where $\mathbf{I}_{\mathrm{MN}}$ is the identity matrix of size $MN \times MN$, and $\mathbf{H} \in \mathbb{C}^{NM\times NM}$ is the delay-Doppler channel matrix with as many non-zero elements in each row as discrete delay-Doppler paths in the channel. The received signal from the n_{Tx} user $\mathbf{Y}_{\mathrm{DD}}$ is retrieved by applying the inverse of the transform in (4.10), that is, the NU-SFFT given by

$$\mathbf{Y}_{\mathrm{DD}}^{(n_{tx})} = \Xi_N^{(n_{tx})}\mathbf{F}_N^{\mathrm{H}}\mathbf{X}_{\mathrm{DD}}^{(n_{\mathrm{tx}})}\mathbf{F}_M\Xi_M^{(n_{tx})} \tag{4.26}$$

More information about the structure of the delay-Doppler channel matrix and the implementation of the LMMSE receiver for OTFS can be found in e.g. [88].

4.4. PERFORMANCE ASSESSMENT OF NU-OTFS

In this section, a series of numerical simulations are performed to validate the viability of NU-OTFS for radar and communications.

4.4.1. MIMO-OTFS RADAR PERFORMANCE EVALUATION

In this section, a numerical analysis of NU-OTFS radar performance under the proposed MIMO configuration is performed. As OTFS is particularly well suited to communications in high mobility channels [89], the radar study is aimed at automotive applications, where high Doppler shifts are common and Radcom applications are gaining popularity. The waveform parameters displayed in Table 4.1 are chosen to match the standards in automotive applications (e.g., [7]).

Table 4.1: OTFS simulations waveform parameters

Parameter	Symbol	Value
Number of delay bins	N	1024
Number of Doppler bins	M	512
Bandwidth	B	1 GHz
Carrier frequency	f_c	77 GHz
Symbol duration	T	1.02 μs
Intercarrier separation	Δf	977 kHz
Cyclic prefix duration	T_{cp}	1 μs
Communication Modulation	(–)	QPSK

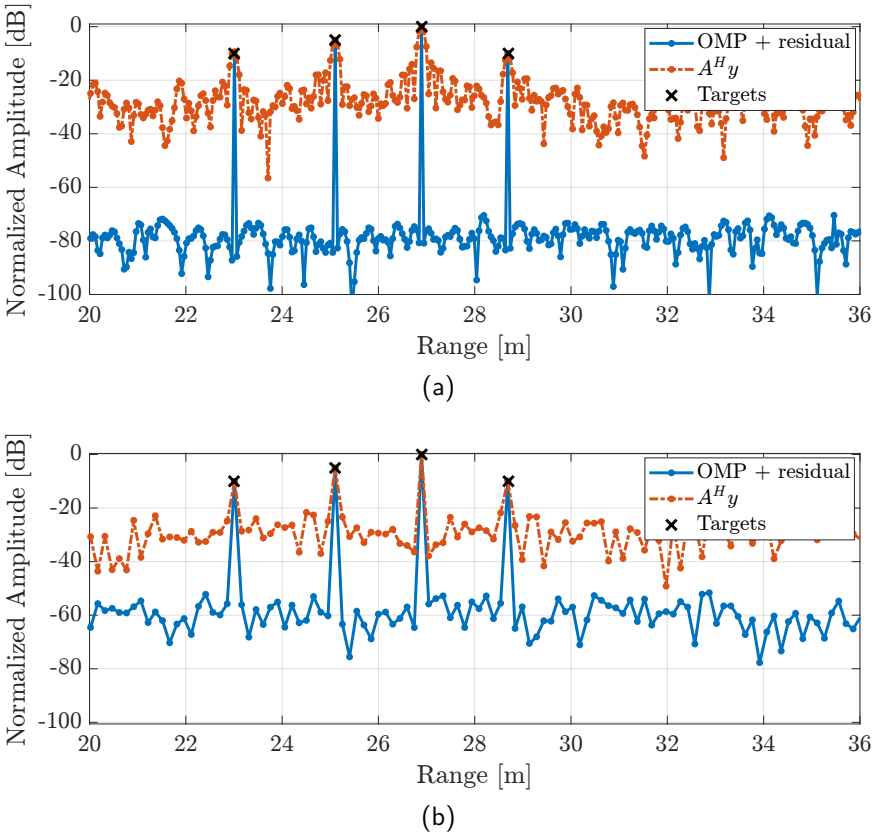

Figure 4.5: Range cuts (a) on-grid targets and grid size of $3N$, and (b) off-grid targets and grid size of N. The signal-to-noise ratio is set to 20 dB.

The performance of the standard DFT-based spectral-division-based receiver is compared to an implementation of the same receiver using OMP as a solver. While OMP is a low-complexity algorithm, its performance in radar estimation is tied to its ability to detect and remove high-power targets accurately. Fig. 4.5 shows the dynamic range gain from using OMP in comparison to the straight correlation of the model $\mathbf{A}$ with the received signal $\mathbf{y}$ (equivalent to standard DFT processing, as $\mathbf{A}$ is a non-uniform DFT matrix). The full potential of the algorithm can be seen in Fig. 4.5a, showing an improvement of around 60 dB when a very fine grid is used in the estimation, and the targets are defined on it. For a more practical scenario, with off-grid targets and a grid size of N, the dynamic-range improvement for the proposed scenario is around 30 dB, as shown in Fig. 4.5b. Specifically, a grid size of N for range estimation and M for Doppler estimation is used, with targets defined off-grid. Scenarios in Fig. 4.5 are simulated with SNR = 20 dB.

Fig. 4.6 shows the integrated sidelobe ratio (ISLR) change in a scene with one target as the number of multiplexed transmitters increases. The ISLR is defined as

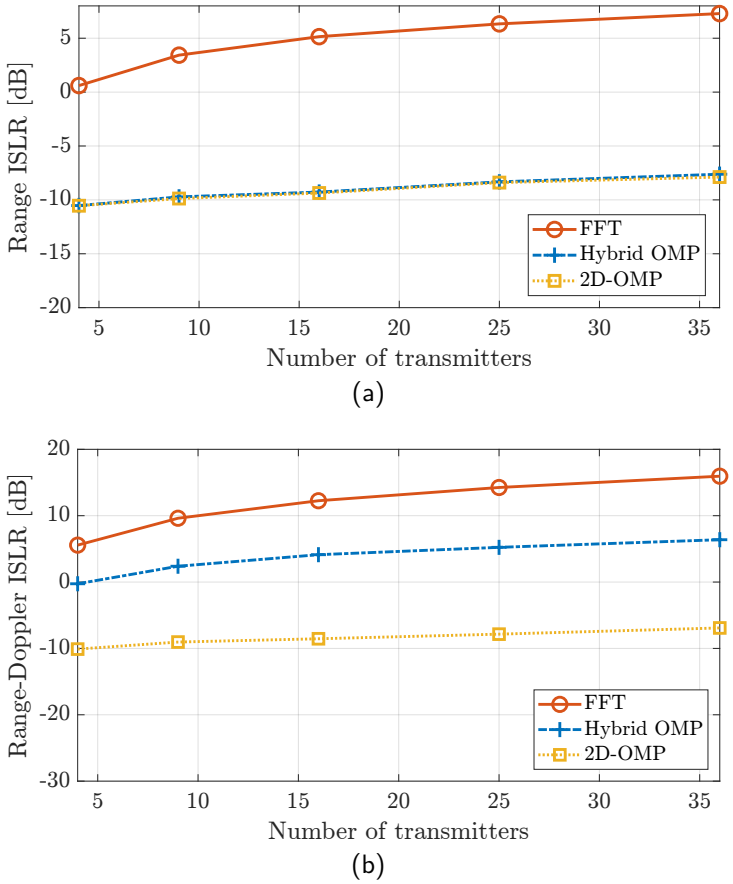

Figure 4.6: ISLR for increasing number of transmitters and different estimation algorithms. (a) ISLR in the range cut; (b) ISLR of the entire range-Doppler surface.

the ratio between the power in the main lobe of the estimation and the integrated power of the sidelobes [90]. As the number of transmitters increases, the sparsity level in the estimation of range and Doppler in each channel increases accordingly. While this causes the ISLR to increase with the number of transmitters for all approaches, there is a 10 dB gain in range-Doppler ISLR when OMP processing is performed in the range dimension (hybrid-OMP), and up to 20 dB when OMP is used to sequentially estimate both range and Doppler (2D-OMP). Moreover, OMP-based approaches degrade visibly slower as the number of transmitters increases. A more visual appreciation of the improvement in sidelobe level can be seen in Fig. 4.7, where a section of the range-Doppler map with four targets shows that the hybrid-OMP (center) and 2D-OMP (right) have progressively lower sidelobes in both range and Doppler when compared with the DFT processing (left).

The spatial spectrum in a simulated system with multiple transmitters and one

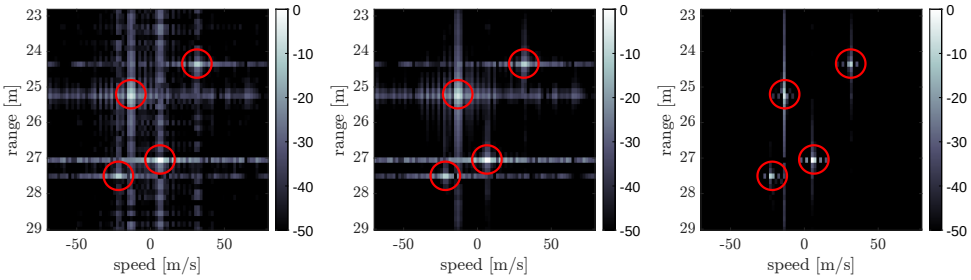

Figure 4.7: Range-Doppler estimation of a single channel of sparse NU-OTFS waveform with four transmitters (i.e., sparsity rate of 25%). On the left, 2D-FFT processing. In the center, hybrid OMP estimation. On the right, 2D OMP.

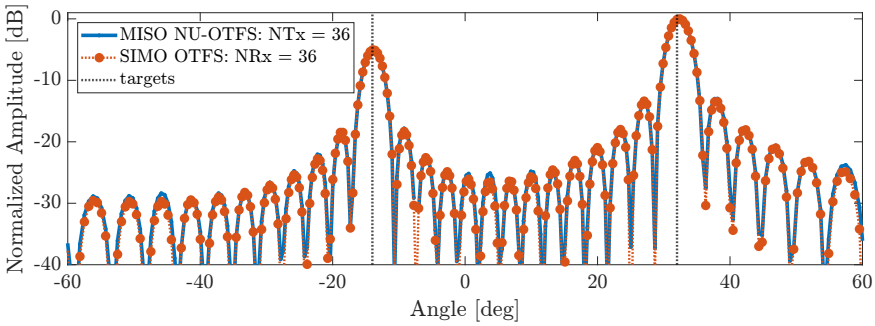

Figure 4.8: Angular estimation of two targets. Comparison between NU-OTFS MISO case with 36 transmitters and one receiver, and standard OTFS SIMO case with one transmitter and 36 receivers. Good matching indicates orthogonality between transmitters in the proposed NU-OTFS waveform.

receiver (MISO) is compared to the spatial spectrum of a SIMO system with one transmitter and multiple receivers to validate the proposed MIMO implementation. In both cases, the equivalent virtual arrays are uniformly spaced at $\lambda/2$ distance, and the spatial spectrum is computed using a discrete Fourier transform over the elements. The comparison is shown in Fig. 4.8, where the MISO result closely resembles the SIMO spectrum, indicating low interference between transmitters. From this, it can be concluded that MIMO operation can happen with low interference between channels. Therefore NU-OTFS is a valid MIMO waveform when paired with the proposed low-complexity spectral division receiver.

4.4.2. EXPERIMENTAL VALIDATION OF OTFS RADAR

In this section, experimental results of OTFS and NU-OTFS radar are presented. The data are gathered using the PARSAX radar [91]. Although PARSAX is a weather radar, it is programmed to send an OTFS frame to measure a static target at 1185 meters

Figure 4.9: PARSAX (left) and measured industrial chimney at approximately 1185 meters from the radar sensor (right).

distance (Fig. 4.9). The OTFS waveform parameters are shown in Table 4.2. A full OTFS frame is transmitted, and the sparse sampling in the time-frequency domain is performed digitally in the acquired signal. This approach serves to evaluate the radar performance of OTFS with experimental data for the first time, both with a full and sparse sampling of the time-frequency resources, while also allowing for the comparison of different multiplexing undersampling schemes.

In the measurements, we compare a fully sampled OTFS frame representing single-transmitter operation with frames with partial time-frequency sampling, simulating a single Tx channel in a MIMO system. For reference, we consider a system with four-channel multiplexing and thus the acquisition of 25% of samples of the full frame. First, we consider interleaved MIMO, where the transmitters are multiplexed through sequential allocation of time-frequency resources (labeled as sparse sequential), such as the example depicted in Fig. 4.2e. Furthermore, we consider a second approach where multiplexing is achieved through quasi-random

Table 4.2: OTFS measurement waveform parameters

Parameter	Symbol	Value
Number of delay bins	N	1024
Number of Doppler bins	M	26
Bandwidth	B	40 MHz
Carrier frequency	f_c	3.315 GHz
Symbol duration	T	25.6 μs
Intercarrier separation	Δf	39.06 kHz
Cyclic prefix duration	T_{cp}	12.8 μs
Communication Modulation	(−)	QPSK

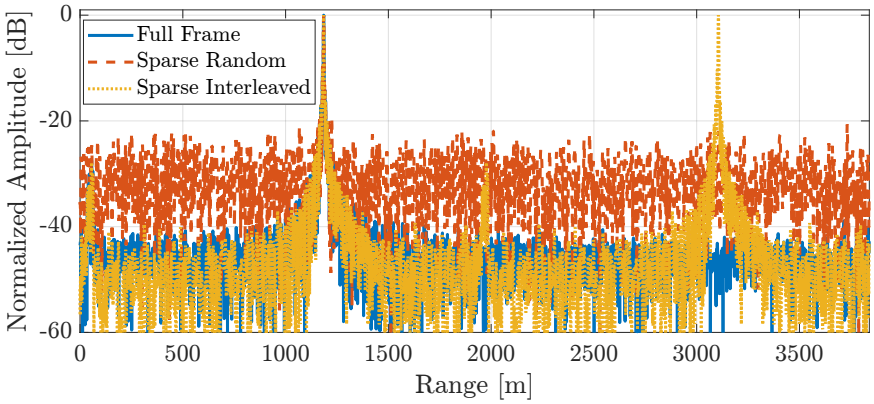

Figure 4.10: Measured DFT-based range profile comparing a full OTFS single-transmitter frame with partially sampled frames for transmitter multiplexing. Sequential multiplexing reduces non-ambiguous parameter estimation, while NU-OTFS random multiplexing reduces the dynamic range.

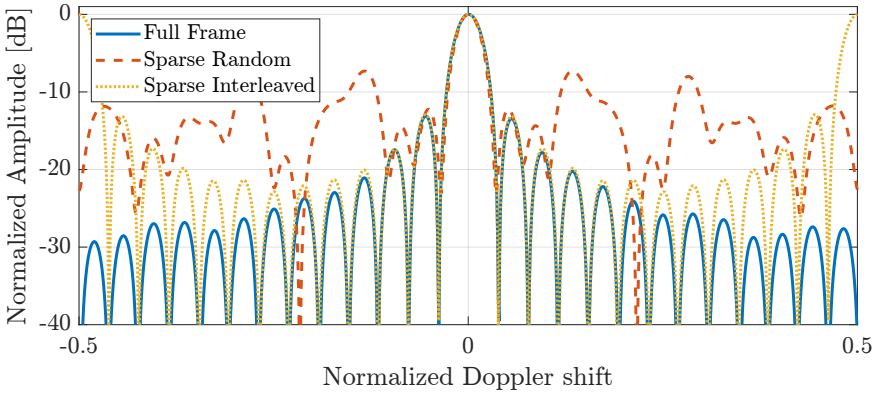

Figure 4.11: Measured DFT-based Doppler profile comparing a full OTFS single-transmitter frame with sparse sampling for transmitter multiplexing.

sparse time-frequency allocation (labeled as sparse random), which is depicted in Fig. 4.2f and representative of NU-OTFS radar operation. Full frame estimation (100% sample acquisition) is used for reference. The estimation of radar parameters is performed using the same receiver as in the numerical validation in the previous section.

The DFT-based range estimation with the described sampling patterns is shown in Fig. 4.10, where the trade-off between sequential and arbitrary multiplexing in time-frequency can be clearly observed. Sequential sparse sampling of the time-frequency domain results in a dynamic range comparable to the fully sampled frame but a reduction in the unambiguous parameter estimation, as made clear

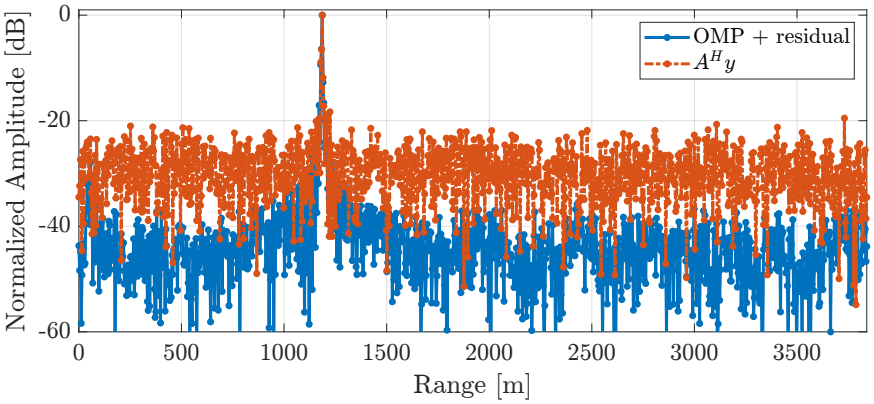

Figure 4.12: Measured NU-OTFS range profile (sparse random) with standard DFT approach versus OMP-based reconstruction. OMP increases the dynamic range to levels comparable to full-frame measurements.

by the appearance of a ghost target in the range domain. On the contrary, random sparse time-frequency patterns reduce the dynamic range under DFT processing but are able to achieve the same unambiguous parameter estimation as the single-transmitter signal. The same effect can be seen in the Doppler estimation shown in Fig. 4.11, where the sequential multiplexing MIMO waveform shows ambiguity at the end of the spectrum, whereas the random time-frequency multiplexing shows a reduction in the dynamic range of the estimation.

In section 4.4.1 it was shown with simulations that sparse reconstruction algorithms (specifically, OMP) can help mitigate the dynamic range loss by using sparse sampling approaches. The results of applying OMP to the NU-OTFS waveform are shown in Fig. 4.12, where the DFT estimation of the randomly multiplexed NU-OTFS signal is compared to the output of OMP. It can be seen that by using OMP, the achieved dynamic range matches the noise floor in the full-frame estimation (Fig. 4.10). These experimental results show that NU-OTFS paired with sparse reconstruction algorithms can achieve comparable dynamic range to fully sampled OTFS frames while being able to multiplex multiple transmitters, thus validating the numerical results for NU-OTFS radar operation presented above.

4.4.3. MU COMMUNICATION PERFORMANCE EVALUATION

To evaluate the communications performance of the proposed MU/MIMO approach, an LMMSE detector [88] is used for an OTFS communication frame propagating through a 3GPP standard *Extended Vehicular A* (EVA) [82] model channel with $n_{\text{taps}} = 9$, and complex gains h_i for $i \in \{1, \ldots, n_{\text{taps}}\}$ modeled as independent Rayleigh fading random variables. The Doppler associated to each tap is sampled from a uniform distribution of shifts in $[0\ v_{\text{max}}]$, with

$$v_{max} = \frac{\Delta \text{v}_{\text{max}}}{c} f_0, \tag{4.27}$$

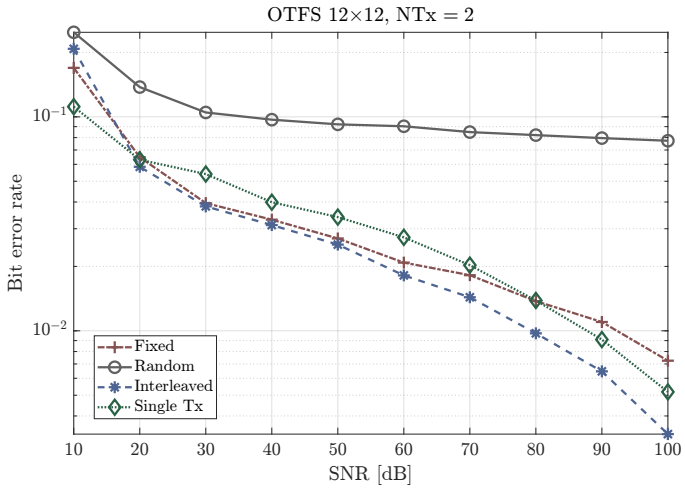

Figure 4.13: Bit error rate for different values of SNR. Standard 3GPP EVA-2 channel used with nine taps and Rayleigh fading. UE speed is sampled for each tap from a uniform distribution between 0 and 100 kph.

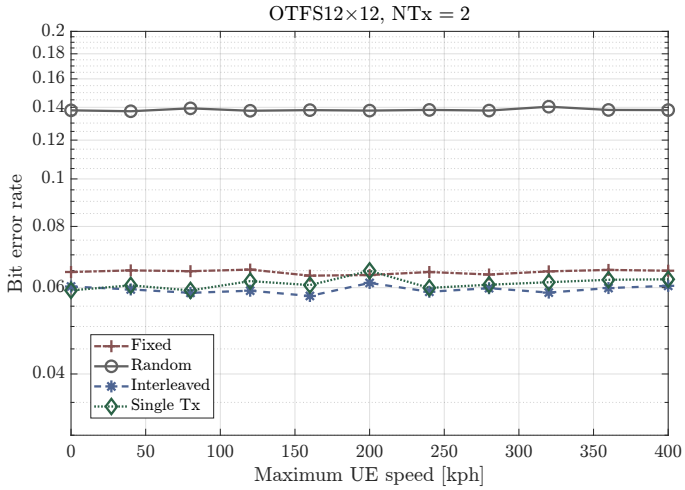

Figure 4.14: Bit error rate versus different distributions of UE speed. Standard 3GPP EVA-2 channel with seven taps, Rayleigh fading, and SNR = 20 dB. UE speed is sampled for each tap from a uniform distribution between 0 and the maximum value.

where v_{max} is the maximum UE speed considered. Fig. 4.13 shows the bit error rate (BER) values for different subcarrier allocation patterns and increasing SNR values. The results are the average of 10000 Monte Carlo simulations with different noise, fading, and user equipment (UE) speed realizations (v_{max} = 100kph). The UE speed

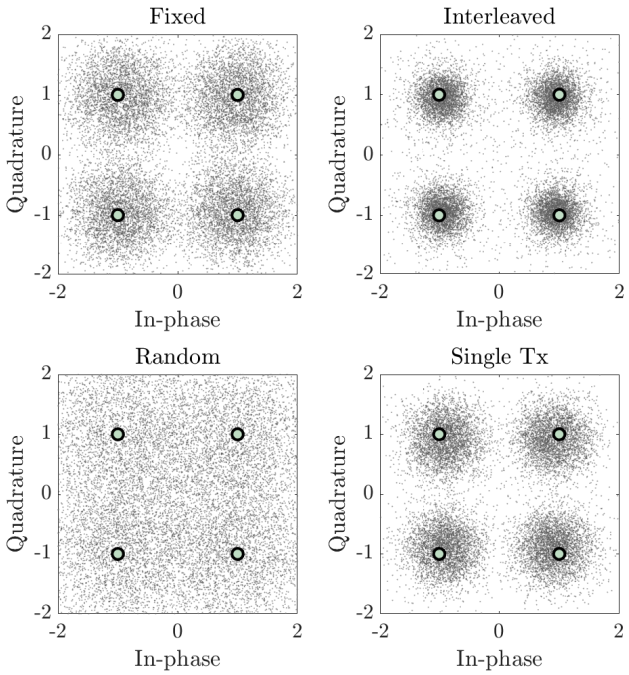

Figure 4.15: IQ distribution of the recovered symbols after an LMSEE receiver in an EVA-2 channel with SNR of 20 dB and maximum UE speed of 100 kph.

value for each Monte Carlo is sampled from a uniform [0 v_{max}] distribution. Random subcarrier allocation is compared to OTFS state-of-the-art interleaved allocation and single Tx performance with no multiplexing. Additionally, a stochastic search accross all channel realisations was used to find generally well-performing subcarrier allocation patterns in terms of BER. One of these selected patterns is used for comparison. In all cases, parameters are sampled from continuous distributions; therefore, off-grid error is present and uncompensated. For methods to mitigate the effects of off-grid error, see e.g. [92].

The simulations show that random subcarrier allocation results in a significant degradation in BER with respect to both the single-user/SISO radar case and the state-of-the-art suggested interleaved subcarrier multiplexing. After closer inspection of the results, it is observed that the BER depends on the chosen subcarrier allocation pattern. Well-performing non-uniform subcarrier allocation patterns from the simulations are selected, and their performance is evaluated. It can be seen that the BER for realistic operating SNR values (i.e., in [15 40] dB [82]) of this pattern, labeled as *Fixed* in Fig. 4.13, closely matches the values of the interleaved pattern, only showing significant differences as SNR increases above realistic values. This validates the viability of the proposed NU-OTFS waveform for user multiplexing. The relatively high BER for all SNR values is attributed to a combination of a

realistic EVA-2 channel, combined with unmitigated off-grid errors present in all simulations. Further study of the potential benefits of the added time-frequency allocation flexibility in NU-OTFS communications in partially interfered channels is left for future work, although similar approaches studied in the framework of cognitive radio have shown increased performance in comparable waveforms such as OFDM [93]. A comparison between the same set of patterns for increasing values of v_{max} is shown in Fig. 4.14, indicating that the chosen fixed subcarrier assignation pattern outperforms the random pattern, and maintains the Doppler tolerance of the interleaved and single-user/SISO radar case.

Fig. 4.15 shows the estimated received QPSK constellations for the same multiplexing patterns and channel conditions at SNR = 20dB, indicating that the interleaved-multiplexing constellation resembles the single-user constellation closely. The QPSK received constellation using the fixed distribution is more spread than the interleaved approach. Still, the symbols can be easily associated to each quadrant instead of the entirely random approach.

4.5. CONCLUSIONS

This chapter has investigated the problem of OTFS ISAC under the requirement of non-uniform allocation of time-frequency resources for multiplexing in MU/MIMO applications and has introduced a novel waveform, NU-OTFS, that enables quasi-arbitrary allocation while preserving the core delay-Doppler structure of OTFS, allowing for more flexible multiplexing schemes. NU-OTFS generalizes and extends previously proposed OTFS multiplexing strategies by using the NU-ISFFT to convert the delay-Doppler symbols into a non-uniform time-frequency frame, thereby unlocking a degree of scheduling freedom that conventional OTFS cannot provide.

Comprehensive numerical simulations and over-the-air radar measurements demonstrate the added value of this flexibility. For radar, NU-OTFS achieves a larger unambiguous Doppler and range window with a manageable side-lobe level when paired with hybrid 1D or 2D sparse estimation, directly addressing the issues with sequential and block-wise OTFS time-frequency multiplexing. For communications, realistic vehicular-channel simulations confirm that the symbol spreading introduced by non-uniform sampling leaves BER essentially unchanged in 5G/6G SNR regimes. Moreover, NU-OTFS shows the same performance in high-mobility scenarios as the interleaved and single-user full-frame approach. Taken together, these results establish NU-OTFS as a performance-enhancing alternative to OTFS ISAC systems whenever fine-grained time-frequency resource allocation is needed for interference avoidance or for extending radar sensing limits.

5

DESIGN OF TIME-FREQUENCY ALLOCATION PATTERNS FOR MIMO NU-OTFS

"The mind was dreaming. The world was its dream."
— Jorge Luis Borges

In this chapter, the performance of MIMO non-uniform orthogonal time-frequency space (NU-OTFS) radar with a high number of transmitters and limited spectral and temporal availability is investigated. NU-OTFS enables the implementation of OTFS communications with quasi-arbitrary distribution of time and frequency resources, increasing the usability of OTFS in spectrally congested scenarios. Moreover, the non-uniform sampling of time and frequency is beneficial for radar performance, as no decrease in resolution or unambiguous parameter estimation occurs. However, radar performance is dependent on the specific time-frequency sampling pattern. This work proposes an optimization framework based on the sidelobe level minimization of the joint ambiguity function of all the operating transmitters. Results show that a substantial sidelobe cancellation can be achieved with specific time-frequency patterns, resulting in viable radar systems with many transmitters in low spectral and temporal availability scenarios.

Parts of this chapter have been published [94]

5.1. INTRODUCTION

In this chapter, the work in the previous chapter and [70] is extended by proposing an optimization strategy for the non-uniform patterns that arise in NU-OTFS for time-frequency multiplexing. We introduce an optimization framework targeting the joint ambiguity function resulting from the incoherent integration of the range and Doppler estimation with multiple transmitters. Incoherent integration is chosen to enable joint detection before direction-of-arrival estimation. Joint design of sparse sampling schemes has found success in other radar applications, such as in [59, 86], where optimization of a joint ambiguity function is used to jointly design arrays in multiple incoherent radar sensors.

As further motivation for the proposed approach, sparse reconstruction algorithms based on group-sparsity [95] can be used to integrate sets of incoherent estimations, and their performance is dependent on a low correlation between the hypotheses of a block-sparse model defined by the sampling scheme (equivalent sidelobe level minimization in the joint ambiguity function). Therefore, the proposed metric is well-tailored for sparse reconstruction algorithms, typical for non-uniformly sampled radar estimation problems [85]. The proposed approach also extends the work in [34] as it tackles the optimization of the 2D joint ambiguity function instead of only subcarrier allocation. In this work, we leverage the low-rank structure of the patterns that arise in NU-OTFS to reduce the number of optimization variables and make the problem simple to extend to the 2D case.

The remainder of the chapter is structured as follows. Section 5.2 presents the signal model and receiver for MIMO NU-OTFS radar. Section 5.3 describes the proposed optimization framework based on the joint range-Doppler ambiguity function. Section 5.4 presents a parametric study using the proposed optimization framework for NU-OTFS radar systems considering different amounts of transmitters and spectro-temporal availability. A chapter summary is given in Section 5.5.

5.2. NU-OTFS MIMO RADAR

In this section, the signal model for NU-OTFS MIMO radar is presented. For more details on the derivation of NU-OTFS from the standard OTFS signal model, we refer the reader to [70]. Consider a MIMO OTFS radar system transmitting a message $\mathbf{X}_{\mathrm{DD}}^{\mathrm{MIMO}} \in \mathbb{C}^{N\times M}$ defined in a $N \times M$ delay-Doppler grid, with N delay bins and M Doppler bins

$$\mathbf{X}_{\mathrm{DD}}^{\mathrm{MIMO}} = \begin{bmatrix} \mathbf{X}_{\mathrm{DD}}^{(1,1)} & \cdots & \mathbf{X}_{\mathrm{DD}}^{(1,\sqrt{N_{\mathrm{Tx}}})} \\ \vdots & \ddots & \vdots \\ \mathbf{X}_{\mathrm{DD}}^{(\sqrt{N_{\mathrm{Tx}}},1)} & \cdots & \mathbf{X}_{\mathrm{DD}}^{(\sqrt{N_{\mathrm{Tx}}},\sqrt{N_{\mathrm{Tx}}})} \end{bmatrix} \tag{5.1}$$

where $\mathbf{X}_{\mathrm{DD}}^{(p,q)} \in \mathbb{C}^{(N/\sqrt{N_{\mathrm{Tx}}})\times(M/\sqrt{N_{\mathrm{Tx}}})}$ are the delay-Doppler messages associated to different transmitters, and $\mathbf{X}_{\mathrm{DD}}^{\mathrm{MIMO}} \in \mathbb{C}^{N\times M}$ is the OTFS MIMO frame for a monostatic OTFS radar with N_{Tx} transmitters. As in the previous chapter, it is assumed that N_{Tx} is a square number to assume equal distribution of the messages in the delay and Doppler domain. This condition is not necessary, as any non-prime number

of transmitters can be distributed in tiles across the delay-Doppler domain. An example of this symbol arrangement in the delay-Doppler domain is shown in Fig. 4.2d. A mapping between $\mathbf{X}_{\mathrm{DD}}$ and a TF representation with a quasi-arbitrary TF occupancy pattern can be achieved. This mapping is denoted here as the non-uniform symplectic finite Fourier transform (NU-ISFFT). For transmitter n_{Tx}, let $\boldsymbol{\xi}_{N,n_{\mathrm{Tx}}} \in \{0,1\}^{N\times 1}$ be a vector indexing the active subcarriers, $\boldsymbol{\xi}_{M,n_{\mathrm{Tx}}} \in \{0,1\}^{M\times 1}$ a vector indexing the active time subsymbols, $\Xi_N^{(n_{\mathrm{Tx}})} = \mathrm{diag}\{\boldsymbol{\xi}_{N,n_{\mathrm{Tx}}}\}$, and $\Xi_M^{(n_{\mathrm{Tx}})} = \mathrm{diag}\{\boldsymbol{\xi}_{M,n_{\mathrm{Tx}}}\}$, then

$$\mathbf{X}_{\mathrm{TF}}^{(n_{\mathrm{Tx}})} = \Xi_N^{(n_{\mathrm{Tx}})}\mathbf{F}_N\mathbf{X}_{\mathrm{DD}}^{(n_{\mathrm{Tx}})}\mathbf{F}_M^{\mathrm{H}}\Xi_M^{(n_{\mathrm{Tx}})} \tag{5.2}$$

$$\mathbf{X}_{\mathrm{TF}} = \sum_{n_{tx}=1}^{N_{\mathrm{Tx}}} \mathbf{X}_{\mathrm{TF}}^{(n_{\mathrm{Tx}})} \tag{5.3}$$

where $\mathbf{F}_{\mathrm{N}} \in \mathbb{C}^{N\times N}$ and $\mathbf{F}_{\mathrm{M}} \in \mathbb{C}^{M\times M}$ are normalized Fourier transform matrices. $\mathbf{X}_{\mathrm{TF}}^{(n_{\mathrm{Tx}})} \in \mathbb{C}^{N\times M}$ is the sparse time-frequency representation of the signal associated to the n_{Tx}-th transmitter, and $\mathbf{X}_{\mathrm{TF}}^{\mathrm{MIMO}} \in \mathbb{C}^{N\times M}$ is the time-frequency representation of all the transmitters. To achieve arbitrary non-overlapping time representations, it is necessary that

$$\left(\boldsymbol{\xi}_{N,n_{\mathrm{Tx}}}\boldsymbol{\xi}_{M,n_{\mathrm{Tx}}}^{T}\right) \odot \left(\boldsymbol{\xi}_{N,n'_{\mathrm{Tx}}}\boldsymbol{\xi}_{M,n'_{\mathrm{Tx}}}^{T}\right) = \mathbf{0} \quad \forall \quad n_{\mathrm{Tx}} \neq n'_{\mathrm{Tx}} \tag{5.4}$$

where $\mathbf{0}$ is the $N \times M$ all zero matrix. Equation (5.4) forces that no pair of subcarrier-subsymbol is occupied by more than one transmitter. Uniform sampling is performed in the subsymbol dimension if $\Xi_M = \mathbf{I}$, and in the subcarrier if $\Xi_N = \mathbf{I}$. The TF patterns arising from the NU-ISFFT are not truly arbitrary, but rather the intersections of two one-dimensional arbitrary assignations of time and subcarrier resources defined by $\boldsymbol{\xi}_{M,n_{\mathrm{Tx}}}$ and $\boldsymbol{\xi}_{N,n_{\mathrm{Tx}}}$ respectively. A standard OTFS modulation approach of (5.1) would give rise to an interleaved TF pattern, as shown in Fig. 4.2e, whereas the NU-OTFS approach results in non-uniform TF patterns like the one depicted in Fig. 4.2f. Finally, the Heisenberg transform converts the TF signal into the time domain for transmission.

$$\mathbf{s} = \mathrm{vec}\left(\mathbf{F}_{\mathrm{N}}^{\mathrm{H}}\mathbf{X}_{\mathrm{TF}}\right) \tag{5.5}$$

Consider now an echo from the signal described in (5.5) from a point target at relative azimuth angle ϕ, in an NU-OTFS MIMO system with N_{Tx} transmitters and N_{Rx} receivers arranged in a one-dimensional array, with their positions given by $\mathbf{d}_{\mathrm{Tx}} \in \mathbb{R}^{N_{\mathrm{Tx}}\times 1}$ and $\mathbf{d}_{\mathrm{Rx}} \in \mathbb{R}^{N_{\mathrm{Rx}}\times 1}$ respectively. The steering vector

$$\mathbf{a}(\phi) := \exp\left(j\frac{2\pi}{\lambda}\mathbf{d}_{\mathrm{Tx}}\sin(\phi)\right) \tag{5.6}$$

with $\mathbf{a}(\phi) \in \mathbb{C}^{N_{\mathrm{Tx}}\times 1}$ captures the direction-of-arrival dependent phase shift associated with the position of the transmitters. Analogously, the angle-dependent phase shift at each receiver is given by

$$\mathbf{b}(\phi) := \exp\left(j\frac{2\pi}{\lambda}\mathbf{d}_{Rx}\sin(\phi)\right). \tag{5.7}$$

with $\mathbf{b}(\phi) \in \mathbb{C}^{N_{\mathrm{Rx}} \times 1}$. Then by adding (5.6) and (5.7) to the SISO range-Doppler signal model presented in Chapter 3, the received signal at receiver n_{Rx} can be written as

$$\mathbf{r}_{n_{\mathrm{Rx}}}^{\mathrm{MIMO}} = \mu\psi b_{n_{\mathrm{Rx}}}(\phi) \sum_{n_{\mathrm{Tx}}=1}^{N_{\mathrm{Tx}}} a_{n_{\mathrm{Tx}}}(\phi)\mathrm{vec}\left(\mathbf{\Gamma_1}\mathbf{F}_{\mathrm{N}}^{\mathbf{H}}\mathbf{A}\mathbf{X}_{\mathrm{TF}}^{\mathrm{MIMO}}\mathbf{\Gamma_2}\right) \tag{5.8}$$

where n_{Tx} and n_{Rx} denote the transmitter and receiver index respectively, and $a_{n_{\mathrm{Tx}}}$ and $b_{n_{\mathrm{Rx}}}$ denote the steering vector entry associated with this index. Co-located MIMO and far-field targets are assumed; therefore, the delay and Doppler shifts associated with each transmit-receive pair are considered the same. The TF representation of the signal at receiver n_{Rx} is given by

$$\mathbf{Y}_{\mathrm{TF},n_{\mathrm{Rx}}}^{\mathrm{MIMO}} = \mathbf{F}_{\mathrm{N}}\mathrm{vec}_{N\times M}^{-1}(\mathbf{r}_{n_{\mathrm{Rx}}}^{\mathrm{MIMO}}) \tag{5.9}$$

Henceforth, a single receiver is assumed, and the n_{Rx} suffix is omitted to simplify notation. This can be done without loss of generality, as receiving and separating the different transmit signals is invariant to the number of receivers. Each transmitted signal can now be separated in the receiver by

$$\mathbf{Y}_{\mathrm{TF}}^{(n_{\mathrm{Tx}})} = \mathbf{\Xi}_N^{(n_{\mathrm{Tx}})}\mathbf{Y}_{\mathrm{TF}}^{\mathrm{MIMO}}\mathbf{\Xi}_M^{(n_{\mathrm{Tx}})} \tag{5.10}$$

thus retrieving the signal associated to the n_{Tx} transmitter, and completing the MIMO implementation of NU-OTFS. Further steps involve the range-Doppler estimation in each transmit-receive pair.

Regarding OTFS radar receivers, multiple options have been proposed in the literature. In this work, a radar receiver based on spectral division in the time-frequency domain is used. The implementation involves only the SFFT processing and a symbol-wise division. This estimation approach can be used with non-uniform multiplexing to maintain the full, unambiguous parameter estimation. A discussion about the properties of the existing receivers for OTFS can be found in [72].

As in the previous chapters, we use the spectral-division-based receiver for radar parameter estimation. The received signal is normalized by the phase of the transmitter TF signal

$$\mathbf{Y}^{\mathrm{norm}}[n,m] = \mathbf{Y}^{\mathrm{RX}}[n,m]\exp(-j\Psi[n,m]) \tag{5.11}$$

where

$$\Psi[n,m] = \angle(\mathbf{X}_{\mathrm{TF}}[n,m]). \tag{5.12}$$

for every $[n,m]$ that fulfills $\mathbf{X}_{\mathrm{TF}}^{n_{\mathrm{tx}}}[n,m] \neq 0$. After phase normalisation, SFFT is performed to represent the signal in the delay-Doppler domain. If $[\tau, f_d] = [0,0]$, $\mathbf{Y}_{\mathrm{div}}$ is an all-ones matrix, and its delay-Doppler representation $\mathbf{Y}_{\mathrm{div}}^{\mathrm{DD}}$ appears as a peak in $[0,0]$. For any other pair of $[\tau_p, \upsilon_p]$, the peak in $\mathbf{Y}_{\mathrm{div}}^{\mathrm{DD}}$ is displaced to the corresponding index in the delay-Doppler plane.

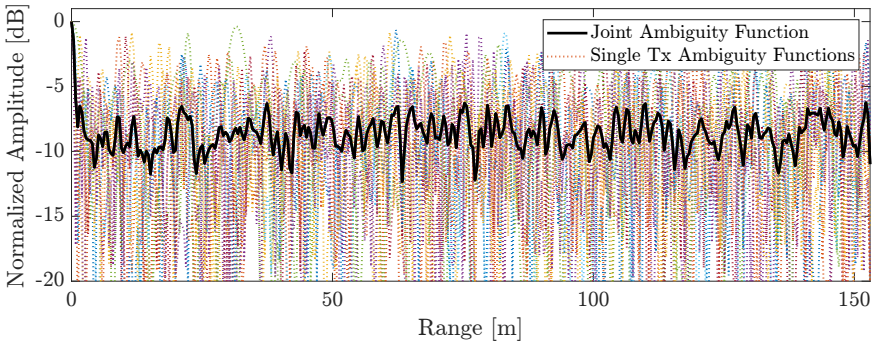

Figure 5.1: Joint range ambiguity function cut for $N_{Tx} = 121$, $N = 256$, $M = 256$, and $S = 0.75$. The dotted curves represent the ambiguity functions of each transmitter.

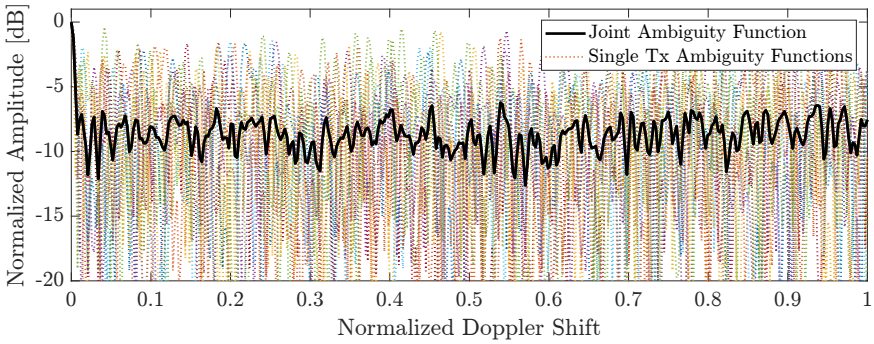

Figure 5.2: Joint Doppler ambiguity function cut for $N_{Tx} = 121$, $N = 256$, $M = 256$, and § = 0.75. The dotted curves represent the ambiguity functions of each transmitter.

5.2.1. JOINT AMBIGUITY FUNCTION FOR NU-OTFS MIMO RADAR

Based on the previously presented receiver, a joint range-Doppler ambiguity function (AF) can be formulated to be used as a reference for optimizing the transmitter time-frequency resource allocation. To formulate the range-Doppler AF associated to each transmitter, the range and Doppler sensing matrices associated to the estimation process are defined as $\mathbf{A}_\tau = [\mathbf{a}_\tau^{\mathrm{T}}(\tau_1), \ldots, \mathbf{a}_\tau^{\mathrm{T}}(\tau_N)]$ and $\mathbf{A}_\nu = [\mathbf{a}_\nu^{\mathrm{T}}(\nu_1), \ldots, \mathbf{a}_\nu^{\mathrm{T}}(\nu_M)]$ respectively, with

$$\mathbf{a}_\tau^{(n_{\mathrm{Tx}})}(\tau) := \exp\left(j\ 2\pi \Delta \mathrm{f} \boldsymbol{\alpha}^{(n_{\mathrm{Tx}})} \frac{2r}{c_0}\right) \tag{5.13}$$

$$\mathbf{a}_\nu^{(n_{\mathrm{Tx}})}(\nu) := \exp\left(j\ 2\pi T \boldsymbol{\beta}^{(n_{\mathrm{Tx}})} \frac{\mathrm{v} f_c}{c_0}\right) \tag{5.14}$$

where for a given transmitter, $\boldsymbol{\alpha}$ and $\boldsymbol{\beta}$ are vectors indexing the active subcarriers and subsymbols, respectively, and τ and ν represent the delay and Doppler shift hypotheses. The vectors $\boldsymbol{\alpha}$ and $\boldsymbol{\beta}$ can be synthesized directly from $\boldsymbol{\xi}_{N,n_{\mathrm{Tx}}}$ and $\boldsymbol{\xi}_{M,n_{\mathrm{Tx}}}$

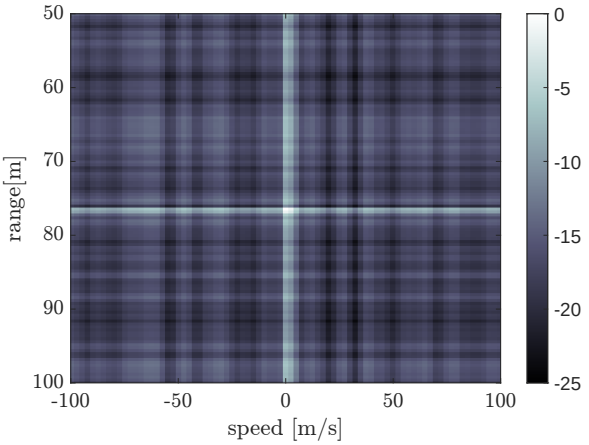

Figure 5.3: Joint range-Doppler ambiguity function cut for $N_{Tx} = 121$, $N = 256$, $M = 256$, and $S = 0.75$.

for each transmitter as the index of their non-zero entries. The ambiguity functions associated with the estimation process are defined as

$$\mathrm{AF}^{(n_{\mathrm{Tx}})}(\tau - \tau_{\mathrm{ref}}) = \mathbf{A}_{\tau}^{\mathrm{H}} \mathbf{a}_{\tau}(0) \in \mathbb{C}^{1\times N} \tag{5.15}$$

$$\mathrm{AF}^{(n_{\mathrm{Tx}})}(\nu - \nu_{\mathrm{ref}}) = \mathbf{A}_{\nu}^{\mathrm{H}} \mathbf{a}_{\nu}(0) \in \mathbb{C}^{1\times M} \tag{5.16}$$

for range and Doppler, respectively. Next, we can leverage the fact that the time allocation for each transmitter is constant in every subcarrier in which it is active (and, equivalently, the subcarrier allocation pattern is static for each time in which the transmitter is active) to formulate the range-Doppler ambiguity function for a given transmitter as

$$\mathrm{AF}^{(n_{\mathrm{Tx}})}((\tau - \tau_{\mathrm{ref}}), (\nu - \nu_{\mathrm{ref}})) = \mathrm{AF}(\tau - \tau_{\mathrm{ref}})^{\mathrm{H}} \mathrm{AF}(\nu - \nu_{\mathrm{ref}}) \tag{5.17}$$

For conciseness, we will refer to $\mathrm{AF}((\tau - \tau_{\mathrm{ref}}), (\nu - \nu_{\mathrm{ref}})) \in \mathbb{C}^{N\times M}$ as $\mathrm{AF}(\tau, \nu)$ henceforth. Finally, when considering all the transmitters in our MIMO system, we define the joint incoherent range-Doppler AF as

$$\mathrm{AF}(\tau, \nu) := \sum_{n_{\mathrm{Tx}}=1}^{N_{\mathrm{Tx}}} |\mathrm{AF}^{(n_{\mathrm{Tx}})}(\tau, \nu)| \in \mathbb{C}^{N\times M} \tag{5.18}$$

The joint ambiguity function in (5.18) simply integrates the individual ambiguity functions associated with each transmitter's waveform. In this integration, effects such as sidelobe cancellation and mainlobe sharpening can be achieved with the careful design of the sampling schemes associated with each transmitter that generates the individual AFs, as shown in Figs. 5.1 and 5.2.

5.3. TIME-FREQUENCY PATTERN OPTIMIZATION

This section presents the optimization approach of time-frequency sampling patterns for NU-OTFS under spectral constraints. The optimization goal is to minimize the peak sidelobe ratio (PSR) of the joint ambiguity function associated with each time-frequency sampling pattern. This metric is selected instead of the ISLR because for a given sparsity level in the TF pattern, the total energy in the sidelobes (affecting ISLR) remains close to constant, while the distribution of this energy varies considerably. The cost function is given by

$$\min_{\hat{\boldsymbol{\xi}}_N, \hat{\boldsymbol{\xi}}_M} f_{\mathrm{SLL}}(\hat{\boldsymbol{\xi}}_N, \hat{\boldsymbol{\xi}}_M) \tag{5.19}$$

where $f_{\mathrm{SLL}}(\hat{\boldsymbol{\xi}}_N, \hat{\boldsymbol{\xi}}_M)$ is a function that returns the sidelobe level (SLL) of the joint AF defined in (5.18). The vectors $\hat{\boldsymbol{\xi}}_N \in \mathbb{R}^{N\times 1} : [0 \;\; N_{\mathrm{Tx}}]$ and $\hat{\boldsymbol{\xi}}_M \in \mathbb{R}^{M\times 1} : [0 \;\; N_{\mathrm{Tx}}]$ are real valued versions of the time-frequency pattern vectors. The values of $\hat{\boldsymbol{\xi}}_N$ and $\hat{\boldsymbol{\xi}}_M$ are mapped to specific transmitters based on the amplitude, so $\boldsymbol{\xi}_{N,n_{\mathrm{Tx}}}$ and $\boldsymbol{\xi}_{N,n_{\mathrm{Tx}}}$ can be generated. Additionally, several constraints are imposed on the problem:

1. No overlap is allowed between time-frequency resources assigned to different transmitters to ensure transmitter separability at reception

$$\left(\boldsymbol{\xi}_{N,n_{\mathrm{Tx}}} \boldsymbol{\xi}^T_{M,n_{\mathrm{Tx}}}\right) \odot \left(\boldsymbol{\xi}_{N,n'_{\mathrm{Tx}}} \boldsymbol{\xi}^T_{M,n'_{\mathrm{Tx}}}\right) = \mathbf{0} \quad \forall \quad n_{\mathrm{Tx}} \neq n'_{\mathrm{Tx}} \tag{5.20}$$

2. Each transmitter is assigned the same amount of time and frequency resources as the rest,

$$\|\boldsymbol{\xi}_{N,n_{\mathrm{Tx}}}\|_{\ell_0} = \|\boldsymbol{\xi}_{N,n'_{\mathrm{Tx}}}\|_{\ell_0} \quad \forall \quad n_{\mathrm{Tx}} \neq n'_{\mathrm{Tx}} \tag{5.21}$$

$$\|\boldsymbol{\xi}_{M,n_{\mathrm{Tx}}}\|_{\ell_0} = \|\boldsymbol{\xi}_{M,n'_{\mathrm{Tx}}}\|_{\ell_0} \quad \forall \quad n_{\mathrm{Tx}} \neq n'_{\mathrm{Tx}}. \tag{5.22}$$

3. The total amount of time and frequency resources used by all the transmitters in the system is limited by the spectro-temporal availability given by $S : [0 \; 1]$, with increasing values of S indicating an increasing percentage of unavailable spectro-temporal resources in the band. It can be written as

$$\sum_{n_{\mathrm{Tx}}=1}^{N_{\mathrm{Tx}}} \|\boldsymbol{\xi}_{N,n_{\mathrm{Tx}}}\|_{\ell_0} \leq (1-S)N \tag{5.23}$$

Table 5.1: OTFS waveform parameters

Parameter	Symbol	Value
Number of delay bins	N	256
Number of Doppler bins	M	256
Bandwidth	B	0.25 GHz
Carrier frequency	f_c	77 GHz
Symbol duration	T	1.02 μs
Intercarrier separation	Δf	977 kHz
Communication Modulation	$(-)$	QPSK

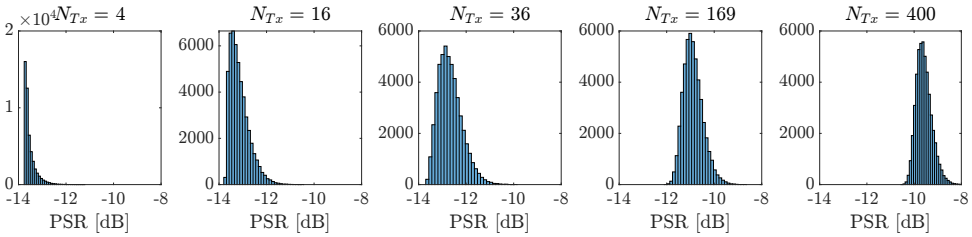

Figure 5.4: Histograms showing the distribution of the peak-to-sidelobe ratio (PSR) in the range-Doppler ambiguity function for 50000 iterations of random time-frequency allocation patterns. In this example, $N = 256$, $M = 256$, and $S = 0$.

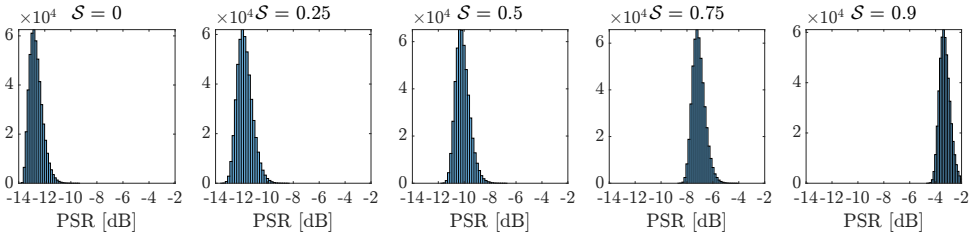

Figure 5.5: Histograms showing the distribution of the peak-to-sidelobe ratio (PSR) in the range-Doppler ambiguity function for 500000 iterations of random time-frequency allocation patterns. In this example, $N = 256$, $M = 256$, and $N_{Tx} = 36$

$$\sum_{n_{\mathrm{Tx}}=1}^{N_{\mathrm{Tx}}} \|\boldsymbol{\xi}_{M,n_{\mathrm{Tx}}}\|_{\ell_0} \leq (1-S)M \tag{5.24}$$

A global optimization algorithm, namely, simulated annealing [96], is used to find candidate patterns. Simulated annealing has proved helpful in solving similar problems, such as array design [59] for MIMO radar.

Minimizing the SLL (or PSR for peak-sidelobe ratio) promotes sidelobe cancellation to maximize the PSR in the joint AF. Some exemplary results of the optimization showcasing the effect of sidelobe cancellation can be seen in Fig. 5.1 and Fig. 5.2 for range and Doppler cuts, respectively. It is shown that the resulting peak sidelobe level in the joint AF is considerably lower than in the AFs of individual transmitters. A section of the resulting 2D joint AF is shown in Fig. 5.3, indicating that the sidelobe-cancellation effects extend to the rest of the range-Doppler hypotheses.

As the 2D patterns in NU-OTFS arise from the two vectors $\hat{\boldsymbol{\xi}}_N$ and $\hat{\boldsymbol{\xi}}_M$, not only is the range-Doppler AF simple to calculate as in (5.17), but also the number of optimization variables is reduced to $N+M$, instead of the expected NM variables for entirely arbitrary 2D patterns. This reduction in dimensionality and computational cost of the goal function enables the optimization of 2D patterns while keeping a similar complexity to 1D pattern optimization.

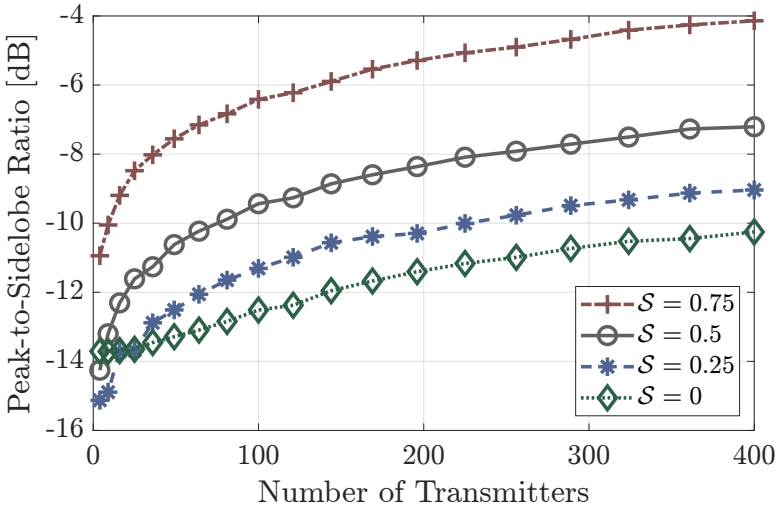

Figure 5.6: Achieved PSR after optimization for an increasing number of transmitters and different values of S.

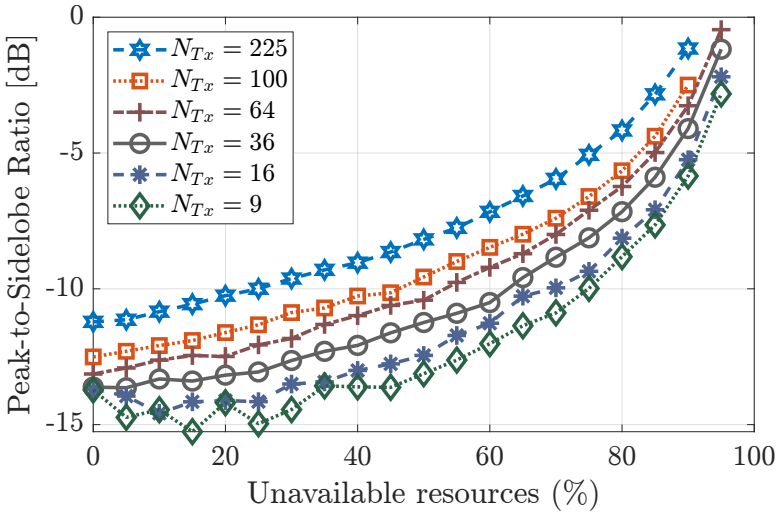

Figure 5.7: Achieved PSR after optimization for an increasing value of S and different amount of transmitters.

5.4. OPTIMIZATION-BASED PARAMETRIC STUDY

This section presents a parametric study of time-frequency allocation patterns for an exemplary NU-OTFS waveform. The static parameters of the waveform under study are shown in Table 5.1. It is assumed that resource allocation is even among transmitters (all transmitters are assigned the same amount of time and frequency

resources). Additionally, when part of the spectro-temporal resources are unavailable ($S > 0$), it is assumed that only $(1-S)N$ subcarriers and $(1-S)M$ subsymbols are available to be occupied by the NU-OTFS waveform.

First, the distribution of the cost function values (namely, the sidelobe level of the joint ambiguity function) for random realizations of time-frequency patterns is studied. Fig. 5.4 shows the distribution of PSR for random realizations of time-frequency patterns and an increasing amount of transmitters. It can be seen that for a low number of transmitters, most patterns offer a comparatively low SLL. As the number of transmitters increases, the best patterns are less likely to occur, increasing the potential benefits of pattern design. Interestingly, the spread is wider for an intermediate number of transmitters than for a very high number. Fig. 5.5 shows similar results but for an increasing amount of unavailable resources. The expected PSR increases as the value of S increases due to the reduction in available spectral resources. The distribution widens noticeably for values around $S \leq 0.5$, but the best achievable PSR values are reduced by less than 2 dB, making time-frequency pattern design more critical.

Next, the proposed optimization framework is used to minimize the sidelobe level in the joint ambiguity function for various values of transmitters and spectro-temporal availability. Fig. 5.6 shows the evolution of the PSR for an increasing number of transmitters after optimization. For a low number of transmitters, the increase in achievable PSR is relatively rapid with respect to the number of transmitters. This effect is even more pronounced for low spectro-temporal availability. As the number of transmitters increases to higher values, the degradation of the PSR becomes less severe, suggesting that in MIMO radar systems where a high baseline number of transmitters is required, the total amount is much less significant to the overall performance than the amount of spectro-temporal available resources. The parametric study of optimized time-frequency patterns for increasing values of S, depicted in Fig. 5.7, shows that the rate of degradation of the PSR value increases significantly for values of $S > 0.6$, regardless of the number of transmitters. Moreover, it appears that an increase in the number of transmitters results in a loss of PSR that is not strongly dependent on the spectro-temporal availability.

5.5. CONCLUSIONS

This chapter has, for the first time, quantified and optimized the scalability of NU-OTFS MIMO radar to a high number of transmitters under spectro-temporal constraints. A new low-complexity optimization framework, built around the range–Doppler joint ambiguity function and leveraging the low-rank structure of NU-OTFS time-frequency occupation patterns, keeps the computational complexity low while preserving near-optimal sidelobe suppression. The resulting patterns are well suited to sparse reconstruction, as minimizing the sidelobe level after incoherent integration is equivalent to minimizing the maximum correlation between hypotheses in the sensing matrix for joint range and Doppler estimation. Parametric studies with an exemplary NU-OTFS waveform have shown the scalability of NU-OTFS MIMO radar to various scenarios with diverse quantities of transmitters and

spectro-temporal availability. Together, these insights and the proposed optimization framework bridge the gap between theoretical multiplexing flexibility and large-scale practical deployment, making NU-OTFS a compelling architecture for dense ISAC networks.

6

EXPERIMENTAL VALIDATION OF NU-OTFS MIMO RADAR

"Experience is merely the name men gave to their mistakes."
— Oscar Wilde

In this chapter, we present an experimental validation of MIMO non-uniform orthogonal time-frequency space (NU-OTFS) radar based on polarimetric measurements. NU-OTFS enables the implementation of OTFS communications and radar with non-overlapping quasi-arbitrary representations in the time-frequency domain, which can be advantageous for MIMO radar and multi-user communications. Non-uniform sampling of the time-frequency plane is helpful for MIMO radars to ensure transmitter separability without reducing non-ambiguous parameter estimation. The viability of NU-OTFS for MIMO radar is validated in a real polarimetric system by showing that different non-overlapping time-frequency representations of NU-OTFS can be separated in a receiver with prior knowledge of the transmit pattern, thus enabling MIMO radar implementations. As non-uniform sparse sampling is a form of Compressed Sensing, the measurements are validated through sparse-reconstruction algorithms.

Parts of this chapter have been published in [97]

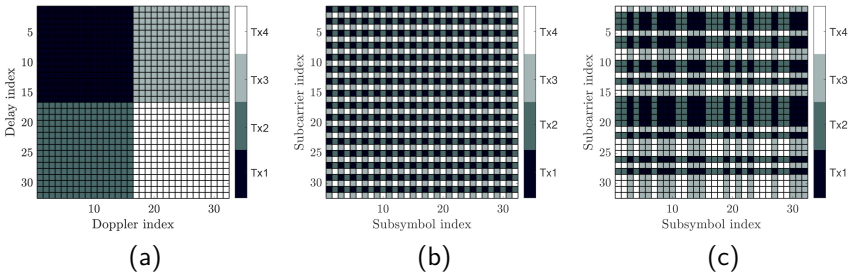

Figure 6.1: Depiction of multiplexing strategy: (a) Four transmitters multiplexed in the delay-Doppler domain; (b) interleaved 2D multiplexing in the time-frequency domain; (c) quasi-arbitrary 2D multiplexing in the TF domain with NU-OTFS.

6.1. INTRODUCTION

In the previous chapters, numerical simulations show that NU-OTFS enables quasi-arbitrary occupation of the time-frequency grid while achieving a similar communication performance and Doppler tolerance as OTFS. The performance was, however, demonstrated only for the single Tx case on simulated and semi-experimental data.

In this chapter, we extend the numerical work presented in chapters 4 and 5, as well as [70] and [94], with the first experimental validation of the MIMO capabilities of NU-OTFS through polarimetric measurements. The MIMO principle of channel separation in the receivers is validated by observing the polarimetric response of two non-overlapping NU-OTFS frames transmitted simultaneously in orthogonal polarizations. Furthermore, sparse reconstruction algorithms are tested on the measurements to explore their compatibility with the waveform. The remainder of the chapter is structured as follows: Section 6.2 briefly introduces a signal model for MIMO NU-OTFS radar. Section 6.3 describes the experimental approach used and discusses the results from the experimental campaigns. A chapter summary is presented in Section 6.4.

6.2. NU-OTFS MIMO RADAR

Consider a MIMO OTFS radar system transmitting a message $\mathbf{X}_{\mathrm{DD}}^{\mathrm{MIMO}} \in \mathbb{C}^{N\times M}$ defined in a $N \times M$ delay-Doppler grid, with N delay bins and M Doppler bins, in which the delay-Doppler messages associated to each transmitter are arranged as shown in Fig. 6.1. A mapping between $\mathbf{X}_{\mathrm{DD}}$ and a TF representation with a quasi-arbitrary TF occupancy pattern can be achieved via the non-uniform inverse symplectic finite Fourier transform (NU-ISFFT) [70]. For transmitter n_{Tx}

$$\mathbf{X}_{\mathrm{TF}}^{(n_{\mathrm{Tx}})} = \mathbf{\Xi}_{N}^{(n_{\mathrm{Tx}})} \mathbf{F}_{N} \mathbf{X}_{\mathrm{DD}}^{(n_{\mathrm{Tx}})} \mathbf{F}_{M}^{\mathrm{H}} \mathbf{\Xi}_{M}^{(n_{\mathrm{Tx}})} \tag{6.1}$$

where $\mathbf{F}_{\mathrm{N}} \in \mathbb{C}^{N\times N}$ and $\mathbf{F}_{\mathrm{M}} \in \mathbb{C}^{M\times M}$ are normalized Fourier transform matrices, and $\mathbf{\Xi}_{N}^{(n_{\mathrm{Tx}})}$ and $\mathbf{\Xi}_{M}^{(n_{\mathrm{Tx}})}$ are diagonal matrices indexing the active subcarriers and

subsymbols respectively. $\mathbf{X}_{\mathrm{TF}}^{(n_{\mathrm{Tx}})} \in \mathbb{C}^{N\times M}$ is the sparse time-frequency representation of the signal associated with the n_{Tx}-th transmitter, as depicted in Fig. 6.1c. The Heisenberg transform converts the TF signal into the time domain for transmission:

$$\mathbf{s}^{(n_{\mathrm{Tx}})} = \mathrm{vec}\left(\mathbf{F}_{\mathrm{N}}^{\mathrm{H}}\mathbf{X}_{\mathrm{TF}}^{(n_{\mathrm{Tx}})}\right) \tag{6.2}$$

The discrete time-domain signal $\mathbf{s} \in \mathbb{C}^{NM\times 1}$ is transformed to the analog domain with a digital-to-analog converter (DAC) before undergoing I/Q modulation to the desired carrier frequency. Equations (6.1) and (6.2) are for the general MIMO case. In this chapter, we use the same formulation to separate polarimetric channels, using the non-uniform TF representations to separate the transmission of V and H polarizations. The received signal after illuminating a scene with K targets characterized by a path delay τ and Doppler shift f_d can be written as

$$\begin{aligned} r_V(t) = \sum_{k=1}^{K} &\left(\alpha_{\mathrm{VV},k}\, s_V(t-\tau_k) + \alpha_{\mathrm{HV},k}\, s_H(t-\tau_k)\right) \\ &\exp\left(j2\pi f_{d,k}\, t\right) + w_V \end{aligned} \tag{6.3}$$

$$\begin{aligned} r_H(t) = \sum_{k=1}^{K} &\left(\alpha_{\mathrm{HH},k}\, s_H(t-\tau_k) + \alpha_{\mathrm{VH},k}\, s_V(t-\tau_k)\right) \\ &\exp\left(j2\pi f_{d,k}\, t\right) + w_H \end{aligned} \tag{6.4}$$

where $s_V(t)$ and $s_H(t)$ are the transmitted time signals in the vertical and horizontal polarization channels, respectively, and α is the complex amplitude associated with the target for each polarimetric channel; w is additive white Gaussian noise. The TF representation of the signal for the vertically polarized receiver after sampling is given by

$$\mathbf{Y}_{\mathrm{TF}}^{(\mathrm{V})} = \mathbf{F}_{\mathrm{N}}\mathrm{vec}_{N\times M}^{-1}\mathbf{r}_V \tag{6.5}$$

Each transmitted signal -polarimetric channel in this case- can now be separated in the receivers using the known time-frequency patterns; e.g., the VV (co-polar) and HV (cross-polar) channels can be extracted by

$$\mathbf{Y}_{\mathrm{TF}}^{(\mathrm{VV})} = \mathbf{\Xi}_N^{(\mathrm{V})}\mathbf{Y}_{\mathrm{TF}}^{(\mathrm{V})}\mathbf{\Xi}_M^{(\mathrm{V})} \tag{6.6}$$

$$\mathbf{Y}_{\mathrm{TF}}^{(\mathrm{HV})} = \mathbf{\Xi}_N^{(\mathrm{H})}\mathbf{Y}_{\mathrm{TF}}^{(\mathrm{V})}\mathbf{\Xi}_M^{(\mathrm{H})} \tag{6.7}$$

respectively, thus retrieving the signal associated to the n_{Tx} transmitter, and completing the polarimetric implementation of NU-OTFS. Superscripts in $\mathbf{\Xi}_N^{(\mathrm{V})}$ and $\mathbf{\Xi}_M^{(\mathrm{H})}$ have been changed w.r.t. (6.1) to reflect the polarization of the signals. HH and HV components can be extracted analogously to (6.5) - (6.7).

For range-Doppler estimation, the radar receiver based on the phase normalization in the time-frequency domain is used for radar estimation. The implementation (e.g., to extract the HV channel) involves a symbol-wise phase normalisation

$$\mathbf{Y}_{\mathrm{div}}^{(\mathrm{VV})}[n,m] = \mathbf{Y}^{\mathrm{V}}[n,m]\exp\left(-j\Psi^{\mathrm{H}}[n,m]\right) \tag{6.8}$$

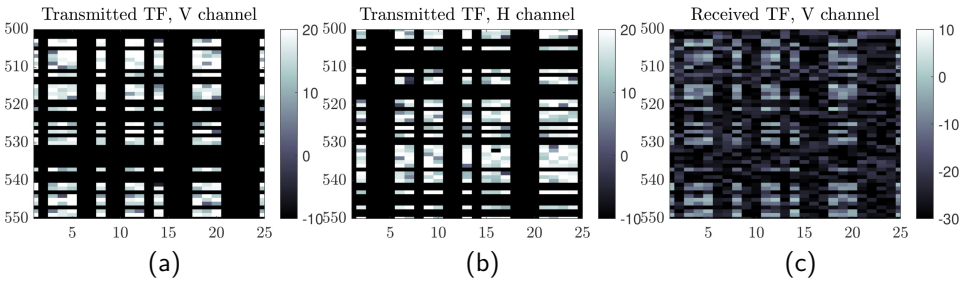

Figure 6.2: Slices of transmitted and received signals in the time-frequency domain: (a) and (b) show the transmitted signals in the V and H channels, respectively, and (c) shows the received signal in the V channel, with some cross-polar components.

where

$$\Psi^{\mathrm{H}}[n,m] = \angle(\mathbf{X}^{\mathrm{H}}_{\mathrm{TF}}[n,m]). \tag{6.9}$$

After spectral division, the SFFT is performed to extract the delay-Doppler map. This estimation approach can be used jointly with non-uniform multiplexing and a repeat CP-OTFS structure to maintain the full unambiguous parameter estimation at low computational complexity [72].

6.3. EXPERIMENTAL VALIDATION

This section presents experimental results of NU-OTFS polarimetric radar to validate the MIMO principle of channel separability. The data are gathered using the PARSAX radar [91], a polarimetric weather radar. The system and measured scenario is the same as the one used in Chapter 4, Fig. 4.9. Two NU-OTFS waveforms with non-overlapping time-frequency representations are sent simultaneously in two orthogonally polarized Tx channels and received in two polarimetric receivers. With this setup, the received signal for a given polarization can be filtered using the known transmit patterns. The objective is to extract the full polarimetric matrix of the target with a single frame measurement, which would verify the MIMO capabilities of the proposed waveform. In this test, polarization takes the role of spatial diversity in what would be a more traditional MIMO radar system. The waveform parameters are shown in Table 6.1. The received signal is filtered using the known transmit matrices, and range and Doppler are estimated through standard DFT processing and the Orthogonal Matching Pursuit (OMP) sparse reconstruction algorithm.

6.3.1. RESULTS

As the main goal of this study is to validate the MIMO capabilities and channel separability of simultaneous transmission of NU-OTFS waveforms, we focus not only on the radar estimation but also on the visualization of the transmit and receive signals in different points of the system. A crop of the time-frequency

Table 6.1: OTFS measurement waveform parameters

Parameter	Symbol	Value
Number of delay bins	N	1024
Number of Doppler bins	M	26
Bandwidth	B	40 MHz
Carrier frequency	f_c	3.315 GHz
Symbol duration	T	25.6 μs
Intercarrier separation	Δf	39.06 kHz
Cyclic prefix duration	T_{cp}	12.8 μs
Communication Modulation	(–)	QPSK

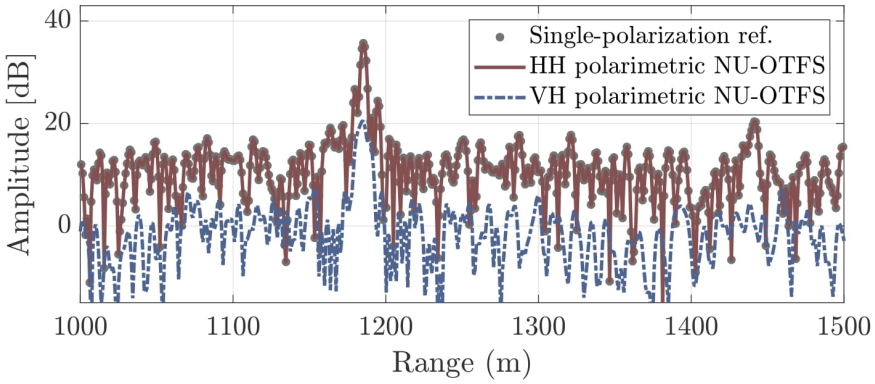

Figure 6.3: Zero-Doppler cut of the range-Doppler estimation in the V channel for the HH and VH components. Both components can be separated as they appear in non-overlapping time-frequency patterns, and the HH component matches with the non-polarimetric measurement, indicating good separability in the time-frequency domain.

representation of the transmit signals sampled directly at IF is shown in Fig. 6.2. Specifically, Figs. 6.2a and 6.2b show that the time-frequency patterns of the signals are cleanly maintained regardless of any possible system distortion, and they occupy non-overlapping time-frequency resources in their baseband representation. Assuming that the signal is well designed in terms of cyclic-prefix length and subcarrier separation for a given channel, this indicates that different MIMO transmitters or users in a multi-user (MU) MIMO communications scenario can be separated by knowing the time-frequency occupancy pattern. Finally, Fig. 6.2c shows the same time-frequency crop of the received signal after channel propagation in the V channel. Here, the pattern of the transmitted V signal can still be identified, but power appears outside of it as well due to the cross-polar components of the target signature.

The radar range-Doppler estimation is performed for both channels to verify the

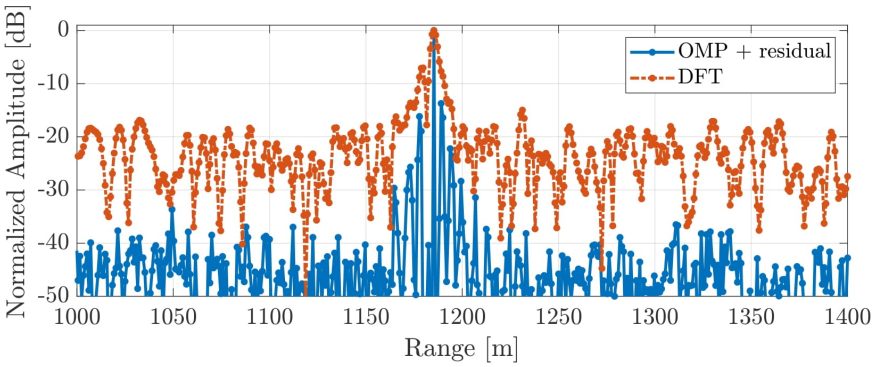

Figure 6.4: DFT and OMP-based range estimation. High sidelobes can be partially mitigated with the use of OMP or other similar algorithms.

Table 6.2: RCS difference between pol. and non-pol. measurements

Waveform	VV	VH	HV	HH
1D NU-OTFS	0.003 dB	0.01 dB	0.04 dB	0.01 dB
2D NU-OTFS	0.01 dB	0.1 dB	0.1 dB	0.001 dB

presence of the co-polar and cross-polar components in the expected time-frequency indexes of the received baseband signal. Fig. 6.3 shows the zero-Doppler cut of the range-Doppler estimation for both HH and VH components. The chimney can be seen as the main target at approximately 1185 meters in both co-polar and cross-polar channels, indicating that the received signal remains in the expected time-frequency resources, as otherwise the spectral division in (6.8) with a misaligned reference signal would impair the estimation and render the target invisible. Moreover, the polarimetric estimation closely matches the result of a horizontally polarized reference measurement, indicating no interference between channels in the TF representation. It is also apparent in Fig. 6.3 that the sidelobe level is quite high due to the non-uniform sampling in the time-frequency domain. A possible solution to increase the system's dynamic range is to use sparse reconstruction algorithms from the compressed sensing framework. In Fig. 6.4, we show the result of applying the orthogonal matching pursuit (OMP) algorithm on range estimation, showing a dynamic range improvement of around 20 dB with measured data, although some artifacts appear close to the main target, which extended target characteristics of the chimney could explain. Table 6.2 shows the RCS difference between single-polarized references and all the polarimetric measurements for both random frequency (1D NU-OTFS) and time-frequency (2D NU-OTFS) allocations. The results are all below 0.1 dB, a difference that can be attributed to the randomness in different noise realizations.

Finally, the range-Doppler estimation around the target is shown in Figs. 6.5 and 6.6, in which we can observe two things: First, in each of them, we can see the

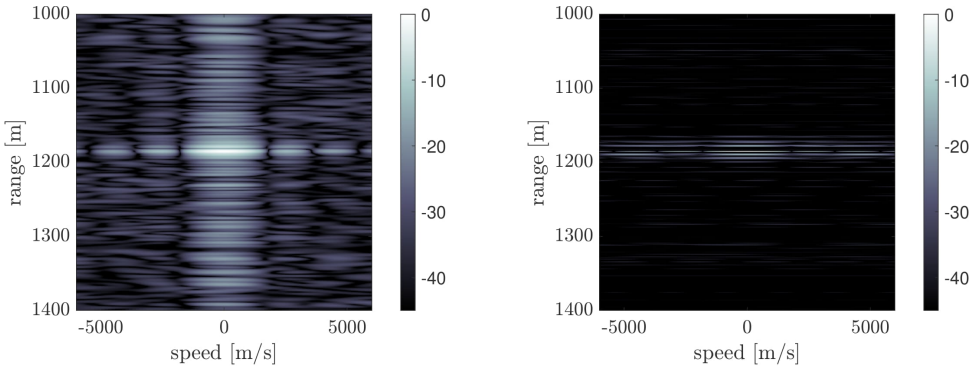

Figure 6.5: Range-Doppler estimation crop around the target for non-uniform intercarrier allocation. On the left, 2D-DFT processing. On the right, OMP is used for range estimation prior to Doppler estimation.

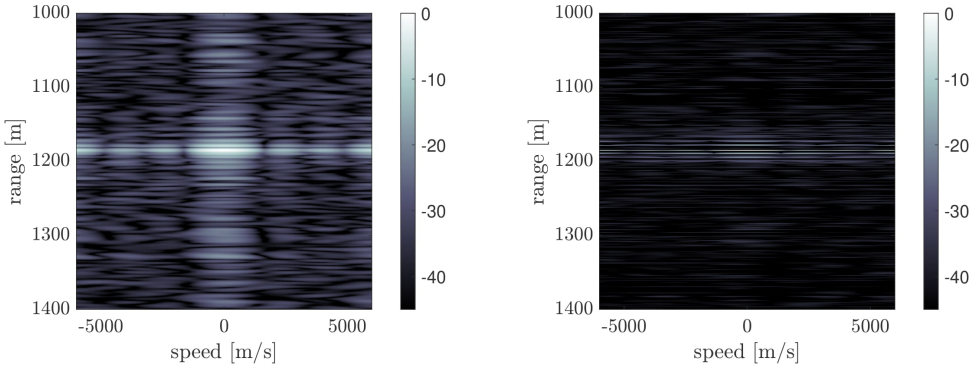

Figure 6.6: Range-Doppler estimation crop around the target for non-uniform 2D time-frequency allocation. On the left, 2D-DFT processing. On the right, OMP is used for range estimation prior to Doppler estimation.

effect of applying OMP for range estimation before Doppler estimation, resulting in a considerably reduced sidelobe level outside the Doppler cut of the target, reducing the likelihood of the target masking other targets at different distances. Second, they serve to validate both 1D subcarrier non-uniform multiplexing (Fig. 6.5) and 2D non-uniform subcarrier-subsymbol multiplexing (Fig. 6.6).

6.4. CONCLUSIONS

This chapter has presented the first over-the-air polarimetric demonstration of MIMO NU-OTFS in a real polarimetric radar system. By performing radar

estimation of the polarimetric channels transmitted simultaneously and analyzing the physical signal at different steps within the system, we confirmed the separability and low cross-transmitter interference of non-overlapping random time-frequency multiplexing with NU-OTFS. These findings prove that MIMO NU-OTFS can sustain reliable sensing while using fragmented spectral masks without meaningful self-interference, thereby opening a practical path toward ISAC architectures that exploit non-uniform time-frequency sampling in high-mobility scenarios.

7

CONSTANT MODULUS OTFS

"I never trust people with no appetite. It's like they're always holding something back on you."
— Haruki Murakami

In this chapter, the problem of amplifier-related signal amplitude compression in the OTFS waveform for radar and communications systems is investigated. A novel approach to OTFS waveform generation is proposed, where complementary sequences are used with the Zak transform to encode delay-Doppler symbols and form an OTFS time-domain signal with a constant envelope. The high PAPR of conventional OTFS can cause amplifier saturation, leading to spectral noise and performance degradation in both communication and radar systems due to amplitude clipping. This issue can be critical in dual-function radar and communication applications, where high power may be crucial in both use cases. The proposed waveform, namely constant modulus OTFS (CM-OTFS), offers an alternative to standard OTFS when high-power or low-cost amplification is required. The sensing and communications performances of CM-OTFS are evaluated through numerical simulations and compared with pristine and amplifier-distorted OTFS waveforms. CM-OTFS demonstrates slightly degraded sensing performance and lower communication rate than pristine OTFS, but outperforms amplifier-distorted OTFS signals. The performance of CM-OTFS is evaluated through radar and communication simulations, as well as radar measurements using the waveform-agile PARSAX radar.

Parts of this chapter have been published in [98]

7.1. INTRODUCTION

In previous chapters, we have demonstrated that OTFS shows comparable flexibility in terms of time and frequency usage to accommodate multiple communication users or radar transmitters and avoid interference in both the time-frequency [70], [94] [69] and spatial [99] domains. Another characteristic that OTFS shares with OFDM, however, is a peak-to-average power ratio (PAPR) greater than one [26], meaning that the envelope of the transmitted time-domain signal is not constant amplitude. The expected PAPR of OFDM increases with the number of subcarriers (fast-time radar samples) [100] in the transmitted signal. In contrast, in OTFS, the expected PAPR increases with the number of subsymbols [26] transmitted over slow-time in one radar frame. Regardless of the different parameter dependence, a non-uniform envelope requires the use of highly linear power amplifiers in the transmitter to avoid signal distortion that would impact both radar and communication performance [101]. This issue is particularly relevant to radar and joint radar and communications applications, where high power is crucial due to the attenuation of round-trip wave propagation. Considering the potential of OTFS for ISAC applications, this is a significant drawback.

Several approaches have been investigated to minimize the PAPR in OFDM signals. An iterative technique was proposed in [102] to reduce the PAPR, resulting in a signal spread across a greater frequency bandwidth. Convex optimization is used in [103] to design low PAPR waveforms for an ISAC base station dividing OFDM subcarriers between remote sensing and communications applications. This technique is suitable for generating signals with spectral nulls but not for real-time implementation in adaptive systems due to the high computational load. Another alternative is to use the so-called constant-envelope OFDM [37]. However, constant-envelope OFDM signaling presents several challenges related to phase-only information encoding. No similar approaches have been proposed for OTFS, although it is reasonable to assume that some of them can be adapted to the waveform, given their similarities.

In this chapter, we propose a method to form unit-PAPR OTFS frames based on generating complementary sequences from the information data to be transmitted. The proposed approach is inspired by the work in [104],[105], [38], where a similar technique is applied to achieve constant-modulus OFDM (CM-OFDM). The approach in [104] is reformulated to fit the Zak transform-based implementation of OTFS, where the delay-Doppler message is directly transformed into the time-domain signal without an intermediate time-frequency representation. Specifically, the main contributions of this chapter are the following:

1. A formulation for the Zak transform-based constant-modulus OTFS (CM-OTFS) signal. For each subcarrier, two complementary sequences are built from the slow-time symbols of the OTFS frame in an iterative process, resulting in a final constant-envelope time-domain signal. Double differential encoding (DDE) and decoding are used to deal with cumulative phase errors during CM-OTFS symbol recovery, as proposed for CM-OFDM in [38]. Radar and communication receivers compatible with the proposed CM-OTFS waveform are presented, completing the concept for an ISAC CM-OTFS system.

2. A simulation-based and experimental evaluation of the performance of the proposed CM-OTFS waveform for monostatic SISO radar applications. The performance is compared with standard OTFS under non-linear amplifier-induced signal distortion.

3. A simulation-based study of the communications performance of constant-modulus OTFS. A numerical comparison with standard OTFS under amplifier distortion is drawn using standard 3GPP vehicular channel models for simulation.

The scope of this chapter is limited to single-user scenarios, and extension of the technique proposed to the MIMO radar and multi-user scenarios using beamspace [99], delay-Doppler [69], and time-frequency [70] multiplexing is a subject of future research. The remainder of the chapter is structured as follows. Section 1 recalls a mathematical description of OTFS signal generation and channel effects, discusses the issue of PAPR in OTFS waveforms, and presents the CM-OTFS signal generation method. Section 2 includes descriptions of the CM-OTFS radar signal model and receiver. Section 3 presents numerical radar and communications performance simulations for the proposed CM-OTFS system concept, and Section 4 extends these results with experimental validation for CM-OTFS radar. Finally, concluding remarks are given in section 5.

Notation: In this chapter, the presence of related pairs of vectors lead to a slight change in vector notation: vector parameter dependencies are indicated by $\mathbf{a}(n)$, individual components by $a[m]$, and subscripts distinguish related vectors, e.g., the complementary sequence pair $\mathbf{c}_1$ and $\mathbf{c}_2$.

7.2. OTFS ISAC SYSTEM MODEL

Consider a single transmitter OTFS system transmitting a message $\mathbf{X}_{\text{DD}} \in \mathbb{C}^{N\times M}$ defined in a $N \times M$ delay-Doppler grid, with N delay bins and M Doppler bins. The number of subcarriers and subsymbols in time-frequency representation is also N and M, respectively, and the communication symbols are mapped to the time-frequency domain through the inverse symplectic Fourier transform (ISFFT)

$$\mathbf{X}_{\text{TF}}[n,m] = \frac{1}{\sqrt{NM}} \sum_{k=0}^{N-1} \sum_{l=0}^{M-1} \mathbf{X}_{\text{DD}}[k,l] e^{j2\pi\left(\frac{ml}{M} - \frac{nk}{N}\right)} \tag{7.1}$$

where $[k,l]$ are index pairs in the delay-Doppler grid, and $[n,m]$ are index pairs in the slow-time-frequency grid. The Heisenberg transform converts the time-frequency signal into the time domain for transmission. The time domain signal $s(t)$ is given by

$$s(t) = \sum_{n=0}^{N-1} \sum_{m=0}^{M-1} \mathbf{X}_{\text{TF}}[n,m] g_{tx}(t-nT) e^{j2\pi n\Delta\text{f}(t-mT)} \tag{7.2}$$

where g_{tx} is the transmit pulse. Assuming a rectangular transmit pulse and a critically sampled signal, equations (7.1) and (7.2) can be written in compact matrix notation as

$$\mathbf{X}_{\text{TF}} = \mathbf{F}_{\text{N}} \mathbf{X}_{\text{DD}} \mathbf{F}_{\text{M}}^{\text{H}} \tag{7.3}$$

and

$$\mathbf{s} = \mathrm{vec}\left(\mathbf{F}_{\mathrm{N}}^{\mathrm{H}}\mathbf{X}_{\mathrm{TF}}\right) = \mathrm{vec}\left(\mathbf{X}_{\mathrm{DD}}\mathbf{F}_{\mathrm{M}}^{\mathrm{H}}\right) \tag{7.4}$$

where $\mathbf{F}_{\mathrm{N}} \in \mathbb{C}^{N\times N}$ and $\mathbf{F}_{\mathrm{M}} \in \mathbb{C}^{M\times M}$ are normalized Fourier transform matrices. The discrete time-domain signal $\mathbf{s} \in \mathbb{C}^{NM\times 1}$ is transformed to the analog domain with a digital-to-analog converter (DAC) before undergoing I/Q modulation and up-mixing to the desired carrier frequency f_c. Note that in (7.4), a single discrete Fourier transform is used to map the delay-Doppler domain symbols to the time-domain signal. This transform is referred to as the Zak transform and allows for the synthesis of the OTFS time-domain signal without an intermediate time-frequency representation.

7.2.1. PAPR IN OTFS SIGNALS

A single DFT across the Doppler symbols is required to go from the delay-Doppler representation ($\mathbf{X}_{\mathrm{DD}}$) to the time-domain transmitted signal $\mathbf{s}$, as shown in (7.4). This is the Zak transform, and it is the reason why the expected PAPR of OTFS increases with M [26]. The PAPR of a specific OTFS frame depends on the transmitted message and is, therefore, best modeled as a random variable, assuming that the probability of different messages is uniform for any given frame. The complementary cumulative probability distribution functions of the PAPR in an OTFS signal for different values of M are shown in Fig. 7.1, showcasing the dependency with the number of subsymbols, as well as the expected PAPR values in realistic OTFS frames for QPSK modulation. We refer the reader to [26] for a deeper study on the PAPR of OTFS with a variety symbol constellations and frame sizes.

The increase in PAPR can lead to radar performance degradation if the signal is transmitted through a saturated amplifier. Amplifier saturation is common in radar systems to maximize output power and increase target detection probability. In this work, the power amplifier is modeled as an instantaneous nonlinearity [106]. Considering as input an arbitrary complex signal

$$s_{in}(t) = A_{in}(t)\exp\left(j\phi_{in}(t)\right) \tag{7.5}$$

and the output

$$s_{out}(t) = G(A_{in}(t))\exp\left(j(\phi_{in}(t) + \Phi(A_{in}(t))\right) \tag{7.6}$$

where G and Φ are input-amplitude dependent distortions of the amplitude (clipping) and phase of the output signal, respectively. We use the model from [107], [37]:

$$G(A_{in}(t)) = \frac{g_0 A_{in}(t)}{1 + (A_{in}(t)/A_{sat,in})^2} \tag{7.7}$$

$$\Phi(A_{in}(t)) = \frac{\alpha_\phi A_{in}^2(t)}{1 + \beta_\phi A_{in}^2(t)} \tag{7.8}$$

which is parametrized by the gain g_0, the input saturation amplitude $A_{sat,in}$, and the amplitude-dependent phase modulation α_ϕ and β_ϕ, which we set to $\alpha_\phi = \pi/6$

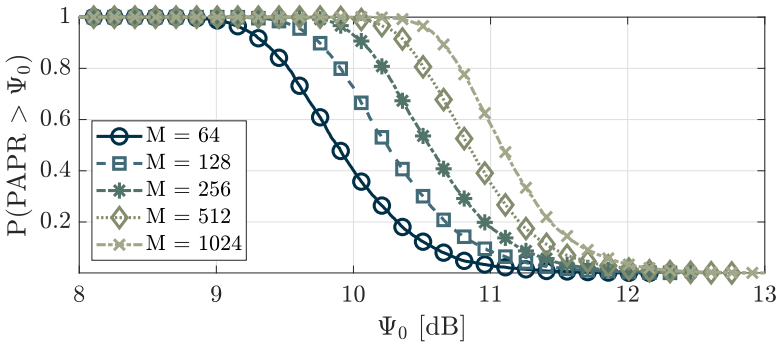

Figure 7.1: Complementary cumulative distribution function (CCDF) of PAPR in OTFS signals for different values of M, numerically calculated with 5000 simulations for each data point. In all examples, $N = 256$.

and $\beta_\phi = 0.2$. Finally, amplitude clipping is defined by the value of $A_{sat,in}$, which is set by the PAPR of the signal and the input power backoff (IBO) [108], defined as

$$\text{IBO} := \frac{A_{sat,in}}{\mathbb{E}(A_{in}^2(t))} \geq 1 \tag{7.9}$$

For any constant envelope signal, such as the CM-OTFS presented in this work, the IBO = 0 dB. The lower the value of IBO for a non-constant envelope signal, the stronger the amplitude clipping in the output signal. The effect of amplitude clipping in the time-domain signal is depicted in Fig. 7.2. Integrated and peak sidelobe levels in the radar range-Doppler estimation for different levels of amplifier distortion (parametrized with the IBO) are shown in Fig. 7.3, where a loss of almost 10 dB in dynamic range occurs for low IBO values. The envelope variation of time domain OTFS arises from the Doppler domain symbol integration through the Zak transform, and it can lead to the distortion shown in Fig. 7.2 and the sidelobe level increase shown in Fig. 7.3. However, it is possible to use the Zak transform to formulate a constant-modulus version of OTFS signals using complementary sequences generated from the transmitted symbols in the Doppler domain.

7.2.2. Constant Modulus OTFS

Let us consider the same delay-Doppler message $\mathbf{X}_{\text{DD}} \in \mathbb{C}^{N\times M}$ from the previous section as formed by N data vectors $\mathbf{a}(n) \in \mathbb{C}^{1\times M}\ \forall\ n \in [1, N]$, such that

$$\mathbf{X}_{\text{DD}} = [\mathbf{a}(1)^T, \mathbf{a}(2)^T, \ldots, \mathbf{a}(N)^T]^T. \tag{7.10}$$

A pair of complementary sequences $\mathbf{c}_1$ and $\mathbf{c}_2$ are built from each data vector $\mathbf{a}(n) \in \mathbb{C}^{1\times M}$, where n denotes the delay index in the delay-Doppler representation of the OTFS signal. The sequence pair $\mathbf{c}_1$ and $\mathbf{c}_2$ are complementary when the sum of their autocorrelations $\mathbf{r}_{11}$ and $\mathbf{r}_{22}$ add up to a δ-function

$$\mathbf{r}_{11} + \mathbf{r}_{22} \propto \delta[\eta] \tag{7.11}$$

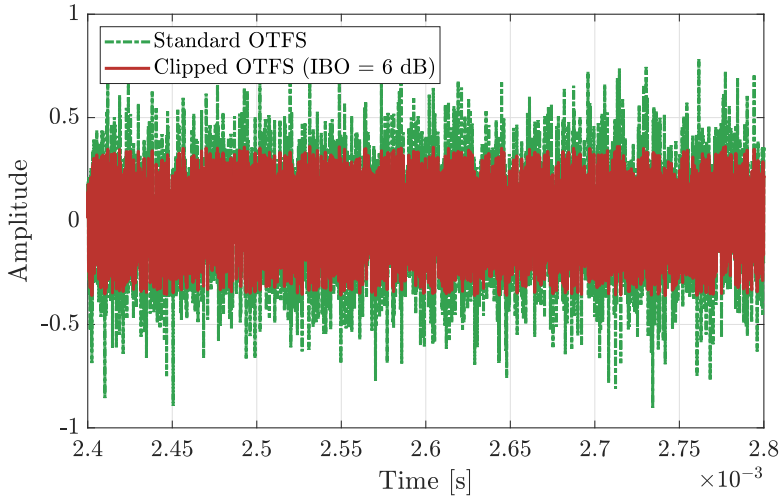

Figure 7.2: Real part of a standard OTFS signal, and the same signal with amplifier-related amplitude clipping.

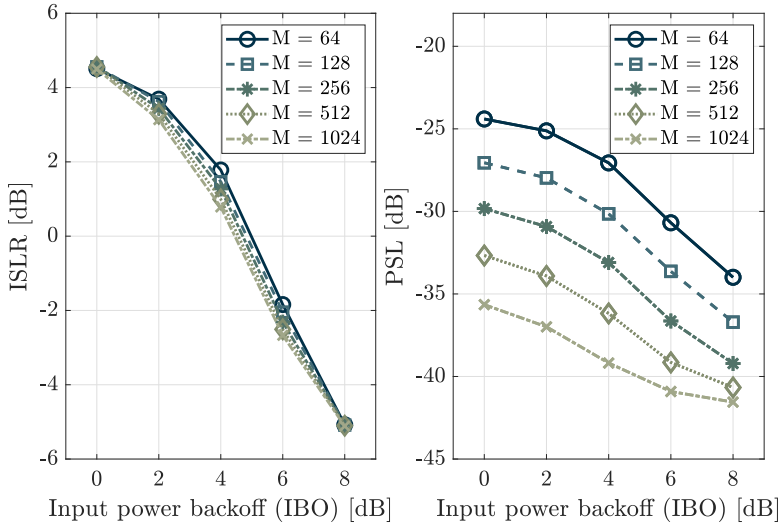

Figure 7.3: Integrated and peak sidelobe levels of a range-Doppler estimation in a distorted OTFS frame for different values of M and IBO. Lower values of IBO represent a higher degree of amplitude distortion.

Following Algorithm 1, an initial pair of Golay sequences $\mathbf{c}_1^{(-1)}$ and $\mathbf{c}_2^{(-1)}$ are iteratively extended into longer sequences through 2×2 unitary transforms using the data symbols contained in $\mathbf{a}(n)$. Let us define the initial sequences as

$$\mathbf{c}_1^{(-1)} := [1,1], \quad \mathbf{c}_2^{(-1)} := [1,-1]. \tag{7.12}$$

Algorithm 1 CM-OTFS Complementary Sequence Generation

Input: Data vectors $\mathbf{a}(n)$, M Doppler bins, N delay bins, coupling parameter r
Output: Complementary sequences $\mathbf{c}_1^{(M)}$, $\mathbf{c}_2^{(M)}$
begin
  Initialization: $\mathbf{c}_1^{(-1)} := [1,1]$, $\mathbf{c}_2^{(-1)} := [1,-1]$ (See Eq. (7.12))
  Compute normalization factor $\alpha = 1/\sqrt{\mathbb{E}[||\mathbf{a}||^2] + r^2}$
for $n = 1$ to N **do**
  for $m = 0$ to $M-1$ **do**
    1. Compute unitary transform matrix:
      Define $\mathbf{S}_m$ as in Eq. (7.13)
    2. Expand complementary sequences:
      Update $\mathbf{c}_1^{(m)}$, $\mathbf{c}_2^{(m)}$ as in Eq. (7.14)
  end for
    3. Form $\mathbf{d}_1(n)$, $\mathbf{d}_2(n)$ as in Eq. (7.15), (7.16)
end for
end

For the data vector $\mathbf{a}(n)$ associated with a specific subcarrier n, this sequence is extended by one symbol at a time through an M-long iterative process of unitary transforms defined as

$$\mathbf{S}_m = \alpha \begin{bmatrix} a[m] & -r \\ r & a^*[m] \end{bmatrix} \tag{7.13}$$

where $a[m]$ is the m-th symbol from the data vector $\mathbf{a}(n)$, r is a free parameter that determines coupling between the complementary sequences, and $\alpha = 1/\sqrt{\mathbb{E}[||\mathbf{a}||^2] + r^2}$ is a normalization factor. Note that we drop writing explicitly the dependency with n for compactness and clarity. In CM-OFDM, the value of r has been shown to impact communication and radar performance in opposing ways, making it a trade-off parameter [104]. The influence of the r-value in CM-OTFS will be analyzed empirically in subsequent sections.

The transforms are used to expand the pair of complementary sequences iteratively

$$\begin{bmatrix} \mathbf{c}_1^{(m)} \\ \mathbf{c}_2^{(m)} \end{bmatrix} = \mathbf{S}_m \begin{bmatrix} \mathbf{c}_1^{(m-1)} & 0 \\ 0 & \mathbf{c}_2^{(m-1)} \end{bmatrix} \tag{7.14}$$

which generates two complementary sequences $\{\mathbf{c}_1^{(m)}, \mathbf{c}_2^{(m)}\}$. The iterative sequence expansion in (7.14) results in two expanded sequences $\{\mathbf{c}_1, \mathbf{c}_2\} \in \mathbb{C}^{1\times M'}$, where we use $M' := M+2$ for compactness of notation. Mirroring the steps in [109] for CM-OFDM, the resulting sequences are interleaved to form a new pair of complementary sequences $\mathbf{d}_1$, $\mathbf{d}_2 \in \mathbb{C}^{1\times 2M'}$

$$\mathbf{d}_1 = [c_1[0], c_2[0], c_1[1], c_2[1], \ldots, c_2[M+1]] \tag{7.15}$$

$$\mathbf{d}_2 = [c_1[0], -c_2[0], c_1[1], -c_2[1], \ldots, -c_2[M+1]] \tag{7.16}$$

that will be used to assemble the OTFS time signal with the Zak transform. For N delay bins, the process in (7.13-7.16) is repeated for each vector $\mathbf{a}(n)$, resulting in

N pair of sequences, indexed as $\{\mathbf{d}_1(n), \mathbf{d}_2(n)\}\ \forall\ n \in [1, N]$. Two new delay-Doppler signals composed of these complementary sequences can be written as

$$\hat{\mathbf{X}}_{\mathrm{DD}_1} = [\mathbf{d}_1(1)^T, \mathbf{d}_1(2)^T, \ldots, \mathbf{d}_1(N)^T]^T \tag{7.17}$$

$$\hat{\mathbf{X}}_{\mathrm{DD}_2} = [\mathbf{d}_2(1)^T, \mathbf{d}_2(2)^T, \ldots, \mathbf{d}_2(N)^T]^T \tag{7.18}$$

and finally, two intermediate time-domain signals can be generated as in (7.4) with the Zak transform

$$\mathbf{z}_1 = \mathrm{vec}\left(\hat{\mathbf{X}}_{\mathrm{DD}_1}\mathbf{F}_{\mathrm{M}}^{\mathrm{H}}\right) \tag{7.19}$$

$$\mathbf{z}_2 = \mathrm{vec}\left(\hat{\mathbf{X}}_{\mathrm{DD}_2}\mathbf{F}_{\mathrm{M}}^{\mathrm{H}}\right) \tag{7.20}$$

where each $\mathbf{z}_1$ and $\mathbf{z}_2$ are OTFS sub-signals of length $2NM'$, and are used to construct the final OTFS constant-modulus time-domain signals

$$\hat{\mathbf{s}}_1 = \mathbf{z}_1 + j\exp(j\boldsymbol{\phi}_c) \odot \mathbf{z}_2 \tag{7.21}$$

$$\hat{\mathbf{s}}_2 = \mathbf{z}_1 - j\exp(j\boldsymbol{\phi}_c) \odot \mathbf{z}_2 \tag{7.22}$$

where $\{\hat{\mathbf{s}}_1, \hat{\mathbf{s}}_2\} \in \mathbb{C}^{1\times 2M'}$, and $\boldsymbol{\phi}_c = \angle\mathbf{z}_1 - \angle\mathbf{z}_2 \in \mathbb{R}^{1\times 2M'}$. In (7.21) and (7.22), the phase of $\mathbf{z}_2$ is replaced with the phase of $\mathbf{z}_1$ and placed in quadrature, which results in a constant modulus OTFS time-domain signal. Signals $\hat{\mathbf{s}}_1$ and $\hat{\mathbf{s}}_2$ are both transmitted (e.g., in consecutive delay bins or as double-length Doppler messages) to use differential decoding to avoid errors in the process of recovering the data vectors $\mathbf{a}(n)$. This reflects the main trade-off of both CM-OFDM and the proposed CM-OTFS when using this constant-modulus formulation: $4M$ total symbols are transmitted to encode a total of M data symbols, reducing the efficiency by a factor of four.

The process generates two complementary sequences from the communication symbols and uses the Zak transform to synthesize the OTFS time-domain signal, replacing the operation in (7.4). For N delay indexes of the original $\mathbf{X}_{\mathrm{DD}}$ data matrix, the resulting time-domain signal is

$$\mathbf{s}_{\mathrm{CM}} = \mathrm{vec}\,(\mathbf{S}_{\mathrm{CM}}) \tag{7.23}$$

where $\mathbf{S}_{\mathrm{CM}} \in \mathbb{C}^{2N\times 2M}$ is defined as

$$\mathbf{S}_{\mathrm{CM}} = [\hat{\mathbf{s}}_1^T(n=1), \hat{\mathbf{s}}_2^T(n=1), \ldots, \hat{\mathbf{s}}_1^T(n=N), \hat{\mathbf{s}}_2^T(n=N)]^T \tag{7.24}$$

which has a constant-envelope as shown in Fig. 7.4 and encodes $N \times M$ communications symbols in a $2N \times 2M'$ frame.

Before moving forward, it is worth discussing some already apparent drawbacks. First, there is a reduction in spectral efficiency, as a frame of size $4NM'$ is used to encode NM QPSK delay-Doppler symbols, which corresponds to a reduction by a factor of four. Moreover, this approach to generate a constant-modulus signal has only been defined for communication dictionaries without amplitude modulation, restricting this approach to QPSK and phase-only dictionaries [109].

To recover the delay-Doppler symbols $\mathbf{a}(n)$, the previous process is undone. Let us assume a received signal $\mathbf{r}_{\mathrm{CM}} \in \mathbb{C}^{4NM'\times 1}$ after channel compensation

$$\mathbf{r}_{\mathrm{CM}} = \mathbf{s}_{\mathrm{CM}} + \mathbf{w} \tag{7.25}$$

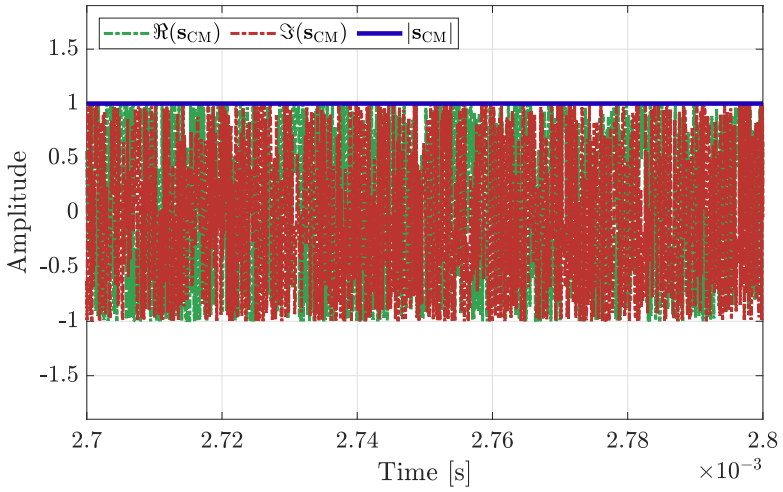

Figure 7.4: Real and imaginary part resulting from the CM-OTFS process, using the same data symbols as in the signal depicted in Fig. 7.2. The amplitude of the signal (blue curve) is constant.

Algorithm 2 CM-OFTS Delay-Doppler Symbol Recovery

Input: $\hat{\mathbf{Y}}_{\mathrm{DD}_1}, \hat{\mathbf{Y}}_{\mathrm{DD}_2}, r, M, N, \hat{\mathbf{c}}_1^{(0)}, \hat{\mathbf{c}}_2^{(0)}$
Output: $\hat{\mathbf{a}}(n) \in \mathbb{C}^{1\times M} \quad \forall n \in [1, N]$
begin
  Initialization: $\hat{\mathbf{a}}(n) = \mathbf{0} \quad \forall n \in [1, N]$;
for $n = 1$ to N **do**
  for $m = 0$ to $M-1$ **do**
    1. Calculate $\hat{\mathbf{a}}(n)_{M-m}$ **data symbol** (7.30);
    2. Update complementary sequences:
      $\mathbf{c}_1^{(m+1)}$ from $\hat{a}[M-m]$ and $\mathbf{c}_1^{(m)}$ (7.31);
      $\mathbf{c}_2^{(m+1)}$ from $\hat{a}[M-m]$ and $\mathbf{c}_2^{(m)}$ (7.32);
  end for
end for
end

where $\mathbf{w}$ is additive white Gaussian noise. If we consider $\mathbf{R}_{\mathrm{CM}} = \mathrm{vec}(\mathbf{r}_{\mathrm{CM}})^{-1}_{2N\times 2M'}$, then $\{\hat{\mathbf{s}}_1(n), \hat{\mathbf{s}}_2(n)\}$ can be recovered by selecting the odd and even rows of $\mathbf{R}_{\mathrm{CM}}$ respectively, undoing the interleaving in (7.24). After some simple algebra we can find that

$$\hat{\mathbf{z}}_1 = \frac{\hat{\mathbf{s}}_1 + \hat{\mathbf{s}}_2}{2} \tag{7.26}$$

$$\hat{\mathbf{z}}_2 = \exp(-j\phi_c)\frac{\hat{\mathbf{s}}_1 - \hat{\mathbf{s}}_2}{2j} \tag{7.27}$$

with which we calculate the delay-Doppler representation of the received signal

$$\hat{\mathbf{Y}}_{\mathrm{DD}_1} = \mathrm{vec}^{-1}_{N\times 2(M+2)}\left(\hat{\mathbf{z}}_1\right)\mathbf{F}_{2\mathrm{M}}, \tag{7.28}$$

$$\hat{\mathbf{Y}}_{\mathrm{DD}_2} = \mathrm{vec}^{-1}_{N\times 2(M+2)}\left(\hat{\mathbf{z}}_2\right)\mathbf{F}_{2\mathrm{M}}, \tag{7.29}$$

from which we can get the estimate of the sequences $\hat{\mathbf{d}}_1$, $\hat{\mathbf{d}}_2$, and $\hat{\mathbf{c}}_1$, $\hat{\mathbf{c}}_1$ by undoing the steps in (7.15-7.18). Finally, from the complementary pairs $\hat{\mathbf{c}}_1$, $\hat{\mathbf{c}}_1$, the original symbols are extracted in an iterative manner that reverses the steps in (7.14), and for each $m \in \{0,\ldots,M-1\}$, as shown in Algorithm 2, where the estimation of the transmitted symbols is given by

$$\hat{a}[M-m] = r\,\frac{\hat{c}_1^{(m)}[1] - \hat{c}_2^{(m)*}[M-m]}{\hat{c}_2^{(m)}[1] + \hat{c}_1^{(m)*}[M-m]} \tag{7.30}$$

and $\{\mathbf{c}_1^{(m+1)}, \mathbf{c}_2^{(m+1)}\}$ for the next iteration are given by the inversion of (7.14) using the conjugate transpose of the Hermitian matrix $\mathbf{S}_m$

$$\mathbf{c}_1^{(m+1)} = \hat{a}[M-m]\hat{\mathbf{c}}_1^{(m)} + r\hat{\mathbf{c}}_2^{(m)} \tag{7.31}$$

$$\mathbf{c}_2^{(m+1)} = -r\hat{\mathbf{c}}_1^{(m)} + \hat{a}[M-m]\hat{\mathbf{c}}_2^{(m)} \tag{7.32}$$

where in each step a new data symbol $\hat{a}[M-m]$ is recovered, and the sequences $\mathbf{c}_1^{(m+1)}$ and $\mathbf{c}_2^{(m+1)}$ have one less length than their predecessors, as their last and first element respectively are zero. Note that the calculation of the sequences $\{\mathbf{c}_1^{(m+1)}, \mathbf{c}_2^{(m+1)}\}$ is performed for each n, but the index is dropped for compactness. This process is repeated for each $n \in \{1,\ldots,N\}$, thus recovering all n data vectors $\hat{\mathbf{a}}(n)$, that forms our received delay-Doppler data matrix

$$\hat{\mathbf{X}}_{\mathrm{DD}} = [\hat{\mathbf{a}}(1)^T, \hat{\mathbf{a}}(2)^T, \ldots, \hat{\mathbf{a}}(N)^T]^T. \tag{7.33}$$

7.3. CONSTANT MODULUS OTFS RADAR

The discrete constant-modulus time-domain signal $\mathbf{s}_{\mathrm{CM}}$ is transformed to the analog domain with a digital-to-analog converter (DAC) before being modulated to the desired carrier frequency and transmitted. Assuming co-located radar operation, the received signal after illuminating a scene with K targets characterized by a path delay τ and a Doppler shift f_d can be written as

$$r(t) = \sum_{k=1}^{K} \alpha_k s_{\mathrm{CM}}(t-\tau_k)\exp\left(j2\pi f_{d,k}t\right) + w \tag{7.34}$$

where $s_{\mathrm{CM}}(t)$ is the transmitted time-domain signal, α_k is the complex amplitude associated to the k-th target, and w is additive white Gaussian noise (AWGN). The delay and Doppler effects in the signal can be represented in the time-frequency domain compactly by using the generalized multicarrier radar signal model [53].

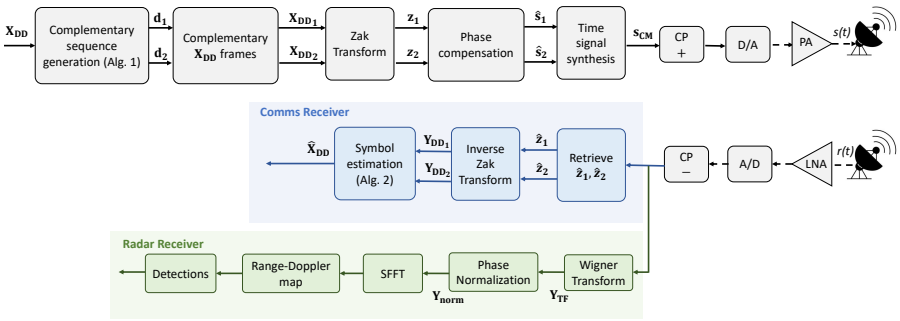

Figure 7.5: Block diagram of an exemplary CM-OTFS ISAC system with dual function waveform transmission. A separate radar and communication digital signal processing chain enables using the complete waveform for both functions. The radar function relies on time-frequency processing, while the communications branch relies on the Zak transform for symbol recovery.

The time-frequency representation $\mathbf{Y}_{\mathrm{TF}} \in \mathbb{C}^{2N\times 2M}$ of the critically sampled received time-domain signal $\mathbf{r}$ is given by

$$\mathbf{Y}_{\mathrm{TF}} = \mathbf{F}_{2\mathrm{N}}\mathrm{vec}^{-1}_{2N\times 2M'}(\mathbf{r}) \tag{7.35}$$

and the radar delay-Doppler effects in the time-frequency signal for each target can be written as

$$\mathbf{r} = \mu\psi\mathrm{vec}(\mathbf{\Gamma_1}\mathbf{F}_{\mathrm{N}}^{\mathbf{H}}\mathbf{A}\mathbf{X}_{\mathrm{TF}}\mathbf{\Gamma_2}) \tag{7.36}$$

where, for a delay τ and a Doppler shift f_d, the following constants are defined

$$\gamma = \exp\left(-j2\pi\frac{T}{N}f_d\right) \tag{7.37}$$

$$a = \exp\left(-j2\pi\Delta f\tau\right) \tag{7.38}$$

and used to build diagonal matrices modeling the time and frequency shift in the received signal:

$$\mathbf{\Gamma}_1 = \mathrm{diag}\{\gamma^0, \gamma^1, \ldots, \gamma^{(N-1)}\} \tag{7.39}$$

$$\mathbf{\Gamma}_2 = \mathrm{diag}\{\gamma^0, \gamma^N, \ldots, \gamma^{(M-1)N}\} \tag{7.40}$$

where $\mathbf{\Gamma}_1 \in \mathbb{C}^{N\times N}$ represents the Doppler phase shift along subcarriers - the intercarrier interference - and $\mathbf{\Gamma}_2 \in \mathbb{C}^{M\times M}$ is the Doppler phase shift across subpulses. Analogously, a matrix form of the target range-related subcarrier phase shift is defined as

$$\mathbf{A} = \mathrm{diag}\{a^0, a^1, \ldots, a^{N-1}\} \tag{7.41}$$

with $\mathbf{A} \in \mathbb{C}^{N\times N}$. Finally, μ is a complex amplitude, and ψ represents the delay-dependent phase shift at carrier frequency

$$\psi = \exp\left(-j2\pi f_c\tau\right) \tag{7.42}$$

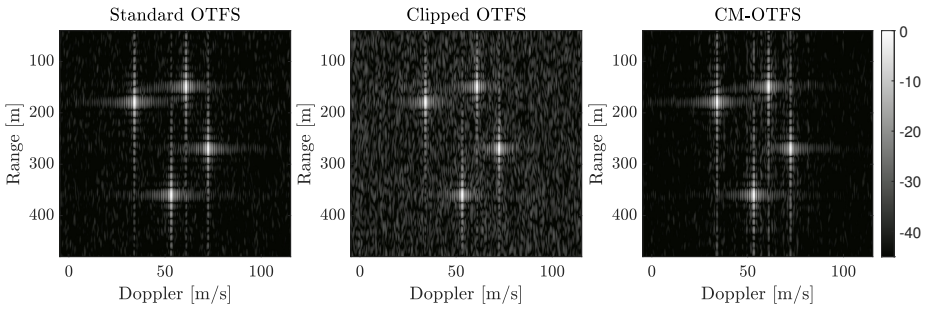

Figure 7.6: Noiseless Range-Doppler slice section for OTFS radar with different waveforms. On the left, standard OTFS with no amplifier effect. On the center, the same waveform with amplifier-caused amplitude clipping (IBO = 6 dB). On the right is a constant modulus OTFS waveform.

A radar receiver, based on the time-frequency domain phase normalization of the received signal (see Chapter 3 for a full description), is used to estimate the range-Doppler parameters in the received signal. This receiver assumes uncoupled range-Doppler estimation parameters, which are estimated sequentially and result in a computational complexity of $\mathcal{O}(N+M)$. The trade-off of this assumption is a reduced Doppler tolerance and unambiguous range-Doppler estimation compared to joint delay-Doppler receivers [72]. However, the computational complexity of joint delay-Doppler receivers is $\mathcal{O}(NM)$, which makes them impractical for relatively big frame sizes and fractional time and frequency shifts. Implementing this phase-normalization-based receiver involves a point-wise multiplication to normalize the phase, followed by a Symplectic Finite Fourier Transform (SFFT). The phase normalization is given by

$$\mathbf{Y}_{\text{norm}}[n,m] = \mathbf{Y}_{\text{TF}}[n,m]\exp\left(-j\Psi[n,m]\right) \tag{7.43}$$

where

$$\Psi[n,m] = \angle(\mathbf{X}_{\text{TF}}[n,m]) \tag{7.44}$$

for every $n \in \{1,\ldots,2N\}$ and $m \in \{1,\ldots,2M\}$. After phase normalization, the SFFT is performed to calculate the range-Doppler map. This receiver normalizes the received signal in the time-frequency domain and transforms the result into the delay-Doppler domain. If $[\tau_k, f_{d,k}] = [0,0]$, then $\mathbf{Y}_{\text{norm}}$ is an all-ones matrix, and its delay-Doppler representation $\mathbf{Y}^{\text{DD}}_{\text{norm}}$ appears as a peak at $[0,0]$. For any other pairs of $[\tau_k, f_{d,k}]$, the peak in $\mathbf{Y}^{\text{DD}}_{\text{norm}}$ is displaced to the corresponding index in the delay-Doppler plane.

7.4. PERFORMANCE ASSESSMENT OF CONSTANT-MODULUS OTFS

In this section, numerical simulations are performed to test the performance of CM-OTFS for radar and communications. The waveform parameters in Table. 7.1

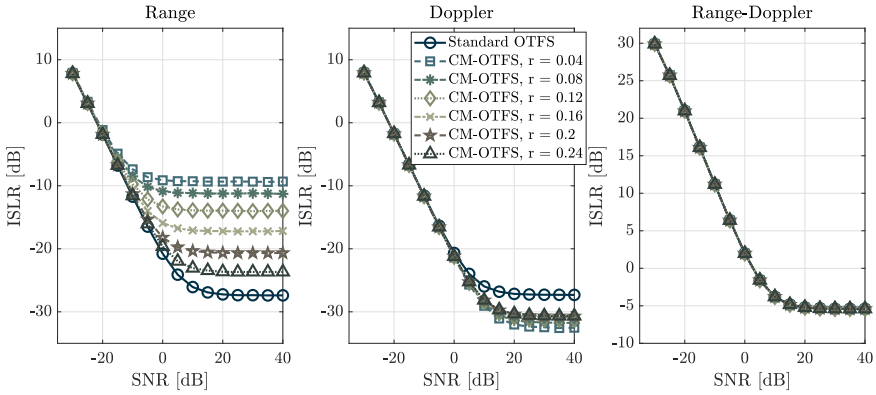

Figure 7.7: Integrated sidelobe level after range-Doppler estimation in target range slice, Doppler slice, and Range-Doppler map in the left, center, and right respectively.

are used for both radar and communications simulations.

7.4.1. CM-OTFS RADAR PERFORMANCE EVALUATION

The performance of CM-OTFS in radar applications is tested through numerical simulations. As OTFS is particularly well suited to high-mobility applications, a carrier frequency of 24 GHz is chosen, as bands around this frequency have been used for automotive radar, and are projected to be used in millimeter-wave communications for 6G under the label of FR3, therefore showing potential in applications for both sensing and communication in high-mobility scenarios [110]. The simulations are performed assuming a monostatic system, and the main waveform parameters are shown in Table 7.1. For the scope of this work, a monostatic single-input single-output (SISO) radar is considered.

The approach followed to evaluate CM-OTFS radar performance is to compare with two references: first, a baseline standard OTFS approach with the same subcarriers

Table 7.1: OTFS simulation waveform parameters

Parameter	Symbol	Value
Number of delay bins	N	256
Number of Doppler bins	M	256
Bandwidth	B	10 MHz
Carrier frequency	f_c	24 GHz
Symbol duration	T	25.6 μs
Intercarrier separation	Δf	39 kHz
Cyclic prefix duration	T_{cp}	12.8 μs
Communication Modulation	(−)	QPSK

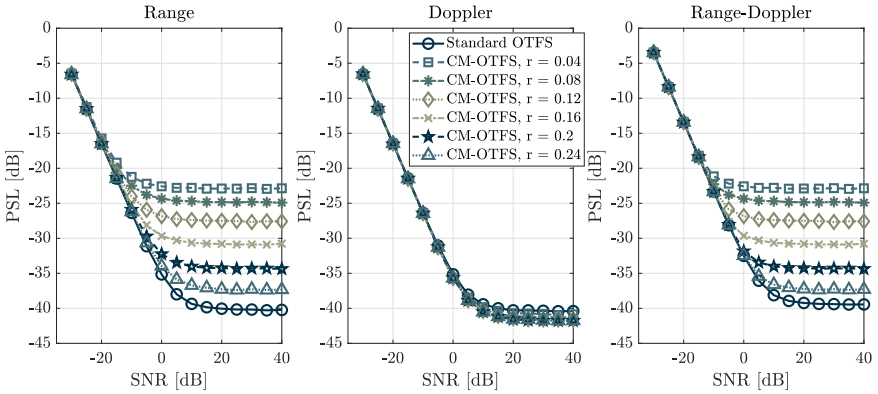

Figure 7.8: Normalized peak sidelobe level after range-Doppler estimation in target range slice, Doppler slice, and Range-Doppler map in the left, center, and right, respectively.

(N) and subsymbols (M), and second, an OTFS waveform with amplifier-related distortion due to the non-uniform amplitude of the time-domain signal. The radar estimation is performed with the standard DFT-based spectral division receiver for all three cases. In the case of the distorted OTFS signal, the original transmitted OTFS signal is used for radar processing. Fig. 7.6 shows the range-velocity maps of standard OTFS, amplitude-clipped OTFS due to amplifier saturation, and CM-OTFS. Four-point targets are present in the simulation, and no tapering is used in the estimation, resulting in similar sinc-like sidelobes around the targets. A stronger noise-like background appears in the clipped-OTFS waveform when compared to standard OTFS, which we attribute to the mismatch between the original signal and the distorted transmitted signal. CM-OTFS shows slightly increased noise-like sidelobes around the main range sinc-like sidelobes, but they are contained to the Doppler cells around the target. Overall, the sidelobe level of CM-OTFS is better than that of the clipped OTFS waveform and close to the performance of a standard OTFS frame.

A quantitative study of the sidelobe characteristics of the waveforms for a single target is shown in Figs. 7.7 and 7.8. Fig. 7.7 shows the integrated sidelobe ratio (ISLR) in the range cut, Doppler cut, and whole range-Doppler surfaces for standard OTFS and CM-OTFS for different values of r. The ISLR is defined as the integrated sidelobe power in an estimation normalized to the main-lobe peak [90]. First, when the measurement is noise-dominated (i.e., the sidelobes are buried under the noise), standard OTFS and CM-OTFS perform the same regarding sidelobe power. For sidelobe-dominated estimations (i.e., higher SNR values), we observe that the ISLR in the range cut increases (meaning higher sidelobe power) in CM-OTFS compared to standard OTFS. Moreover, the higher the value of the parameter r, the higher the sidelobes in the range cut. In the Doppler cut, we see a similar behavior regarding the noise, but now standard OTFS shows slightly higher sidelobe power at high noise levels. Finally, the ISLR on the range-Doppler slice shows that standard OTFS and

CM-OTFS have the same sidelobe power. This implies that the differences in ISLR in the range and Doppler cuts are due to a redistribution of the sidelobe power and not an overall increase in the sidelobe level.

Changes in the structure of the sidelobes can result in increased peak-to-sidelobe level (PSL), which increases the chances of target masking. Fig. 7.8 shows the PSL of standard OTFS and CM-OTFS for different values of SNR. Similarly, as with ISLR, we can see that as long as the measurements are noise-dominated, the PSL of the estimation is the same in all waveforms, as it simply reflects the peak of the noise floor. For higher SNR values, we observe an increase in PSL in the range-domain that worsens as the value of r decreases. Moreover, this increased range sidelobe becomes the dominating sidelobe in the entire range-Doppler domain, as shown by the fact that the PSL value in the range-Doppler surface matches the PSL value in the range cut.

Overall, if we compare the results of ISLR with the ISLR in standard OTFS with amplifier clipping (Fig. 7.3), we can see that for a value of e.g. IBO = 0, the expected ISLR for clipped OTFS with $M = 256$ is around 5 dB, whereas in CM-OTFS the ISLR would be -5 dB, meaning an improvement of 10 dB over the amplifier clipped waveform, at the cost of the sidelobe-power being focused in a higher range peak sidelobe. In the end, whether a constant modulus approach is desirable in terms of radar will depend mostly on the characteristics of the amplifier and power requirements, which will define the expected distortion on the transmitted signal.

7.4.2. CM-OTFS COMMUNICATION PERFORMANCE EVALUATION

To evaluate the communications performance of the proposed CM-OTFS waveform, an LMMSE detector [88] is used for an OTFS frame. It is assumed that perfect channel state information is available, the channel effects have been compensated for, and only noise is present. The goal of this evaluation is to verify that the original delay-Doppler symbols can be reconstructed from a CM-OTFS frame and, similarly to the radar numerical evaluation, to determine how the performance of CM-OTFS compares to a pristine OTFS frame and OTFS frames that are distorted due to the amplitude clipping caused by amplifier saturation. The same waveform parameters as before (Table 7.1) are used for the simulations in this section, and the steps in (7.25 - 7.32) are followed for symbol recovery. As the number of subcarriers and subsymbols (delay and Doppler bins) is equal in both standard OTFS and CM-OTFS, CM-OTFS carries a quarter of the symbols and achieves a quarter of the communication rate. The communication symbols are sampled from a uniform random distribution.

The iterative decoding process to retrieve the data symbols from the complementary sequences in the received signal can result in a cumulative phase error in the presence of noise. Using a double differential encoding (DDE) in the transmitted symbols can help mitigate this effect [38]. First, the transmitted symbols $\mathbf{a}(n) \in \mathbb{C}^{1\times M}$ are separated in two sub-signals formed by the even and odd Doppler indexes, $\mathbf{a}_E(n) \in \mathbb{C}^{1\times M/2}$ and $\mathbf{a}_O(n) \in \mathbb{C}^{1\times M/2}$ respectively. Assuming a phase-only modulation,

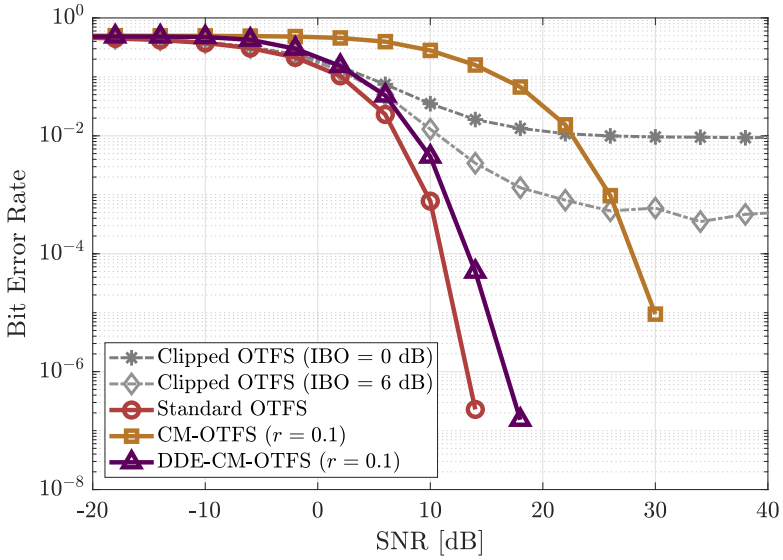

Figure 7.9: Bit Error Rate (BER) for an increasing value of SNR for distorted and pristine OTFS, and CM-OTFS with and without double differential encoding.

differential encoding can be applied to each of them separately, resulting in

$$d_E[m] = a_E[m]a_E[m-1] \tag{7.45}$$

$$d_O[m] = a_O[m]a_O[m-1] \tag{7.46}$$

and then new data vectors $\mathbf{a}^{\text{DDE}} \in \mathbb{C}^{1\times M}$ can be formed by interleaving the elements of $\mathbf{d}_O$ and $\mathbf{d}_E$. Double differential decoding is applied at the receiver by reversing the previous process. For consistency with (7.45) and (7.46), we relabel the recovered differential-encoded symbols from (7.30) as $\hat{\mathbf{a}}^{\text{DDE}}$, which we separate in even $\hat{\mathbf{d}}_E$ and odd $\hat{\mathbf{d}}_O$, and used to compute the double differential decoding

$$\hat{a}_E[m] = \hat{d}_E[m]\exp(-j\arg(d_E[m])) \tag{7.47}$$

$$\hat{a}_O[m] = \hat{d}_O[m]\exp(-j\arg(d_O[m])) \tag{7.48}$$

and the recovered data vectors $\hat{\mathbf{a}}^{\text{DDE}} \in \mathbb{C}^{1\times M}$ are formed by interleaving the elements of $\hat{\mathbf{a}}_O$ and $\hat{\mathbf{a}}_E$ for each $n \in \{0,\ldots,N-1\}$. In (7.47), (7.48), the phase of the previous symbol is used for differential decoding to avoid any changes in amplitude. This process is repeated for each $n \in \{0,\ldots,N-1\}$, resulting in the estimated vectors $\hat{\mathbf{a}}^{\text{DDE}}(n)$ that form the estimated delay-Doppler data matrix as in (7.33). Note that to perform DDE, the transmitter and receiver need to agree on a starting reference phase for the first symbol, which, in our case, is zero degrees. We label the resulting signal double differential encoded constant modulus OTFS (DDE-CM-OTFS).

The bit error rate (BER) for the evaluated waveforms and increasing SNR values is shown in Fig. 7.9. The results are the average of 1000 Monte Carlo simulations

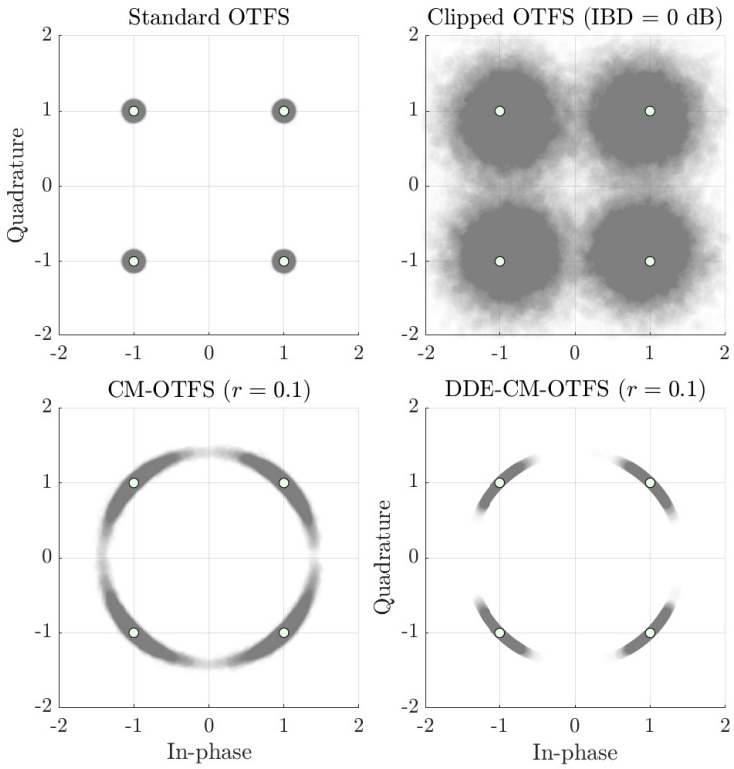

Figure 7.10: Constellation of reconstructed symbols after channel compensation for SNR = 30 dB. Pristine OTFS on the top-left, amplifier distorted OTFS on the top-right, CM-OTFS on the bottom-left, and DDE-CM-OTFS on the bottom-right.

for each waveform and SNR step. The simulations show that undistorted OTFS (red) achieves the best BER values, achieving the same BER as CM-OTFS (yellow), with SNR being lower by 15 dB. Although both CM-OTFS and undistorted OTFS tend towards a BER of zero for sufficiently high values of SNR, an SNR loss of around 15 dB is severe in most applications, even if the constant-envelope property of CM-OTFS enables high-power transmission. The decrease in BER for a given SNR is caused by the iterative nature of the symbol retrieval from the complementary sequences, as an early error propagates to future iterations, as seen in CM-OFDM. Double differential encoding (DDE) [109] can be used prior to the complementary sequence synthesis to ensure the phase errors only propagate for a maximum of two iterations in the decoding process. The resulting waveform, namely DDE-CM-OTFS, significantly improves the performance of CM-OTFS and achieves BER similar to standard pristine OTFS, as shown in Fig. 7.9 (purple curve), while maintaining all the advantages of CM-OTFS. For amplitude-clipped OTFS, the BER plateaus at a non-zero value, regardless of the SNR. As the amplifier-related distortion is not

channel-dependent, it creates constant noise regardless of the channel conditions. When considering possible use-cases of ISAC OTFS systems that involve high power transmission for radar operation, not achieving a good BER due to the amplitude clipping, regardless of the high signal level, is a substantial shortcoming with non-constant modulus signals such as OTFS. Instead, when CM-OTFS is used, good communication links could be established, as CM-OTFS enables high power transmission without distortion, helping to bridge the gap of required SNR.

To gain a better understanding of the role of the CM-OTFS frame synthesis approach in the degradation of communications performance, the recovered symbol constellation for a high SNR iteration (SNR = 30 dB) is plotted in Fig. 7.10. This representation shows the spread of the symbols caused primarily by channel-unrelated effects. For Clipped OTFS, we see a substantial increase in random noise-like error when compared to pristine OTFS, showing that the amplitude clipping appears similar to white Gaussian noise in the IQ plane. The stronger the distortion (the lower the IBO), the higher the symbols spread. The recovered CM-OTFS symbols display a similar level of spread in terms of magnitude to pristine OTFS but also show a considerable phase deviation caused by the cumulative phase error in the decoding process, resulting in reduced communications performance. It is observed in simulations that as the SNR increases, the phase error decreases until it disappears, resulting in the steadily decreasing BER value in Fig. 7.9. The phase drift in the recovered symbols using double differential encoding (DDE-CM-OTFS) is significantly reduced, resulting in considerable performance improvement compared to standard CM-OTFS.

7.5. EXPERIMENTAL VALIDATION OF CM-OTFS RADAR

In this section, experimental results of CM-OTFS radar are presented and compared with standard OTFS radar with and without amplifier-related distortion. The data are acquired using the PARSAX radar [91], a polarimetric waveform-agile radar used previously to validate MIMO NU-OTFS [97]. For the experiments in this work, a single polarimetric channel (HH) is used to measure a static target at a distance of 1185 meters. The radar and the target are shown in Fig. 7.11. Three measurements

Table 7.2: OTFS experimental waveform parameters

Parameter	Symbol	Value
Number of delay bins	N	1024
Number of Doppler bins	M	812
Bandwidth	B	40 MHz
Carrier frequency	f_c	3.315 GHz
Symbol duration	T	25.6 μs
Intercarrier separation	Δf	39.06 kHz
Cyclic prefix duration	T_{cp}	12.8 μs
Communication Modulation	(−)	QPSK

Figure 7.11: PARSAX (left) and measured industrial chimney at approximately 1185 meters from the radar sensor (right).

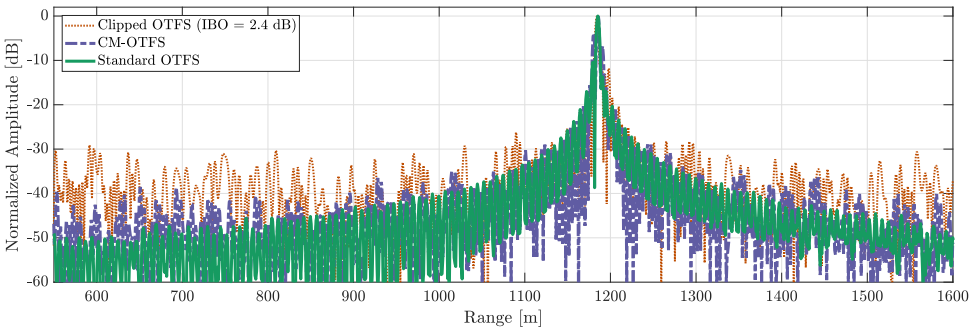

Figure 7.12: Range cut of the range-Doppler radar estimation measured with PARSAX, without tapering. All estimations are normalized to their maximum and show a peak at the correct target position.

are carried out: first, a standard OTFS frame is used without any amplifier-caused distortion; second, a signal with simulated amplifier-caused amplitude clipping $\gamma = 3$ is used to measure the same target; finally, a measurement is carried out with the proposed CM-OTFS waveform ($r = 0.1$). The waveform parameters are shown in Table. 7.2 are set so that all waveforms share the same coherent processing time and bandwidth. The implication is that the CM-OTFS waveform transmits only a quarter of the communication symbols as the other two waveforms.

The zero-Doppler range cut for all three waveforms is shown in Fig. 7.12, where it can be seen that all three waveforms show a clear peak in the correct position of the target at 1185 meters. It is also apparent that the standard undistorted OTFS waveform shows the best estimation, with the highest dynamic range. The CM-OTFS measurement shows slightly increased sidelobe levels, particularly far from the target

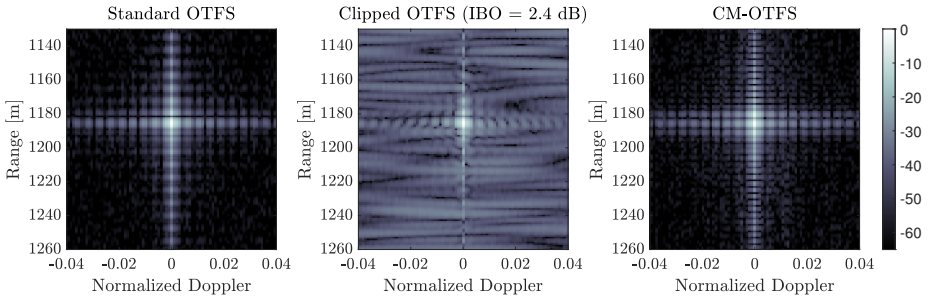

Figure 7.13: Range-Doppler radar estimation measured with PARSAX, without tapering. Pristine OTFS on the left, OTFS with simulated amplifier distortion (IBO = 2.4 dB) in the center, and CM-OTFS on the right.

position, but comparatively lower than the measurement with the distorted OTFS signal, represented by the orange dotted curve. CM-OTFS shows around 5 to 10 dB lower sidelobes than the measurement performed with an OTFS waveform suffering from simulated amplifier distortion. On the other hand, close side peaks appear in the range estimation next to the main peak of the CM-OTFS waveform, which aligns with the observation in the simulation of the degradation in radar performance of CM-OTFS compared to standard OTFS, affecting primarily the range cut. More observations can be made from Fig. 7.13, where the range-Doppler map around the target position is shown for all three waveforms. The standard OTFS measurement, on the left, shows the typical sync-like decreasing sidelobes in both range and Doppler. The clipped OTFS measurement shows a slightly increased range and Doppler sidelobes in the cells aligned with the target positions, but more importantly, it shows approximately 30 dB degradation in the bins not aligned with the correct range-Doppler. This sort of degradation extends over the entire range-Doppler plane. It would significantly impair the estimation of multiple targets, particularly considering that there is no access to the distorted signal in the system that could otherwise be used to remove the sidelobes through model-based processing. Finally, the sidelobes in the CM-OTFS waveform are also steadily decreasing sinc-like sidelobes. Although they extend to the spurious peaks adjacent to the correct target position, they are confined to those specific range values and do not affect other areas of the range-Doppler plane.

In addition to the radar performance, we assess the communication functionality by recovering the delay-Doppler symbols embedded in the received radar waveform. The radar receive chain is re-purposed as a communications receiver: the range–Doppler estimate obtained from the monostatic radar processing is treated as a single-path channel estimate, the dominant path corresponding to the chimney reflection. This estimate is then used to equalize the base-band signal and to decode the delay-Doppler symbols following the procedure of Section IV-B. The resulting symbol constellations are depicted in Fig. 7.14. As expected, pristine OTFS exhibits the tightest clustering. The clipped-OTFS case, which emulates amplifier saturation, shows a noticeable dispersion that would increase the probability of symbol errors at

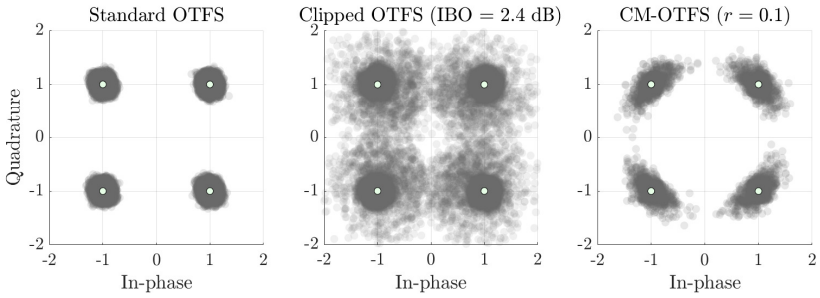

Figure 7.14: Constellation of reconstructed symbols at the radar receiver. Channel compensation is performed using the monostatic radar estimation, assuming a single path.

modest SNR. Crucially, the symbols conveyed with the proposed CM-OTFS waveform are successfully recovered after equalisation, and their scatter matches the trend observed in the simulations.

These findings validate the end-to-end signal-processing chain proposed for CM-OTFS operation, confirming that both sensing and communications functions can be achieved without requiring separate hardware paths or calibration steps. The experiment therefore demonstrates the practical viability of CM-OTFS as a dual-function waveform under realistic front-end constraints. In fact, the experimental results with the clipped signal show more degradation than the degradation predicted in simulations, suggesting that abrupt amplitude clipping in the signal causes further hardware-related non-linear effects than those modeled in our numerical simulations.

7.6. CONCLUSION

This chapter delivers the first systematic analysis of power-amplifier (PA)-induced distortion in OTFS and introduces CM-OTFS, the first constant-envelope OTFS waveform designed for ISAC. We prove analytically and numerically that the PAPR of conventional OTFS grows with the number of Doppler bins, directly degrading radar detectability and communication reliability under realistic PA back-off constraints. To overcome this issue, we proposed a novel variation of OTFS, namely CM-OTFS. Inspired by a preexisting OFDM technique, CM-OTFS employs complementary sequences and the Zak transform to embed delay-Doppler symbols into a strictly constant-modulus time-domain signal, all while preserving OTFS's Doppler resilience.

The performance of CM-OTFS has been evaluated through a combination of numerical simulations and radar experiments. Radar numerical and experimental over-the-air tests show that CM-OTFS performs slightly worse than pristine OTFS in target estimation but outperforms OTFS with amplifier distortion, with the gap widening as the signal distortion increases. The noise tolerance of CM-OTFS communications was improved by using double differential encoding, achieving BER

performance close to that of pristine OTFS. This robustness comes at a trade-off in communication throughput, as a fourfold reduction in data rate. The results presented suggest that CM-OTFS is a novel and promising alternative to standard OTFS for ISAC applications. In particular, it is well suited for systems where high-power operation and/or low-cost front-end components are required, or as a tool to enable high-power sensing modes in adaptive/cognitive ISAC systems with limited repercussions in communication performance.

8

CONCLUSION

"There is no perfection, only life."
— Milan Kundera

This chapter summarizes the thesis's contributions to OTFS-based radar operation for integrated sensing and communications. Concluding remarks are presented, and potential avenues for future research are outlined.

8.1. CONCLUDING REMARKS

In this thesis, I introduced three novel extensions that significantly advanced state-of-the-art OTFS waveform design and signal processing for 5G/6G integrated sensing-and-communications (ISAC) radar. I successfully tackled two standing challenges, high envelope variation and a rigid, fully populated time–frequency structure, thereby advancing towards turning OTFS into a practically deployable radar waveform. My overarching goal was to adapt OTFS, originally optimised for communications, into a high-performance sensing waveform without sacrificing spectral efficiency or Doppler robustness.

In Chapter 3, I developed and compared several radar receiver architectures for OTFS and OFDM to clarify how the two waveforms differ and align in monostatic radar sensing. This work answered the first research question:

Q1: *How do the differences in structure between OFDM and OTFS translate to radar sensing, and does the Doppler resilience of OTFS in communications transfer to monostatic radar sensing?*

In previous work, significant differences between the performance of OTFS and OFDM monostatic radar were attributed to the structure of the waveform, reinforcing the idea that OTFS shows inherent advantages, particularly in terms of Doppler tolerance. However, by formulating both waveforms with a shared multicarrier radar model and performing a "head-to-head" analysis, it was revealed that the "inherent

Doppler immunity" of OTFS radar actually stems from receiver assumptions rather than waveform physics, answering our first research question. The results show that, depending on the level of complexity of the receiver and the modeling of the ICI and ISI effects, radar receivers could be formulated for both waveforms. The results showed that the waveforms are qualitatively similar to each other, and that the bulk of the difference in radar performance can be attributed to the receiver design.

In chapter **4**, I proposed a novel generalization of the OTFS signal synthesis process to accommodate more flexibility in terms of time-frequency structure, giving rise to a novel waveform that I termed Non-Uniform OTFS (NU-OTFS). This work addressed the second research question of the thesis:

Q2: *What are practical ways of enabling flexible time-frequency multiple access for MIMO radar and MIMO/multi-user communications for OTFS?*

This question was chosen because MIMO is pivotal for radar, while multi-user service is essential for public communications; both face a common challenge: multiple access of transmitters in MIMO radar and of users in communication systems. A typical solution is to allocate non-overlapping time–frequency resources, which is straightforward in OFDM. Traditional OTFS, however, spreads information over contiguous time–frequency tiles, so multiple OTFS messages in the same band overlap and impede multiple-access capability. To address this limitation, I proposed a generalised OTFS synthesis that permits arbitrary time–frequency allocation patterns and coined the resulting waveform Non-Uniform OTFS (NU-OTFS). This scheme increases resource-allocation flexibility, enables MIMO radar and multi-user communication, and improves interference avoidance compared with conventional OTFS. The performance of NU-OTFS for MIMO radar and for communications in high-mobility channels was analysed, confirming that OTFS's key advantages are preserved while its flexibility is enhanced. The chapter also presented the first over-the-air validation of OTFS radar and examined NU-OTFS using artificially sparsified measured data.

The concept of NU-OTFS is further explored in chapters **5** and **6**. In chapter **5**, I presented a novel study of the link between the time-frequency patterns of NU-OTFS and the expected MIMO radar performance, shedding some light on the extent of sparsity and interference that NU-OTFS can tolerate for radar applications. In chapter **6**, a fully polarimetric radar was used to explore the separability between non-uniform time-frequency representations achieved through NU-OTFS. The result is the first validation of simultaneous OTFS MIMO radar through measurements in the literature, albeit in a slightly unorthodox manner. With that, I closed our research in OTFS multiple access for radar and communications, and moved to our next research topic.

Chapter **7** I tackled the issue of non-constant envelope that OTFS shares to a great extent with OFDM, and that limits the implementation of OFDM and OTFS in high-power radar systems. Motivated by this, I aimed to answer our final research question:

Q3: *How can a constant-envelope (or ultra-low-PAPR) OTFS waveform be designed,*

such that it preserves its delay–Doppler sensing fidelity and key communication characteristics?

To answer this question, I introduced a novel method for generating a constant-envelope, time-domain OTFS signal. The resulting waveform, termed constant-modulus OTFS (CM-OTFS) to emphasise its link to the earlier CM-OFDM scheme, enables the synthesis of constant-envelope OTFS frames and removes the PAPR bottleneck that limits high-power OTFS-based ISAC applications. Although CM-OTFS transmits only one quarter of the information carried by a standard OTFS frame, it surpasses power-amplifier-distorted OTFS in both radar and communication tasks. Radar and communication performance were validated through numerical simulations, and representative measurements were conducted to confirm the radar results experimentally.

Collectively, these contributions help transform OTFS from a Doppler-tolerant, communications-centric OFDM alternative into a radar-ready waveform family that scales to dense MIMO arrays, fragmented spectra, and high-power front-ends, helping to lay a solid foundation for next-generation ISAC systems.

8.2. RESEARCH OPPORTUNITIES

Although I have addressed some of the major challenges that OTFS faced in ISAC systems, a multitude of open research questions remain unanswered when it comes to future OTFS radar and ISAC systems:

RO1: *What are alternative efficient implementations of a radar receiver design for OTFS that carry some of the advantages of the joint delay-Doppler receiver but remain computationally efficient?*

For receiver design, an efficient implementation of the joint delay-Doppler receiver that carries over the Doppler tolerance of OTFS in communications for radar operation is crucial. Mobile radar platforms may not have sufficient computing power to achieve the required frame rate and parameter estimation performance otherwise, especially as frame sizes grow to dimensions similar to the standards of OFDM.

RO2: *What are the trade-offs between different approaches to multiple access with OTFS for MU communications and MIMO radar?*

Regarding MIMO waveform design and spectral compatibility, different visions for OTFS MIMO coexist: delay-Doppler multiplexing and time-frequency multiplexing. A delay-Doppler multiplexing approach better suited to multiuser communications and spectral flexibility is an open challenge. On the other hand, although spectral flexibility and compatibility with multiuser MIMO communications are appealing, further research into the trade-offs and performance bounds of the non-uniform time-frequency multiplexing approach is required before conclusions can be drawn about its potential.

Although crucial, receiver and waveform design are not the only directions in which OTFS radar-communication systems face challenges:

RO3: *What are alternative approaches to deal with the high PAPR of OTFS?*

Although a specific solution was given in this dissertation, other approaches with different trade-offs should be possible. Further research in this direction is necessary to find the best alternative for different use cases.

RO4: *Is there a way to limit the receiver bandwidth in OTFS such that high bandwidths are possible with reduced data rates?*

FMCW is an extremely popular radar waveform in civil applications, particularly where low-cost modules such as automotive and drone radars are preferred. This is partially due to the beat-frequency processing reducing the required receiver bandwidth relative to the measurement bandwidth in FMCW radars. This is not the case for OTFS, and no solution to tackle this limitation has been proposed to the best of the author's knowledge. Moreover, the data rate required for all fully digital radars, including OTFS, is a strong limitation regarding system design [7].

RO5: *What are the properties of multistatic OTFS radar, opposite to monostatic setups?*

In this thesis, I have focused on monostatic OTFS radar, where the transmitted waveform is known in the receiver (besides issues with, e.g., amplifier distortion). The case of multistatic radar, particularly when only part of the signal is known (the pilot signal), is not investigated in this thesis and is of great importance when it comes to ISAC implementations with networked systems that operate both as sensors and communication nodes. Research on pilot form and structure in OTFS frames and the associated radar and communication trade-offs is still in an early stage and crucial for many relevant applications.

RO6: *How would we define application-specific ISAC requirements for waveforms such as OTFS and OFDM?*

This is a challenge that research in OTFS multifunctional systems shares with other ISAC research: the scenarios in which such systems will be helpful are loosely described. A better understanding of the capabilities and limitations of distributed system structures with collaborative sensing (monostatic or multistatic) in centralized or ad-hoc communication networks would lay the groundwork for guiding further basic research on the capabilities of OTFS and physical layer waveforms for future ISAC systems.

REFERENCES

[1] K. V. Mishra, M. Bhavani Shankar, V. Koivunen, B. Ottersten, and S. A. Vorobyov. "Toward Millimeter-Wave Joint Radar Communications: A Signal Processing Perspective". In: *IEEE Signal Processing Magazine* 36.5 (Sept. 2019), pp. 100–114. ISSN: 1558-0792. DOI: 10.1109/MSP.2019.2913173.

[2] A. Liu, Z. Huang, M. Li, Y. Wan, W. Li, T. X. Han, C. Liu, R. Du, D. K. P. Tan, J. Lu, *et al.* "A survey on fundamental limits of integrated sensing and communication". In: *IEEE Communications Surveys & Tutorials* 24.2 (2022), pp. 994–1034.

[3] D. K. P. Tan, J. He, Y. Li, A. Bayesteh, Y. Chen, P. Zhu, and W. Tong. "Integrated sensing and communication in 6G: Motivations, use cases, requirements, challenges and future directions". In: *2021 1st IEEE International Online Symposium on Joint Communications & Sensing (JC&S)*. IEEE. 2021, pp. 1–6.

[4] O. Bialer, A. Jonas, and T. Tirer. "Super resolution wide aperture automotive radar". In: *IEEE Sensors Journal* 21.16 (2021), pp. 17846–17858.

[5] K. Harlow, H. Jang, T. D. Barfoot, A. Kim, and C. Heckman. "A new wave in robotics: Survey on recent mmwave radar applications in robotics". In: *IEEE Transactions on Robotics* (2024).

[6] G. Hakobyan and B. Yang. "High-Performance Automotive Radar: A Review of Signal Processing Algorithms and Modulation Schemes". In: *IEEE Signal Processing Magazine* 36.5 (Sept. 2019), pp. 32–44. ISSN: 1558-0792. DOI: 10.1109/MSP.2019.2911722.

[7] B. Schweizer, A. Grathwohl, G. Rossi, P. Hinz, C. Knill, S. Stephany, H. J. Ng, and C. Waldschmidt. "The Fairy Tale of Simple All-Digital Radars: How to Deal With 100 Gbit/s of a Digital Millimeter-Wave MIMO Radar on an FPGA [Application Notes]". In: *IEEE Microwave Magazine* 22.7 (July 2021), pp. 66–76. ISSN: 1557-9581. DOI: 10.1109/MMM.2021.3069602.

[8] L. Zheng, M. Lops, Y. C. Eldar, and X. Wang. "Radar and communication coexistence: An overview: A review of recent methods". In: *IEEE Signal Processing Magazine* 36.5 (2019), pp. 85–99.

[9] F. Liu, Y. Cui, C. Masouros, J. Xu, T. X. Han, Y. C. Eldar, and S. Buzzi. "Integrated sensing and communications: Toward dual-functional wireless networks for 6G and beyond". In: *IEEE journal on selected areas in communications* 40.6 (2022), pp. 1728–1767.

[10] Y. Cui, F. Liu, X. Jing, and J. Mu. "Integrating sensing and communications for ubiquitous IoT: Applications, trends, and challenges". In: *IEEE network* 35.5 (2021), pp. 158–167.

[11] J. Choi, V. Va, N. Gonzalez-Prelcic, R. Daniels, C. R. Bhat, and R. W. Heath. "Millimeter-wave vehicular communication to support massive automotive sensing". In: *IEEE Communications Magazine* 54.12 (2016), pp. 160–167.

[12] J. Mu, R. Zhang, Y. Cui, N. Gao, and X. Jing. "UAV meets integrated sensing and communication: Challenges and future directions". In: *IEEE Communications Magazine* 61.5 (2023), pp. 62–67.

[13] R. Hadani, S. Rakib, M. Tsatsanis, A. Monk, A. J. Goldsmith, A. F. Molisch, and R. Calderbank. "Orthogonal Time Frequency Space Modulation". en. In: *2017 IEEE Wireless Communications and Networking Conference (WCNC)*. San Francisco, CA, USA: IEEE, Mar. 2017, pp. 1–6. ISBN: 978-1-5090-4183-1. DOI: 10.1109/WCNC.2017.7925924. (Visited on 07/09/2020).

[14] L. Gaudio, G. Colavolpe, and G. Caire. "OTFS vs. OFDM in the presence of sparsity: A fair comparison". In: *IEEE Transactions on Wireless Communications* 21.6 (2021), pp. 4410–4423.

[15] R. Prasad. *OFDM for wireless communications systems*. Vol. 2. Artech House, 2004.

[16] D. Khosla, S. Singh, R. Singh, and S. Goyal. "OFDM modulation technique & its applications: a review". In: *International Conference on Innovations in Computing (ICIC 2017)*. 2017, pp. 101–105.

[17] T. Hwang, C. Yang, G. Wu, S. Li, and G. Y. Li. "OFDM and its wireless applications: A survey". In: *IEEE transactions on Vehicular Technology* 58.4 (2008), pp. 1673–1694.

[18] L. Litwin and M. Pugel. "The principles of OFDM". In: *RF signal processing* 2 (2001), pp. 30–48.

[19] G. Hakobyan. "Orthogonal frequency division multiplexing multiple-input multiple-output automotive radar with novel signal processing algorithms". en. In: (2018). Accepted: 2018-05-29T07:58:12Z. DOI: 10.18419/opus-9830. URL: http://elib.uni-stuttgart.de/handle/11682/9847 (visited on 09/01/2022).

[20] C. Sturm, E. Pancera, T. Zwick, and W. Wiesbeck. "A novel approach to OFDM radar processing". In: *2009 IEEE Radar Conference*. ISSN: 2375-5318. May 2009, pp. 1–4. DOI: 10.1109/RADAR.2009.4977002.

[21] R. F. Tigrek, W. J. A. de Heij, and P. van Genderen. "Multi-carrier radar waveform schemes for range and Doppler processing". In: *2009 IEEE Radar Conference*. ISSN: 2375-5318. May 2009, pp. 1–5. DOI: 10.1109/RADAR.2009.4976986.

[22] G. Franken, H. Nikookar, and P. V. Genderen. "Doppler Tolerance of OFDM-coded Radar Signals". In: *2006 European Radar Conference*. Sept. 2006, pp. 108–111. DOI: 10.1109/EURAD.2006.280285.

[23] G. Hakobyan and B. Yang. "A Novel Intercarrier-Interference Free Signal Processing Scheme for OFDM Radar". In: *IEEE Transactions on Vehicular Technology* 67.6 (June 2018), pp. 5158–5167. ISSN: 1939-9359. DOI: 10.1109/TVT.2017.2723868.

[24] T. M. C. Chu, H.-J. Zepernick, A. Westerhagen, A. Höök, and B. Granbom. “Performance Assessment of OTFS Modulation in High Doppler Airborne Communication Networks”. en. In: *Mobile Networks and Applications* (Feb. 2022). ISSN: 1572-8153. DOI: 10.1007/s11036-022-01928-4. URL: https://doi.org/10.1007/s11036-022-01928-4 (visited on 03/02/2022).

[25] P. Raviteja, Y. Hong, E. Viterbo, and E. Biglieri. “Practical Pulse-Shaping Waveforms for Reduced-Cyclic-Prefix OTFS”. In: *IEEE Transactions on Vehicular Technology* 68.1 (Jan. 2019), pp. 957–961. ISSN: 1939-9359. DOI: 10.1109/TVT.2018.2878891.

[26] G. D. Surabhi, R. M. Augustine, and A. Chockalingam. “Peak-to-Average Power Ratio of OTFS Modulation”. In: *IEEE Communications Letters* 23.6 (June 2019), pp. 999–1002. ISSN: 1558-2558. DOI: 10.1109/LCOMM.2019.2914042.

[27] P. Raviteja, E. Viterbo, and Y. Hong. “OTFS Performance on Static Multipath Channels”. In: *IEEE Wireless Communications Letters* 8.3 (June 2019), pp. 745–748. ISSN: 2162-2345. DOI: 10.1109/LWC.2018.2890643.

[28] P. Raviteja, K. T. Phan, Y. Hong, and E. Viterbo. “Orthogonal Time Frequency Space (OTFS) Modulation Based Radar System”. In: *2019 IEEE Radar Conference (RadarConf)*. ISSN: 2375-5318. Apr. 2019, pp. 1–6. DOI: 10.1109/RADAR.2019.8835764.

[29] M. F. Keskin, H. Wymeersch, and A. Alvarado. “Radar Sensing with OTFS: Embracing ISI and ICI to Surpass the Ambiguity Barrier”. In: *arXiv:2103.16162 [eess]* (Apr. 2021). arXiv: 2103.16162. (Visited on 04/02/2021).

[30] I. Van der Werf, H. Dol, K. Blom, R. Heusdens, R. C. Hendriks, and G. Leus. “On the equivalence of OSDM and OTFS”. In: *Signal Processing* 214 (2024), p. 109254.

[31] T. Kebede, Y. Wondie, J. Steinbrunn, H. B. Kassa, and K. T. Kornegay. “Multi-carrier waveforms and multiple access strategies in wireless networks: Performance, applications, and challenges”. In: *IEEE Access* 10 (2022), pp. 21120–21140.

[32] G. Hakobyan and B. Yang. “A novel OFDM-MIMO radar with non-equidistant subcarrier interleaving and compressed sensing”. In: *2016 17th International Radar Symposium (IRS)*. ISSN: 2155-5753. May 2016, pp. 1–5. DOI: 10.1109/IRS.2016.7497312.

[33] C. Knill, F. Roos, B. Schweizer, D. Schindler, and C. Waldschmidt. “Random Multiplexing for an MIMO-OFDM Radar With Compressed Sensing-Based Reconstruction”. In: *IEEE Microwave and Wireless Components Letters* 29.4 (Apr. 2019), pp. 300–302. ISSN: 1558-1764. DOI: 10.1109/LMWC.2019.2901405.

[34] G. Hakobyan, M. Ulrich, and B. Yang. “OFDM-MIMO Radar With Optimized Nonequidistant Subcarrier Interleaving”. In: *IEEE Transactions on Aerospace and Electronic Systems* 56.1 (Feb. 2020), pp. 572–584. ISSN: 1557-9603. DOI: 10.1109/TAES.2019.2920044.

[35] M. F. Keskin, C. Marcus, O. Eriksson, A. Alvarado, J. Widmer, and H. Wymeersch. “Integrated Sensing and Communications With MIMO-OTFS: ISI/ICI Exploitation and Delay-Doppler Multiplexing”. In: *IEEE Transactions on Wireless Communications* 23.8 (2024), pp. 10229–10246. DOI: 10.1109/TWC.2024.3370501.

[36] V. Khammammetti and S. K. Mohammed. “OTFS-Based Multiple-Access in High Doppler and Delay Spread Wireless Channels”. In: *IEEE Wireless Communications Letters* 8.2 (Apr. 2019), pp. 528–531. ISSN: 2162-2345. DOI: 10.1109/LWC.2018.2878740.

[37] S. C. Thompson, A. U. Ahmed, J. G. Proakis, J. R. Zeidler, and M. J. Geile. “Constant envelope OFDM”. In: *IEEE transactions on communications* 56.8 (2008), pp. 1300–1312.

[38] K. Willstatter and M. D. Zoltowski. “Complementary sequence construction for constant-envelope OFDM transmission enabling nonlinear amplification and clipping”. In: *MILCOM 2021-2021 IEEE Military Communications Conference (MILCOM)*. IEEE. 2021, pp. 390–395.

[39] S. Sun, A. P. Petropulu, and H. V. Poor. “MIMO Radar for Advanced Driver-Assistance Systems and Autonomous Driving: Advantages and Challenges”. In: *IEEE Signal Processing Magazine* 37.4 (July 2020), pp. 98–117. ISSN: 1558-0792. DOI: 10.1109/MSP.2020.2978507.

[40] S. M. Patole, M. Torlak, D. Wang, and M. Ali. “Automotive radars: A review of signal processing techniques”. In: *IEEE Signal Processing Magazine* 34.2 (Mar. 2017), pp. 22–35. ISSN: 1558-0792. DOI: 10.1109/MSP.2016.2628914.

[41] F. Roos, J. Bechter, C. Knill, B. Schweizer, and C. Waldschmidt. “Radar Sensors for Autonomous Driving: Modulation Schemes and Interference Mitigation”. en. In: *IEEE Microwave Magazine* 20.9 (Sept. 2019), pp. 58–72. ISSN: 1527-3342, 1557-9581. DOI: 10.1109/MMM.2019.2922120. URL: https://ieeexplore.ieee.org/document/8792451/ (visited on 05/05/2021).

[42] E. Hossain, D. Niyato, and Z. Han. *Dynamic Spectrum Access and Management in Cognitive Radio Networks*. en. Google-Books-ID: DSuD9_skTcsC. Cambridge University Press, June 2009. ISBN: 978-0-521-89847-8.

[43] S. Haykin. *Cognitive Dynamic Systems: Perception-action Cycle, Radar and Radio*. en. Google-Books-ID: GMDdQEVm74UC. Cambridge University Press, Mar. 2012. ISBN: 978-0-521-11436-3.

[44] C. Aydogdu, M. F. Keskin, N. Garcia, H. Wymeersch, and D. W. Bliss. “RadChat: Spectrum Sharing for Automotive Radar Interference Mitigation”. In: *IEEE Transactions on Intelligent Transportation Systems* (2019), pp. 1–14. ISSN: 1558-0016. DOI: 10.1109/TITS.2019.2959881.

[45] J. Khoury, R. Ramanathan, D. McCloskey, R. Smith, and T. Campbell. “RadarMAC: Mitigating Radar Interference in Self-Driving Cars”. In: *2016 13th Annual IEEE International Conference on Sensing, Communication, and Networking (SECON)*. June 2016, pp. 1–9. DOI: 10.1109/SAHCN.2016.7733011.

[46] F. Uysal. “Phase-Coded FMCW Automotive Radar: System Design and Interference Mitigation”. In: *IEEE Transactions on Vehicular Technology* 69.1 (Jan. 2020), pp. 270–281. ISSN: 1939-9359. DOI: 10.1109/TVT.2019.2953305.

[47] N. Levanon and E. Mozeson. “Multicarrier radar signal - pulse train and CW”. In: *IEEE Transactions on Aerospace and Electronic Systems* 38.2 (Apr. 2002), pp. 707–720. ISSN: 1557-9603. DOI: 10.1109/TAES.2002.1009000.

[48] C. Sturm and W. Wiesbeck. “Waveform Design and Signal Processing Aspects for Fusion of Wireless Communications and Radar Sensing”. In: *Proceedings of the IEEE* 99.7 (July 2011). Number: 7, pp. 1236–1259. ISSN: 1558-2256. DOI: 10.1109/JPROC.2011.2131110.

[49] C. Knill, B. Schweizer, S. Sparrer, F. Roos, R. F. H. Fischer, and C. Waldschmidt. “High Range and Doppler Resolution by Application of Compressed Sensing Using Low Baseband Bandwidth OFDM Radar”. In: *IEEE Transactions on Microwave Theory and Techniques* 66.7 (July 2018), pp. 3535–3546. ISSN: 1557-9670. DOI: 10.1109/TMTT.2018.2830389.

[50] Z. Cheng, Z. He, B. Liao, and M. Fang. “MIMO Radar Waveform Design With PAPR and Similarity Constraints”. In: *IEEE Transactions on Signal Processing* 66.4 (Feb. 2018), pp. 968–981. ISSN: 1941-0476. DOI: 10.1109/TSP.2017.2780052.

[51] M. F. Keskin, H. Wymeersch, and V. Koivunen. “MIMO-OFDM Joint Radar-Communications: Is ICI Friend or Foe?” In: *IEEE Journal of Selected Topics in Signal Processing* 15.6 (Nov. 2021), pp. 1393–1408. ISSN: 1941-0484. DOI: 10.1109/JSTSP.2021.3109431.

[52] C. Knill, F. Embacher, B. Schweizer, S. Stephany, and C. Waldschmidt. “Coded OFDM Waveforms for MIMO Radars”. In: *IEEE Transactions on Vehicular Technology* 70.9 (Sept. 2021), pp. 8769–8780. ISSN: 1939-9359. DOI: 10.1109/TVT.2021.3073268.

[53] M. Bică and V. Koivunen. “Generalized Multicarrier Radar: Models and Performance”. In: *IEEE Transactions on Signal Processing* 64.17 (Sept. 2016), pp. 4389–4402. ISSN: 1941-0476. DOI: 10.1109/TSP.2016.2566610.

[54] M. Bică and V. Koivunen. “Radar Waveform Optimization for Target Parameter Estimation in Cooperative Radar-Communications Systems”. In: *IEEE Transactions on Aerospace and Electronic Systems* 55.5 (Oct. 2019), pp. 2314–2326. ISSN: 2371-9877. DOI: 10.1109/TAES.2018.2884806.

[55] L. Gaudio, M. Kobayashi, G. Caire, and G. Colavolpe. “On the Effectiveness of OTFS for Joint Radar Parameter Estimation and Communication”. In: *IEEE Transactions on Wireless Communications* (2020), pp. 1–1. ISSN: 1558-2248. DOI: 10.1109/TWC.2020.2998583.

[56] M. Skolnik. *Radar Handbook*. Electronic engineering series. McGraw-Hill, 1990. ISBN: 9780070579132. URL: https://books.google.de/books?id=s35UAAAAMAAJ.

[57] M. Richards. *Fundamentals of Radar Signal Processing*. Professional Engineering. Mcgraw-hill, 2005. ISBN: 9780071444743. URL: https://books.google.de/books?id=VOvsJ7G1oDEC.

[58] D. Mateos-Núñez, M. A. González-Huici, R. Simoni, F. B. Khalid, M. Eschbaumer, and A. Roger. “Sparse array design for Automotive MIMO Radar”. In: *2019 16th European Radar Conference (EuRAD)*. Oct. 2019, pp. 249–252.

[59] D. Mateos-Núñez, R. Simoni, M. A. González-Huici, and A. Correas-Serrano. "Design of mutually incoherent arrays for DoA estimation via group-sparse reconstruction". In: *2019 IEEE Radar Conference (RadarConf)*. ISSN: 2375-5318. Apr. 2019, pp. 1–6. DOI: 10.1109/RADAR.2019.8835842.

[60] G. Babur, P. Aubry, and F. L. Chevalier. "Simple transmit diversity technique for phased array radar". en. In: *IET Radar, Sonar & Navigation* 10.6 (July 2016), pp. 1046–1056. ISSN: 1751-8792. DOI: 10.1049/iet-rsn.2015.0311. (Visited on 01/14/2021).

[61] Z. Zhao, M. Schellmann, X. Gong, Q. Wang, R. Böhnke, and Y. Guo. "Pulse shaping design for OFDM systems". In: *EURASIP Journal on Wireless Communications and Networking* 2017 (2017), pp. 1–25.

[62] D. Roque and S. Bidon. "Range migration in symbol-based OFDM radar receivers". In: *2021 IEEE 22nd International Workshop on Signal Processing Advances in Wireless Communications (SPAWC)*. IEEE. 2021, pp. 496–500.

[63] G. Babur, O. A. Krasnov, A. Yarovoy, and P. Aubry. "Nearly Orthogonal Waveforms for MIMO FMCW Radar". In: *IEEE Transactions on Aerospace and Electronic Systems* 49.3 (July 2013), pp. 1426–1437. ISSN: 1557-9603. DOI: 10.1109/TAES.2013.6557996.

[64] H. Bolcskei. "MIMO-OFDM wireless systems: basics, perspectives, and challenges". In: *IEEE Wireless Communications* 13.4 (Aug. 2006), pp. 31–37. ISSN: 1558-0687. DOI: 10.1109/MWC.2006.1678163.

[65] C. Sturm, Y. L. Sit, M. Braun, and T. Zwick. "Spectrally interleaved multi-carrier signals for radar network applications and multi-input multi-output radar". en. In: *IET Radar, Sonar & Navigation* 7.3 (2013), pp. 261–269. ISSN: 1751-8792. DOI: 10.1049/iet-rsn.2012.0040. (Visited on 06/01/2023).

[66] G. D. Surabhi, R. M. Augustine, and A. Chockalingam. *Multiple Access in the Delay-Doppler Domain using OTFS modulation*. arXiv:1902.03415 [cs, math]. Feb. 2019. DOI: 10.48550/arXiv.1902.03415. (Visited on 07/14/2023).

[67] A. De Maio, Y. C. Eldar, and A. M. Haimovich. *Compressed sensing in radar signal processing*. Cambridge University Press, 2019.

[68] A. Correas-Serrano and M. A. Gonzalez-Huici. "Sparse Reconstruction of Chirplets for Automotive FMCW Radar Interference Mitigation". In: *2019 IEEE MTT-S International Conference on Microwaves for Intelligent Mobility (ICMIM)*. Apr. 2019, pp. 1–4. DOI: 10.1109/ICMIM.2019.8726758.

[69] M. F. Keskin, C. Marcus, O. Eriksson, A. Alvarado, J. Widmer, and H. Wymeersch. "Integrated Sensing and Communications with MIMO-OTFS: ISI/ICI Exploitation and Delay-Doppler Multiplexing". In: *IEEE Transactions on Wireless Communications* (2024).

[70] A. Correas-Serrano, N. Petrov, M. Gonzalez-Huici, and A. Yarovoy. "MIMO OTFS with Arbitrary Time-Frequency Allocation for Joint Radar and Communications". In: *IEEE Transactions on Radar Systems* (2023).

[71] S. D. Blunt and E. L. Mokole. “Overview of radar waveform diversity”. In: *IEEE Aerospace and Electronic Systems Magazine* 31.11 (Nov. 2016), pp. 2–42. ISSN: 1557-959X. DOI: 10.1109/MAES.2016.160071.

[72] A. Correas-Serrano, N. Petrov, M. Gonzalez-Huici, and A. Yarovoy. “Comparison of Radar Receivers for OFDM and OTFS waveforms”. In: *2022 19th European Radar Conference (EuRAD)*. Sept. 2022, pp. 1–4. DOI: 10.23919/EuRAD54643.2022.9924824.

[73] M. F. Keskin, H. Wymeersch, and V. Koivunen. “ICI-Aware Parameter Estimation for Mimo-Ofdm Radar via Apes Spatial Filtering”. In: *ICASSP 2021 - 2021 IEEE International Conference on Acoustics, Speech and Signal Processing (ICASSP)*. ISSN: 2379-190X. June 2021, pp. 8248–8252. DOI: 10.1109/ICASSP39728.2021.9414537.

[74] M. Bică and V. Koivunen. “Multicarrier Radar-communications Waveform Design for RF Convergence and Coexistence”. In: *ICASSP 2019 - 2019 IEEE International Conference on Acoustics, Speech and Signal Processing (ICASSP)*. ISSN: 2379-190X. May 2019, pp. 7780–7784. DOI: 10.1109/ICASSP.2019.8683655.

[75] K. M. Braun. “OFDM radar algorithms in mobile communication networks”. PhD thesis. Karlsruhe, Karlsruher Institut für Technologie (KIT), Diss., 2014, 2014.

[76] C. Knill. “Novel MIMO OFDM waveform designs and high-performance signal processing methods for digital radars”. en. Accepted: 2022-04-07T11:39:48Z ISBN: 9781798281574. Dissertation. Universität Ulm, Apr. 2022. DOI: 10.18725/OPARU-42838. URL: https://oparu.uni-ulm.de/xmlui/handle/123456789/42914 (visited on 09/01/2022).

[77] Y. Hong, T. Thaj, and E. Viterbo. *Delay-Doppler Communications: Principles and Applications*. 1st ed. eBook ISBN : 9780323859660. Academic Press, 2022. ISBN: 9780323850285.

[78] M. S. Davis and A. D. Lanterman. “Minimum integrated sidelobe ratio filters for MIMO radar”. In: *IEEE Transactions on Aerospace and Electronic Systems* 51.1 (2015), pp. 405–416.

[79] J. Li and P. Stoica. *MIMO radar signal processing*. John Wiley & Sons, 2008.

[80] L. Gaudio, M. Kobayashi, G. Caire, and G. Colavolpe. “Joint Radar Target Detection and Parameter Estimation with MIMO OTFS”. In: *2020 IEEE Radar Conference (RadarConf20)*. ISSN: 2375-5318. Sept. 2020, pp. 1–6. DOI: 10.1109/RadarConf2043947.2020.9266546.

[81] Y. Ge, Q. Deng, P. Ching, and Z. Ding. “OTFS signaling for uplink NOMA of heterogeneous mobility users”. In: *IEEE Transactions on Communications* 69.5 (2021), pp. 3147–3161.

[82] 3GPP TS 36.101. *‘Evolved Universal Terrestrial Radio Access (E-UTRA); User Equipment (UE) Radio Transmission and Reception.” 3rd Generation Partnership Project; Technical Specification Group Radio Access Network*. https://www.3gpp.org. 2021.

[83] J. H. G. Ender. “On compressive sensing applied to radar”. en. In: *Signal Processing*. Special Section on Statistical Signal & Array Processing 90.5 (May 2010), pp. 1402–1414. ISSN: 0165-1684. DOI: 10.1016/j.sigpro.2009.11.009. (Visited on 04/06/2022).

[84] J. Wang, S. Kwon, and B. Shim. “Generalized Orthogonal Matching Pursuit”. In: *IEEE Transactions on Signal Processing* 60.12 (Dec. 2012), pp. 6202–6216. ISSN: 1941-0476. DOI: 10.1109/TSP.2012.2218810.

[85] A. Correas-Serrano and M. A. González-Huici. “Experimental Evaluation of Compressive Sensing for DoA Estimation in Automotive Radar”. In: *2018 19th International Radar Symposium (IRS)*. ISSN: 2155-5753. June 2018, pp. 1–10. DOI: 10.23919/IRS.2018.8448197.

[86] A. Correas-Serrano, M. Gonzalez-Huici, R. Simoni, T. Bredderman, E. Warsitz, T. Müller, and O. Kirsch. “Performance Analysis and Design of a Distributed Radar Network for Automotive Application”. In: *2022 23rd International Radar Symposium (IRS)*. ISSN: 2155-5753. Sept. 2022, pp. 30–35. DOI: 10.23919/IRS54158.2022.9904987.

[87] S. Tiwari, S. S. Das, and V. Rangamgari. “Low complexity LMMSE Receiver for OTFS”. In: *IEEE Communications Letters* 23.12 (Dec. 2019), pp. 2205–2209. ISSN: 1558-2558. DOI: 10.1109/LCOMM.2019.2945564.

[88] Y. Hong, T. Thaj, and E. Viterbo. *Delay-Doppler Communications: Principles and Applications*. Elsevier, 2022.

[89] R. Hadani and A. Monk. “OTFS: A New Generation of Modulation Addressing the Challenges of 5G”. In: *arXiv:1802.02623 [cs, math]* (Feb. 2018). (Visited on 05/20/2020).

[90] M.-E. Chatzitheodoridi, A. Taylor, and O. Rabaste. “A Mismatched Filter for Integrated Sidelobe Level Minimization over a Continuous Doppler Shift Interval”. In: *2020 IEEE Radar Conference (RadarConf20)*. 2020 IEEE Radar Conference (RadarConf20). Florence, Italy: IEEE, Sept. 2020. DOI: 10.1109/RadarConf2043947.2020.9266564. URL: https://hal.archives-ouvertes.fr/hal-03104178 (visited on 03/22/2022).

[91] O. A. Krasnov, G. P. Babur, Z. Wang, L. P. Ligthart, and F. v. d. Zwan. “Basics and first experiments demonstrating isolation improvements in the agile polarimetric FM-CW radar – PARSAX”. en. In: *International Journal of Microwave and Wireless Technologies* 2.3-4 (Aug. 2010), pp. 419–428. ISSN: 1759-0795, 1759-0787. DOI: 10.1017/S1759078710000371. (Visited on 07/14/2023).

[92] Y. Ge, Q. Deng, P. Ching, and Z. Ding. “Receiver design for OTFS with a fractionally spaced sampling approach”. In: *IEEE Transactions on Wireless Communications* 20.7 (2021), pp. 4072–4086.

[93] J. Lunden, V. Koivunen, and H. V. Poor. “Spectrum Exploration and Exploitation for Cognitive Radio: Recent Advances”. In: *IEEE Signal Processing Magazine* 32.3 (May 2015), pp. 123–140. ISSN: 1558-0792. DOI: 10.1109/MSP.2014.2338894.

[94] A. Correas-Serrano, N. Petrov, M. Gonzalez-Huici, and A. Yarovoy. “Optimized Time-Frequency Allocation in MIMO NU-OTFS Radar for Enhanced Performance Under Spectral Constraints”. In: *2024 IEEE Radar Conference (RadarConf24)*. IEEE. 2024, pp. 1–6.

[95] Y. C. Eldar, P. Kuppinger, and H. Bolcskei. “Block-Sparse Signals: Uncertainty Relations and Efficient Recovery”. In: *IEEE Transactions on Signal Processing* 58.6 (June 2010), pp. 3042–3054. ISSN: 1941-0476. DOI: 10.1109/TSP.2010.2044837.

[96] D. Bertsimas and J. Tsitsiklis. “Simulated annealing”. In: *Statistical science* 8.1 (1993), pp. 10–15.

[97] A. Correas-Serrano, N. Petrov, M. Gonzalez-Huici, and A. Yarovoy. “Experimental Validation of NU-OTFS MIMO Radar through Polarimetric Measurements”. In: *2024 21st European Radar Conference (EuRAD)*. 2024, pp. 1–4.

[98] A. Correas-Serrano, N. Petrov, M. Gonzalez-Huici, and A. Yarovoy. “Constant Modulus OTFS Based on Zak Transform of Complementary Sequences for Joint Radar and Communications”. In: *IEEE Transactions on Radar Systems* (2025). submitted for publication.

[99] S. K. Dehkordi, L. Gaudio, M. Kobayashi, G. Caire, and G. Colavolpe. “Beam-space MIMO radar for joint communication and sensing with OTFS modulation”. In: *IEEE Transactions on Wireless Communications* 22.10 (2023), pp. 6737–6749.

[100] D. Guel and J. Palicot. “Analysis and comparison of clipping techniques for OFDM Peak-to-Average Power Ratio reduction”. In: *2009 16th International Conference on Digital Signal Processing*. ISSN: 2165-3577. July 2009, pp. 1–6. DOI: 10.1109/ICDSP.2009.5201128.

[101] S. Chang, E. J. Powers, and J. Chung. “A compensation scheme for nonlinear distortion in OFDM systems”. In: *Globecom’00-IEEE. Global Telecommunications Conference. Conference Record (Cat. No. 00CH37137)*. Vol. 2. IEEE. 2000, pp. 736–740.

[102] B. D. Carlton and J. G. Metcalf. “Orthogonal frequency peak-to-average power ratio reduction via the error reduction algorithm”. In: *2022 IEEE radar conference (RadarConf22)*. IEEE. 2022, pp. 1–6.

[103] P. Varshney, P. Babu, and P. Stoica. “Low-PAPR OFDM waveform design for radar and communication systems”. In: *IEEE Transactions on Radar Systems* 1 (2023), pp. 69–74.

[104] S. P. Lavery and T. Ratnarajah. “Remote Sensing with Constant-Modulus OFDM Signals from Complementary Sequences”. In: *2024 IEEE Radar Conference (RadarConf24)*. IEEE. 2024, pp. 1–6.

[105] K. Willstatter and M. D. Zoltowski. “Complementary sequence encoding for 1D and 2D constant-modulus OFDM transmission at millimeter wave frequencies”. In: *ICASSP 2019-2019 IEEE International Conference on Acoustics, Speech and Signal Processing (ICASSP)*. IEEE. 2019, pp. 4804–4808.

[106] M. C. Jeruchim, P. Balaban, and K. S. Shanmugan. *Simulation of communication systems: modeling, methodology and techniques*. Springer Science & Business Media, 2006.

[107] E. Costa, M. Midrio, and S. Pupolin. "Impact of amplifier nonlinearities on OFDM transmission system performance". In: *IEEE Communications Letters* 3.2 (1999), pp. 37–39.

[108] H. Ochiai. "Performance analysis of peak power and band-limited OFDM system with linear scaling". In: *IEEE Transactions on Wireless Communications* 2.5 (2003), pp. 1055–1065.

[109] K. Willstatter. "Constant-Modulus OFDM Transmission Using Complementary Sequences". PhD thesis. Purdue University, 2022.

[110] Z. Cui, P. Zhang, and S. Pollin. "6G wireless communications in 7-24 GHz band: Opportunities, techniques, and challenges". In: *arXiv preprint arXiv:2310.06425* (2023).

ACKNOWLEDGEMENTS

Completing this dissertation is the hardest and longest challenge I have faced in my professional and academic life. I expected it to be demanding, but the COVID-19 pandemic added difficulties no one could have predicted. This thesis would not exist without the support of many people. I am deeply grateful to my supervisory team at TU Delft: my promotor, Prof. Olexander Yaroviy, for his consistency and for keeping me grounded. My daily supervisor, Dr. Nikita Petrov, for all his help and especially for his patience and availability when receiving last-minute drafts to review right before submission. I would also like to thank my supervisor during these years at the Fraunhofer FHR, Dr. María Gonzalez-Huici. Since before I even started my Ph.D. journey, she has always supported me by facilitating the required mental space and time to do this research.

I would also like to thank my colleagues in Fraunhofer FHR: Christian (x2), Renato, Avinash, and so many others. Special thanks to David for the time you took over the years to patiently explain concepts that back then were alien to me, but now seem like common sense. I am also very grateful for my long-distance colleagues in the MS3 group at TU Delft. Although I did not have a lot of contact with you on a daily basis, you always made me feel like a part of the team when we met at conferences. And of course, I am incredibly grateful to Fred; without being able to perform experiments remotely thanks to you, there would be no thesis to speak of.

Thanks to all my friends, who have supported and endured me these years. Years in which I have occasionally disappeared for months while writing a paper, or have been insufferably pessimistic due to some (un)expected setback in my research. Thank you, Javi, Ismael, and Julio, for making me feel like I never left Spain when we have a chance to hang out. Thanks to Carlos for always being there as the friendliest face. Thanks to the Riopar August crew for being such an awesome crowd; spending time with you is always a healing experience. Also, thanks to all my friends and important people that I have met in Bonn over the years: Alessandra, Katigo, Torben, Ruth, Joe, Jacob, Huda, Lennard, Candela, and so many others. You have made and keep making my time in Bonn so great.

Last, but definitely not least, thanks to my family. Gracias, papá y mamá, por apoyarme en todo lo que me propongo. Gracias a mi hermano Diego por ser el mejor compañero de juegos y un gran ejemplo a seguir, y gracias a Helena por inyectar tanta vida y energía en mi existencia, y acompañarme en los últimos años de mi doctorado. Os quiero a todos.

About the Author

Aitor Correas-Serrano was born in Tarragona, Spain, in 1993. He completed his B.Sc. and M.Sc. in telecommunications engineering at the Technical University of Cartagena in 2015 and 2017, respectively. During his master's program, he worked as a research engineer at the Fraunhofer Institute for high-frequency physics and radar (FHR) in Wachtberg, Germany, where he completed his master's thesis on Compressed Sensing methods applied to automotive radar. Since then, he has continued his work on MIMO waveforms, interference cancellation, and Compressed Sensing at the Fraunhofer FHR. In 2020, he became an external Ph.D. student in the Microwave Sensing, Signals and Systems group at TU Delft, focusing on waveform design and adaptive strategies for multifunctional radar and communication systems. As of January 2025, Aitor is leading the Sensor Data Intelligence group at Fraunhofer FHR. In his career, he has been nominated in three conferences for Best Paper Award, having won none of the prizes.

LIST OF PUBLICATIONS

Journal Publications

J1 **A. Correas-Serrano**, N. Petrov, M. Gonzalez-Huici and A. Yarovoy, "MIMO OTFS With Arbitrary Time-Frequency Allocation for Joint Radar and Communications" in IEEE Transactions on Radar Systems, vol. 1, pp. 707-718, 2023.

J2 **A. Correas-Serrano**, N. Petrov, M. Gonzalez-Huici and A. Yarovoy, "Emerging Trends in Radar: OTFS-based Radar for Integrated Sensing and Communications Systems," in IEEE Aerospace and Electronic Systems Magazine.

J3 **A. Correas-Serrano**, N. Petrov, M. Gonzalez-Huici and A. Yarovoy, "Constant Modulus OTFS Based on Zak Transform of Complementary Sequences for Joint Radar and Communications" in IEEE Transactions on Radar Systems, *submitted*.

Conference Publications

C1 **A. Correas-Serrano** et al., "Performance Analysis and Design of a Distributed Radar Network for Automotive Application," 2022 23rd International Radar Symposium (IRS), Gdansk, Poland, 2022, pp. 30-35.

C2 **A. Correas-Serrano**, N. Petrov, M. Gonzalez-Huici and A. Yarovoy, "Comparison of Radar Receivers for OFDM and OTFS waveforms," 2022 19th European Radar Conference (EuRAD), Milan, Italy, 2022, pp. 1-4

C3 **A. Correas-Serrano**, N. Petrov, M. Gonzalez-Huici and A. Yarovoy, "CDMA and Non-Uniform Multiplexing: A Study of Dynamic Range in MIMO Radar Waveforms," ICMIM 2024; 7th IEEE MTT Conference, Boppard, 2024, pp. 53-56.

C4 **A. Correas-Serrano**, N. Petrov, M. Gonzalez-Huici and A. Yarovoy, "Optimized Time-Frequency Allocation in MIMO NU-OTFS Radar for Enhanced Performance Under Spectral Constraints," 2024 IEEE Radar Conference (RadarConf24), Denver, CO, USA, 2024, pp. 1-6

C5 Ramesh, Avinash Nittur, **Aitor Correas-Serrano**, and María González-Huici. "SCaRL-A Synthetic Multi-Modal Dataset for Autonomous Driving." ICMIM 2024; 7th IEEE MTT Conference, Boppard, 2024, pp. 53-56.

C6 **A. Correas-Serrano**, N. Petrov, M. Gonzalez-Huici and A. Yarovoy, "Experimental Validation of NU-OTFS MIMO Radar through Polarimetric Measurements," 2024 21st European Radar Conference (EuRAD), Paris, France, 2024, pp. 63-66.

C7 C. Kurtscheid, **A. Correas-Serrano** and M. Gonzalez-Huici, "Iterative Adaptive Thresholding for 2D Estimation in Sparse Radar Arrays: Performance Analysis and Experimental Validation", 2025 22nd European Radar Conference (EuRAD), Utrecht, Netherlands, 2025.

Pre-thesis Conference Publications

C1 **A. Correas-Serrano** and M. A. González-Huici, "Experimental Evaluation of Compressive Sensing for DoA Estimation in Automotive Radar," 2018 19th International Radar Symposium (IRS), Bonn, Germany, 2018, pp. 1-10.

C2 **A. Correas-Serrano** and M. A. Gonzalez-Huici, "Sparse Reconstruction of Chirplets for Automotive FMCW Radar Interference Mitigation," 2019 IEEE MTT-S International Conference on Microwaves for Intelligent Mobility (ICMIM), Detroit, MI, USA, 2019, pp. 1-4.

C3 D. Mateos-Núñez, R. Simoni, M. A. González-Huici and **A. Correas-Serrano**, "Design of mutually incoherent arrays for DoA estimation via group-sparse reconstruction," 2019 IEEE Radar Conference (RadarConf), Boston, MA, USA, 2019, pp. 1-6.

Pre-thesis Patents

P1 M. A. Gonzalez-Huici, David Mateos-Nunez, R. Simoni, C. Greiff, and **A. Correas-Serrano** (2018) "Method for detection and height and azimuth estimation of objects in a scene by radar processing using sparse reconstruction with coherent and incoherent arrays" (EP3588128B1)

P2 M. A. Gonzalez-Huici, David Mateos-Nunez, R. Simoni, and **A. Correas-Serrano** (2019) "Verfahren zur synthese von antennenanordnungslayouts oder zur auswahl der wellenform in einem satz von zueinander inkohärenten aperturen für radar- und hochfrequenzanwendungen " (EP3690483B1)